



TECHNISCHE  
UNIVERSITÄT  
MÜNCHEN



WALTHER-MEISSNER-  
INSTITUT FÜR TIEF-  
TEMPERATURFORSCHUNG



BAYERISCHE  
AKADEMIE DER  
WISSENSCHAFTEN

# Displacement of Squeezed Propagating Microwave States

Master's Thesis  
Stefan Pogorzalek

Supervisor: Prof. Dr. Rudolf Gross  
Munich, October 2015

Fakultät für Physik  
TECHNISCHE UNIVERSITÄT MÜNCHEN



# Contents

<b>1</b>	<b>Introduction</b>	<b>1</b>
<b>2</b>	<b>Theory</b>	<b>5</b>
2.1	Propagating quantum microwaves . . . . .	5
2.1.1	Representation of quantum microwaves . . . . .	5
2.1.2	Gaussian quantum microwave states . . . . .	8
2.1.3	Dual-path state reconstruction method . . . . .	14
2.2	The Josephson Parametric Amplifier . . . . .	17
2.2.1	Josephson junctions . . . . .	17
2.2.2	Dc-SQUID . . . . .	19
2.2.3	Coplanar waveguide resonator . . . . .	22
2.2.4	Coplanar waveguide resonator grounded by a dc-SQUID . . . . .	24
2.2.5	Parametric amplification and generation of squeezed light . . . . .	26
2.2.6	Flux-driven JPA . . . . .	27
<b>3</b>	<b>Experimental techniques</b>	<b>31</b>
3.1	Cryogenic setup . . . . .	31
3.1.1	Cryostat . . . . .	31
3.1.2	Sample preparation . . . . .	34
3.1.3	Sample stage . . . . .	36
3.1.4	Input and output lines . . . . .	37
3.2	IQ Cross-correlation detector . . . . .	38
3.2.1	Room temperature dual-path receiver . . . . .	38
3.2.2	Data acquisition and processing with Acqiris card . . . . .	41
3.2.3	Calibration . . . . .	43
<b>4</b>	<b>JPA characterization</b>	<b>47</b>
4.1	Flux dependence . . . . .	47
4.1.1	Quality factors . . . . .	50
4.1.2	Simulation of the dc-SQUID potential . . . . .	53
4.1.3	Comparison with experimental data . . . . .	57
4.1.4	Comparison to literature . . . . .	60
4.2	Non-degenerate operation mode . . . . .	61

---

4.2.1	Non-degenerate signal gain . . . . .	61
4.2.2	Noise properties . . . . .	62
<b>5</b>	<b>Displacement of squeezed microwave states</b>	<b>65</b>
5.1	Squeezed vacuum states . . . . .	65
5.2	Squeezing versus signal gain . . . . .	67
5.2.1	Experimental results . . . . .	67
5.2.2	Models describing the squeezing level . . . . .	70
5.3	Displacement of quantum states . . . . .	76
5.4	Squeezing versus displacement . . . . .	79
5.4.1	Experimental results . . . . .	79
5.4.2	Effect of phase fluctuations and the PNCF . . . . .	82
<b>6</b>	<b>Conclusions and outlook</b>	<b>87</b>
<b>A</b>	<b>Simulation of dc-SQUID potential</b>	<b>89</b>
<b>B</b>	<b>Cumulants and Gaussianity</b>	<b>91</b>
<b>C</b>	<b>Negativity</b>	<b>93</b>
	<b>Bibliography</b>	<b>95</b>
	<b>Acknowledgments</b>	<b>100</b>

# List of Figures

2.1	Thermal states . . . . .	9
2.2	Coherent state . . . . .	11
2.3	Squeezed vacuum state . . . . .	12
2.4	Squeezed coherent states . . . . .	14
2.5	Dual-path principle . . . . .	15
2.6	Josephson junction and dc-SQUID . . . . .	18
2.7	Microwave resonator models . . . . .	24
2.8	Parametric amplification scheme . . . . .	27
2.9	JPA working principle . . . . .	28
3.1	Photograph of the $^3\text{He}/^4\text{He}$ -dilution refrigerator . . . . .	32
3.2	Schematic of cryogenic setup . . . . .	33
3.3	Optical micrograph of a JPA sample chip . . . . .	34
3.4	Photograph of JPA sample box and aluminum shield . . . . .	35
3.5	Photograph of sample rod . . . . .	36
3.6	Schematic of dual-path receiver . . . . .	39
3.7	Photograph of peltier cooled RT-amplifiers . . . . .	40
3.8	Photograph of Dual-path receiver . . . . .	41
3.9	Sketch of Acqiris card based data acquisition and processing . . . . .	42
3.10	Unbalanced histogram of the total counts for each ADC bin for both channels . . . . .	44
3.11	Time trace for a strong coherent signal . . . . .	44
3.12	Quadrature moments as a function of attenuator temperature . . . . .	46
4.1	Flux dependence measurement setup . . . . .	48
4.2	Flux dependence of JPA Q600 without a pump tone . . . . .	48
4.3	Flux dependence of JPA Q200 without a pump tone . . . . .	49
4.4	Flux dependence of JPA Q200new without a pump tone . . . . .	49
4.5	Fitted reflection magnitude and phase according to input-output formalism of JPA Q600 . . . . .	50
4.6	Fitted reflection magnitude and phase according to input-output formalism of JPA Q200 . . . . .	51
4.7	Fitted reflection magnitude and phase according to input-output formalism of JPA Q200new . . . . .	52

4.8	Dc-SQUID potential for different external flux values $\varphi_{\text{ext}}$ . . . . .	54
4.9	Dc-SQUID potential for different transport currents $j$ . . . . .	56
4.10	Fitted flux dependence of JPA Q600 . . . . .	58
4.11	Fitted flux dependence of JPA Q200 and JPA Q200new . . . . .	59
4.12	Total critical current of a dc-SQUID vs. external flux for different screening parameters . . . . .	61
4.13	Spectrum of non-degenerate signal gain for different pump powers for JPA Q200new . . . . .	62
4.14	Noise power as a function of the attenuator temperature for JPA Q200 . . . . .	63
5.1	Squeezed vacuum state . . . . .	66
5.2	Wigner functions of squeezed vacuum states for different pump powers . . . . .	68
5.3	Squeezing level as a function of the signal gain at 5.594 GHz . . . . .	69
5.4	Squeezing level as a function of the signal gain at 5.51 GHz . . . . .	70
5.5	Squeeze factor extracted under the assumption of thermal squeezed vacuum states . . . . .	71
5.6	Sketch of sidebands . . . . .	72
5.7	Fitted squeezing level as a function of the signal gain at 5.594 GHz . . . . .	74
5.8	Fitted squeezing level as a function of the signal gain at 5.51 GHz . . . . .	74
5.9	Displaced squeezed vacuum state for different displacement angles . . . . .	77
5.10	Simulation of displaced squeezed vacuum state for different displacement angles . . . . .	78
5.11	Displacement photons as a function of displacement power . . . . .	80
5.12	Squeezing level as a function of displacement . . . . .	81
5.13	Negativity kernel as a function of displacement . . . . .	82
5.14	Simulation of phase fluctuations and misestimated PNCF for coherent states . . . . .	83
5.15	Simulation of phase fluctuations on displaced squeezed states . . . . .	86
A.1	Sketch for simulation of dc-SQUID potential and determination of normalized critical current $j_c(\varphi_{\text{ext}})$ . . . . .	89

# List of Tables

3.1	Fitted PNCFs and number of noise photons of the two detection chains .	46
4.1	Fitting results of flux dependence of the resonant frequency for the measured samples . . . . .	59
5.1	Fitting results of the squeezing level with red sideband contribution . . .	75
5.2	Squeezing levels in dB for simulated displaced vacuum states . . . . .	85



# Chapter 1

## Introduction

Since the rise of quantum theory in the early 20th century, substantial discoveries in the field have been made and various quantum phenomena have been experimentally studied and theoretically described. In the last two decades, significant effort has been invested in the question, whether these quantum phenomena can help to surpass the performance of classical information processing and communication. With that, the field of quantum information science was born. Several protocols exist in this field, in which the superposition of quantum states and entanglement between spatially separated systems is of central importance. For example, in quantum computing one replaces the classical bits with so called quantum bits, or qubits, which can be realized by quantum two-level-systems. A qubit can be in any superposition of two eigenstates and thus, in contrast to classical bits, a continuum of states is available. For certain types of problems, quantum computers are expected to provide a significant speed-up compared to classical computers [1, 2].

Furthermore, quantum key distribution [3, 4], quantum teleportation [5–7], heralded entanglement between distant atoms [8, 9] and a future quantum network [10] are topics of high interest. Here, the exchange of quantum information between multiple parties is required and the question of how to achieve this exchange arises. Apart from directly transporting the entity, in which a quantum state is encoded, one can use a 'carrier', which interacts with the quantum state and travels to the desired location to retrieve the information there. In quantum electrodynamics (QED) one studies the interaction between light and matter. The photons can then take the role of the 'carrier' which carries information about the quantum state of the object.

In a basic quantum optics experiment one uses optical photons in a cavity and single atoms, acting as natural two-level-systems, to study the quantum phenomena resulting from the interaction between the photons and the qubit. From that the field of cavity QED [11] was created and substantial progress has been made over the last years [12]. However, the interaction strength between atoms and the light field in an optical cavity is limited by the small dipole moments of the atoms and low field strengths due to the large mode volume of a cavity.

Replacing the atom by a superconducting circuit acting as an effective two level system and the cavity by an on-chip superconducting microwave resonator opens up the new field of circuit QED. Due to the large dipole moments of the superconducting qubits [13] and the small mode volumes inside a quasi one-dimensional coplanar waveguide resonator, large interaction strengths between qubit and resonator are easily achievable [14]. It is even possible to surpass the coupling strengths of cavity QED and explore new physics in the ultra-strong coupling regime [15].

In contrast to optical cavity QED, where optical photons with frequencies of several hundred THz are used, typical frequencies for circuit QED experiments with superconducting circuits are in the microwave regime around several GHz, leading to two severe experimental drawbacks. First, the superconducting circuits need to be cooled below their transition temperature to become superconducting, in order to be used as an effective two-level system with low loss, forming a qubit. Second, a microwave photon frequency of several GHz corresponds to a temperature of around several 100 mK. Therefore, in an experiment at room temperature the tiny microwave quantum signal would always be obscured by a comparatively huge thermal noise contribution. That is also the reason why there are no efficient single photon detectors for microwave photons at room temperature.

To analyze quantum microwave signals despite the lack of single photon detectors, one needs to amplify the signal, which is inevitably associated with adding noise to the signal [16]. Commercial cryogenic high-electron-mobility transistors (HEMTs) are commonly used at low temperatures as phase-insensitive amplifiers, adding only a few tens of noise photons to a signal during amplification. With a recently developed signal recovery technique, the dual-path state reconstruction scheme [17, 18], we are able to analyze quantum states in the presence of a considerable amount of noise. Furthermore, due to the use of a beam splitter, this technique enables one to characterize the entanglement of quantum microwave signals propagating along two spatially separated paths [19].

Another approach is to use phase-sensitive amplifiers to detect quantum signals. For that purpose Josephson Parametric Amplifiers (JPAs)[20–23] are an essential resource. If operated in the phase-sensitive mode, JPAs exhibit noise performances far below the standard quantum limit [23–25] and can be used as low noise pre-amplifiers followed by standard phase-insensitive amplifiers. At the same time, JPAs are also used to create non-classical microwave states. Due to parametric effects, squeezed states can be generated in a JPA. In a squeezed state the symmetric uncertainties of the two quadratures of a signal are deformed in a way, so that the noise of one quadrature is reduced below the vacuum level. Single-mode squeezed states [19, 23, 24] or two-mode squeezed states [26], depending on the operation mode, have been observed. Since squeezed states are non-classical, they are an important resource in quantum information science protocols for e.g. creating path entanglement [19] or the generation of EPR-pairs for quantum teleportation in the microwave regime [27].

---

In this work we use a flux-driven JPA [20], consisting of a coplanar waveguide resonator, where the inner conductor is grounded on one side by a direct-current superconducting quantum interference device (dc-SQUID). The flux dependent non-linear inductance of the dc-SQUID is utilized to tune the resonant frequency of the resonator. By applying a fast varying flux, the resonant frequency is periodically modulated, giving rise to parametric effects and leading to the generation of squeezed propagating microwave states, which leak out of the JPA through a coupling capacitance. Similarly, two-mode squeezed states can be generated by the dynamical Casimir effect, where quantum fluctuations of a resonator field are converted to a measurable signal by rapidly changing the boundary conditions of the resonator, which has been observed with a similar superconducting circuit [28].

Furthermore, not only squeezed vacuum states, which are located at the origin of the phase-space, but also displaced squeezed states are of interest. On one hand, a squeezed coherent state is generated by sending a coherent signal to a JPA. The center of the resulting squeezed state is no longer located at the origin of the phase space anymore, but is shifted along a certain direction. On the other hand, if one first squeezes the vacuum with a JPA and then feeds the squeezed state into a highly asymmetric directional coupler, which is biased by a strong coherent signal, one obtains a displacement operation on the input state [29] and, thus, a displaced squeezed state is generated. Such a displacement operation is the equivalent to a linear transformation in quantum information protocols when working with continuous variables [27]. Also, a displaced squeezed state is a mixture of a classical signal, the coherent signal, and a non-classical state, the squeezed state, making it an interesting object to study.

This thesis is structured in the following way. First, in chapter 2, we lay a theoretical background for the understanding of propagating quantum microwave signals, including the description of microwave states and the fundamentals of the dual-path reconstruction method. Also, we introduce the constituents of a Josephson Parametric Amplifier and present the working principle of the latter. Furthermore, parametric amplification and the generation of squeezed light are discussed in context of the flux-driven JPA. Next, the experimental techniques with the cryogenic setup and the IQ-cross correlation detector are presented in chapter 3. In chapter 4, the dependence of the resonant frequency of the JPAs on an external flux is studied and simulations, describing the experiments, are presented. Furthermore, non-degenerate gain measurements and the noise properties of a JPA are discussed. Subsequently, we use the JPA in the phase sensitive mode and squeeze vacuum states in chapter 5. We study squeezed vacuum states for different non-degenerate signal gains of the JPA as well as for different displacements in phase space. We present simulations, helping to understand the measured states. Finally, we conclude with a summary and give a short outlook in chapter 6.



# Chapter 2

## Theory

This chapter provides theoretical background of our work. We start by introducing propagating quantum microwave signals and their representation by quasi-probability distributions, in particular by a Wigner function. Next, important microwave states, including coherent and squeezed states, are discussed. Detection of propagating quantum microwave signals is realized with a dual-path state reconstruction method.

Furthermore, we address the fundamental building blocks of a Josephson Parametric Amplifier (JPA), including Josephson junctions and dc-SQUIDs. Finally, we discuss the physics of a flux-driven JPA and its application for the generation of squeezed microwave light.

### 2.1 Propagating quantum microwaves

#### 2.1.1 Representation of quantum microwaves

A single-mode classical microwave signal  $A(t)$  with frequency  $f = \omega/(2\pi)$  can be expressed as

$$A(t) = I(t) \cos(\omega t) + Q(t) \sin(\omega t), \quad (2.1)$$

where  $I(t)$  is an in-phase and  $Q(t)$  is an out-of-phase quadrature component.

For the quantum description of a corresponding photonic field, one has to take into account additional properties imposed by quantum mechanics. One of them is the Heisenberg uncertainty relation between two complementary variables such as quadrature components  $\hat{q}$  and  $\hat{p}$ , which are the quantum mechanical analogies to the classical in-phase and out-of-phase components  $I$  and  $Q$ , respectively. Classically it is possible to measure both complementary variables with infinite accuracy at the same time, whereas in quantum mechanics the knowledge of both variables is limited by the Heisenberg relation

$$\Delta q \Delta p \geq \frac{1}{4}, \quad (2.2)$$

where the standard deviation  $\Delta A$  of an observable  $A$  is given by

$$(\Delta A)^2 = \langle (\Delta \hat{A})^2 \rangle \equiv \langle \hat{A}^2 \rangle - \langle \hat{A} \rangle^2. \quad (2.3)$$

The operator for an one-dimensional, single-mode electrical field is given by [30]

$$\hat{A}(r,t) = C \left[ \hat{a}^\dagger e^{i(\omega t - kr)} + \hat{a} e^{-i(\omega t - kr)} \right], \quad (2.4)$$

where  $C$  is a normalization constant,  $\omega = 2\pi f$  the angular frequency of the light mode and  $k$  the wave vector. We also introduced the creation and annihilation operators  $\hat{a}^\dagger$  and  $\hat{a}$ , respectively, with the usual commutator  $[\hat{a}, \hat{a}^\dagger] = 1$ .

By comparing to a reference plane oscillating as  $\cos(\omega t - kr)$ , one can introduce relations between the field quadratures and the respective field operators [31]

$$\hat{q} = \frac{\hat{a} + \hat{a}^\dagger}{2} \quad \text{and} \quad \hat{p} = \frac{\hat{a} - \hat{a}^\dagger}{2i}, \quad (2.5)$$

obeying the commutation relation  $[\hat{q}, \hat{p}] = \frac{i}{2}$ . If the reference plane has an arbitrary phase-shift  $\theta$ , that means an oscillation like  $\cos(\omega t - kr - \theta)$ , the generalized quadrature operators read

$$\hat{q}_\theta = \frac{(\hat{a}e^{-i\theta} + \hat{a}^\dagger e^{i\theta})}{2} \quad \text{and} \quad \hat{p}_\theta = \frac{(\hat{a}e^{-i\theta} - \hat{a}^\dagger e^{i\theta})}{2i}, \quad (2.6)$$

or utilizing Eq. (2.5)

$$\hat{q}_\theta = \hat{q} \cos(\theta) + \hat{p} \sin(\theta) \quad \text{and} \quad \hat{p}_\theta = -\hat{q} \sin(\theta) + \hat{p} \cos(\theta). \quad (2.7)$$

Therefore, a phase shift  $\theta$  corresponds to a rotation of the axis spanned by  $q$  and  $p$  in a phase space representation.

There exist several ways to describe a quantum state, one being via quasi-probability distributions. Such distributions can not be regarded as a full analogy to a classical probability distribution, since the Heisenberg uncertainty relation prohibits the knowledge of both quadratures at the same time. So the classical approach of defining a probability to find a system in a state with well defined  $q$  and  $p$  is not possible. Nevertheless, the extension to quantum mechanics to so-called quasi-probability distributions proved to be useful in describing quantum states, where the first one was introduced by Wigner [32, 33]

$$W(q,p) = \frac{1}{\pi\hbar} \int \langle q - y | \hat{\rho} | q + y \rangle e^{2ipy/\hbar} dy, \quad (2.8)$$

where  $q$  and  $p$  are the dimensionless amplitudes of the quadratures and  $\hat{\rho}$  is the density matrix of the quantum state. It can be understood as a mapping between phase-space and an operator representation of a quantum state and is called the Weyl-Wigner transform [34].

There also exist other formulations of the Wigner function. One can define the Wigner function as the Fourier transform of a symmetrically ordered characteristic function [30]

$$\xi(\eta) = \text{Tr}\{\hat{\rho}\hat{D}(\eta)\} = \text{Tr}\{\hat{\rho}e^{\eta\hat{a}^\dagger - \eta^*\hat{a}}\}, \quad (2.9)$$

where we also introduced a displacement operator  $\hat{D}(\alpha) = \exp(\alpha\hat{a}^\dagger - \alpha^*\hat{a})$ . Therefore, The characteristic function gives an expectation value of the displacement operator. The Wigner function can then be written as

$$W(\alpha) = \frac{1}{\pi^2} \int \exp(\eta^*\alpha - \eta\alpha^*)\xi(\eta) d^2\eta. \quad (2.10)$$

By defining the complex amplitude  $\alpha = q + ip$ , Eq. (2.10) also maps a quantum state to a phase space. The marginal distributions for  $q$  and  $p$ , giving the probabilities to find the state with a certain  $q$  or  $p$ , are  $w(q) = \int_{-\infty}^{\infty} W(q,p)dp$  and  $w(p) = \int_{-\infty}^{\infty} W(q,p)dq$ , respectively. They can be understood as projections of the Wigner function onto the respective axis.

Based on a different approach, the characteristic function  $\xi(\eta)$  and, thus, the Wigner function, can also be expressed in terms of the normally ordered moments of the creation and annihilation operators  $\langle(\hat{a}^\dagger)^m\hat{a}^n\rangle$  [35, 36]

$$\xi(\eta) = e^{-|\eta|^2/2} \sum_{m,n} \frac{\langle(\hat{a}^\dagger)^m\hat{a}^n\rangle}{m!n!} \eta^m (-\eta^*)^n. \quad (2.11)$$

By inserting the last expression for  $\xi(\eta)$  in Eq. (2.10), the Wigner function is expressed by the moments

$$W(\alpha) = \sum_{m,n} \frac{\langle(\hat{a}^\dagger)^m\hat{a}^n\rangle}{\pi^2 m! n!} \int \eta^m (-\eta^*)^n \exp\left(-\frac{|\eta|^2}{2} + \eta^*\alpha - \eta\alpha^*\right) d^2\eta. \quad (2.12)$$

Consequently, the knowledge of all moments  $\langle(\hat{a}^\dagger)^m\hat{a}^n\rangle$  allows the calculation of the Wigner function. In fact, the description of a quantum state by means of all moments is equal to the description by the Wigner function, or by the density operator [37–40]. It should be noted that for an arbitrary quantum state the knowledge of all moments is needed to fully describe the state. From an experimental point of view the measurement of an infinite amount of moments is not feasible due to a finite measurement time for each moment. In Ref. [36], starting from the Schrödinger-Robertson inequality [41] an uncertainty relation in terms of moments  $\langle(\hat{a}^\dagger)^m\hat{a}^n\rangle$  with  $m + n \leq 2$  as well as inequalities up to fourth order are derived. Such conditions can be used to discard unphysical sets of reconstructed moments.

Based on the principle of maximum entropy first introduced by Jaynes [42], Buzek *et al.* [40, 43] investigated the reconstruction of the Wigner function with a finite number of moments. On the observation level  $\mathcal{O}_2 = \{\hat{a}^\dagger\hat{a}, (\hat{a}^\dagger)^2, \hat{a}^2, \hat{a}^\dagger, \hat{a}\}$ , the approach yields an expression for

the Wigner function, which only contains moments up to the second order

$$W(q,p) = \frac{1}{\pi \sqrt{(\nu + 1/2)^2 - |\mu|^2}} \times \exp \left[ -\frac{(\nu + 1/2)|\zeta - \langle \hat{a} \rangle|^2 - (\mu^*/2)(\zeta - \langle \hat{a} \rangle)^2 - (\mu/2)(\zeta^* - \langle \hat{a}^\dagger \rangle)^2}{(\nu + 1/2)^2 - |\mu|^2} \right], \quad (2.13)$$

where  $\zeta = q + ip$ ,  $\mu = \langle \hat{a}^2 \rangle - \langle \hat{a} \rangle^2$  and  $\nu = \langle \hat{a}^\dagger \hat{a} \rangle - |\langle \hat{a} \rangle|^2$ . The phase space variables  $p$  and  $q$  are normalized so that  $|\zeta|^2 = p^2 + q^2$  is in units of number of photons. Furthermore, it was shown that the reconstruction is complete on the observation level  $\mathcal{O}_2$ , if  $\nu(\nu + 1) = |\mu|^2$  holds since for such states the associated entropy is zero [40]. Consequently, all pure Gaussian states with  $\nu(\nu + 1) = |\mu|^2$  are fully described by moments up to the second order and the Wigner function is positive.

### 2.1.2 Gaussian quantum microwave states

In this subsection, important types of quantum microwave states are introduced and their basic properties are discussed. Further, the description on the basis of moments and corresponding Wigner functions is presented.

#### Thermal states

Thermal states, emitted by a black body emitter with a certain equilibrium temperature  $T$ , follow the Bose-Planck statistics with a mean photon number

$$\langle \hat{n} \rangle = \text{Tr}(\hat{a}^\dagger \hat{a} \rho_{th}) = \frac{1}{\exp\left(\frac{hf}{k_B T}\right) - 1}, \quad (2.14)$$

for a mode with frequency  $f$ , where  $k_B$  is the Boltzmann constant and  $h$  the Planck constant. For  $T = 0$ , it follows that  $\langle \hat{n} \rangle = 0$ , thus describing a state with zero thermal photons on average. We emphasize that  $\langle \hat{n} \rangle$  describes the thermal occupation of photons. Due to zero-point fluctuations any state, quantum or classical, is at least occupied by 1/2 a photon. Thus, a state for  $T = 0$  is referred to as a vacuum state, where only the zero-point fluctuations are present.

Expressed in the basis of Fock states  $|n\rangle$ , the density operator  $\rho_{th}$  consists only of diagonal elements and reads [44]

$$\rho_{th} = \sum_n \frac{\langle \hat{n} \rangle^n}{(1 + \langle \hat{n} \rangle)^{n+1}} |n\rangle \langle n|. \quad (2.15)$$

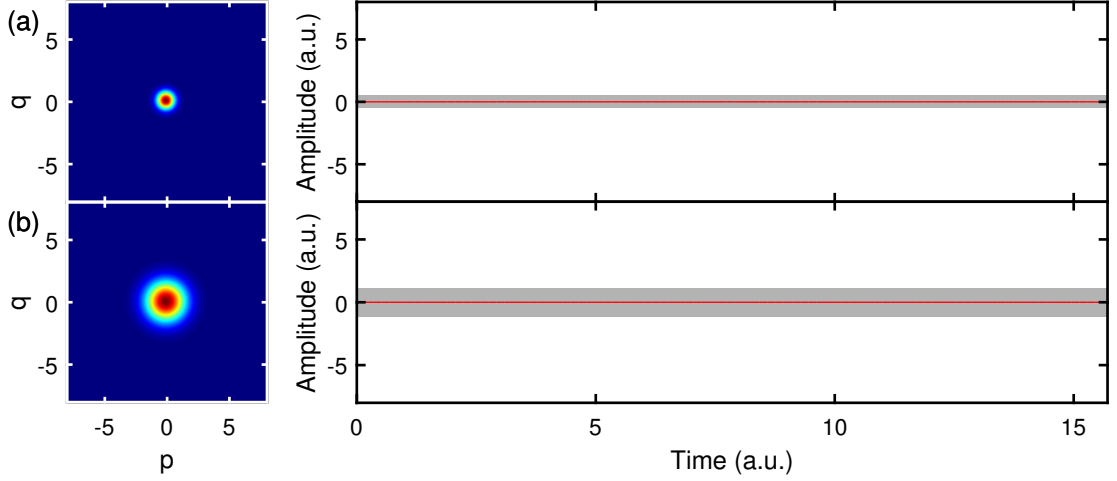


**Figure 2.1:** (a) Vacuum state with  $\langle \hat{n} \rangle = 0$  and (b) thermal state with  $\langle \hat{n} \rangle = 2$ . Left figures show Wigner functions and right figures show the time dependence of the signal amplitude. The red line represents the expectation value and the shaded grey area illustrates the uncertainty for the amplitude at a given time.

Using the density operator one can also find the moments of a thermal state [35]

$$\langle (\hat{a}^\dagger)^m \hat{a}^n \rangle_{th} = \langle \hat{n} \rangle^n n! \delta_{mn}, \quad (2.16)$$

where  $\delta_{mn}$  denotes the Kronecker delta.

It is important to consider thermal states when investigating quantum microwave signals, since thermal states could limit an observation of certain properties of quantum states. To achieve low thermal populations for microwaves in the GHz regime, sub-Kelvin temperatures of an experimental environment are needed. In turn, it is possible to generate thermal states by controlling the temperature of a black body emitter. In the microwave domain, matched  $50 \Omega$  resistors or attenuators are suitable for this purpose.

By inserting the moments of a thermal state from Eq. (2.16) into the general expression Eq. (2.13), it follows that the Wigner function

$$W(q,p) = \frac{1}{\pi \left( \langle \hat{n} \rangle + \frac{1}{2} \right)} \exp \left( - \frac{q^2 + p^2}{\left( \langle \hat{n} \rangle + \frac{1}{2} \right)} \right), \quad (2.17)$$

is rotationally symmetric and it can easily be seen that the variances for the quadratures  $q$  and  $p$  are equal and depend on the mean photon number

$$\langle (\Delta q)^2 \rangle = \langle (\Delta p)^2 \rangle = \frac{\langle \hat{n} \rangle}{2} + \frac{1}{4}. \quad (2.18)$$

Thus, only the vacuum state with  $\langle \hat{n} \rangle = 0$ , corresponding to  $T = 0$  K, is a minimum uncertainty state, exhibiting the equal sign in Eq. (2.2). The variance of thermal states

increases linearly with the mean photon number. Fig. 2.1 shows Wigner functions and timetraces of a signal in a vacuum and a thermal state with  $\langle \hat{n} \rangle = 0$  and  $\langle \hat{n} \rangle = 2$ , respectively. One can clearly see an increased uncertainty of the thermal state in both quadratures indicated by a grey shaded area in the timetraces around the mean value denoted by a red line.

## Coherent states

The displacement operator already introduced in Sec. 2.1.1

$$\hat{D}(\alpha) = \exp(\alpha \hat{a}^\dagger - \alpha^* \hat{a}) \quad (2.19)$$

allows to displace an arbitrary quantum state by the complex amplitude  $\alpha$ . Particularly interesting is the coherent state, which is generated by a displacement of the vacuum state

$$|\alpha\rangle = \hat{D}(\alpha)|0\rangle. \quad (2.20)$$

Schrödinger derived the coherent state as a solution to the Schrödinger equation in 1926 [45] and found that the coherent state satisfies the correspondence principle. For the coherent state a well defined phase operator can be given and it is also a minimum uncertainty state with  $(\Delta q)^2 = (\Delta p)^2 = \frac{1}{4}$ , which makes the coherent state the closest analog to a classical signal. In fact, coherent states are readily generated by commercially available microwave sources.

Using the fact that the coherent state is an eigenfunction of the annihilation operator  $\hat{a}|\alpha\rangle = \alpha|\alpha\rangle$  with the complex eigenvalue  $\alpha = |\alpha|e^{i\Theta} = Q + iP$ , the Wigner function takes the form

$$W(q,p) = \frac{2}{\pi} \exp\left[-2\left((q-Q)^2 + (p-P)^2\right)\right]. \quad (2.21)$$

Thus, the Wigner function of an ideal coherent state is just the Wigner function of the vacuum with the center shifted to  $(Q,P)$  in phase space. In this thesis, we use the angle between displacement direction and the  $p$ -axis  $\theta = \pi/2 - \Theta$ . A coherent state displaced by  $|\alpha|^2 = 16$  photons at the angle of  $\theta = 45^\circ$  is shown in Fig. 2.2. The timetrace illustrates the resemblance between a coherent state and a classical field with a sinusoidal time dependence. One can understand the timetrace by imagining the Wigner function rotating around the origin in time. The probability distribution of the amplitude for each time is then given by the projection of the circle onto the  $q$ -axis, being equal to the marginal distribution  $w(q) = \int_{-\infty}^{\infty} W(q,p)dp$  of the Wigner function. Since the Wigner function of a coherent state is radially invariant, the uncertainty of the amplitude shown in the timetrace is constant in time.

The displacement of an arbitrary input state can be experimentally implemented by a directional coupler acting as a highly asymmetric beam splitter in the microwave regime.

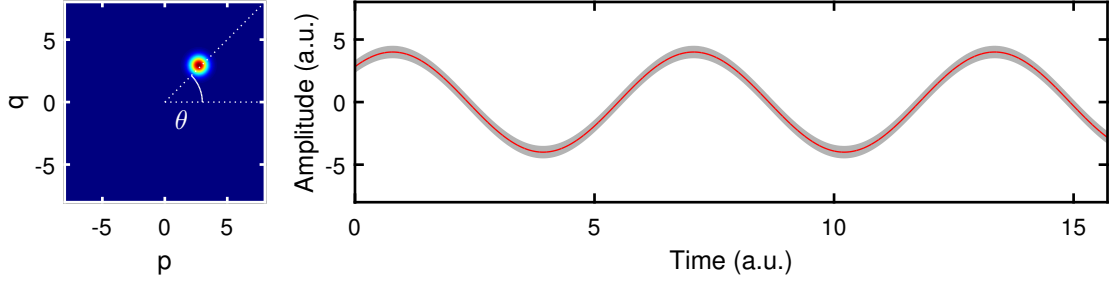


**Figure 2.2:** Coherent state displaced by  $|\alpha|^2 = 16$  with a displacement angle of  $\theta = 45^\circ$ . The left figure shows the Wigner function and the right figure shows the time dependence of the signal amplitude. The red line represents the expectation value and the shaded grey area illustrates the uncertainty for the amplitude at a given time.

The transmitted signal takes the form [29]

$$\hat{a}_{\text{out}} = \sqrt{\tau}\hat{a}_{\text{in}} + \sqrt{1-\tau}\hat{b}_{\text{coh}}, \quad (2.22)$$

where  $\tau$  is the transmissivity,  $\hat{a}_{\text{in}}$  is the state we want to displace, and  $\hat{b}_{\text{coh}}$  a coherent signal incident to the coupled port of the directional coupler corresponding to  $|\tilde{\alpha}\rangle$ .  $\hat{b}_{\text{coh}}$  acts on the coherent state, meaning that  $\hat{b}_{\text{coh}}|\tilde{\alpha}\rangle = \tilde{\alpha}|\tilde{\alpha}\rangle$ , where  $\tilde{\alpha}$  is the eigenvalue. In the limit of high transmissivity  $\tau \rightarrow 1$  and a strong coherent signal  $|\tilde{\alpha}| \gg 1$ , Eq. (2.22) becomes

$$\hat{a}_{\text{out}} \simeq \hat{a}_{\text{in}} + \sqrt{1-\tau}\tilde{\alpha}. \quad (2.23)$$

This is analog to one property of the displacement operator  $\hat{D}(\alpha)$  [30]

$$\hat{D}^\dagger(\alpha)a\hat{D}(\alpha) = a + \alpha, \quad (2.24)$$

with  $\alpha = \sqrt{1-\tau}\tilde{\alpha}$  and, thus, the directional coupler applies a displacement operation to an input state. In Ref. [29] a more detailed theoretical description is given.

## Squeezed states

Apart from vacuum and coherent states, ideal squeezed states are also minimum uncertainty states. But here the uncertainties in different quadrature directions are not equal. Squeezed states are generated by applying a squeezing operator [30]

$$\hat{S}(\xi) = \exp\left(\frac{1}{2}\xi^*\hat{a}^2 - \frac{1}{2}\xi(\hat{a}^\dagger)^2\right), \quad (2.25)$$

with the complex squeeze amplitude  $\xi = re^{i\varphi}$ , to the vacuum

$$|\xi\rangle = \hat{S}(\xi)|0\rangle. \quad (2.26)$$

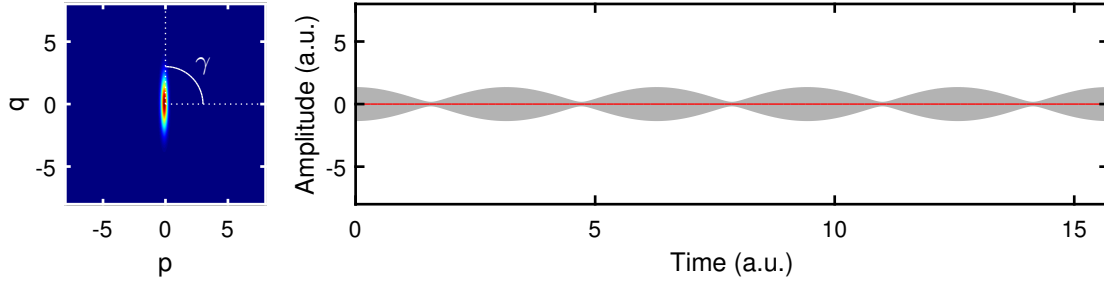


**Figure 2.3:** Squeezed vacuum state with a squeezing angle of  $\gamma = 90^\circ$  and a squeezing amplitude  $r = 1$ , corresponding to a squeezing of  $\mathcal{S} = 8.7$  dB below the vacuum. Left figure shows the Wigner function and the right figure shows the time dependence of the signal amplitude of the states. The red line represents the expectation value and the shaded grey area illustrates the uncertainty for the amplitude at a given time.

The phase  $\varphi$  is related to the angle of the squeezed and anti-squeezed quadrature components. In the following we use the squeezing angle  $\gamma = -\varphi/2$  between the anti-squeezed quadrature direction and the  $p$ -axis in the phase-space representation. The squeezing factor  $r$  quantifies the amount of squeezing. The variances for a squeezed vacuum state along the squeezed and anti-squeezed quadratures are  $e^{-2r}/4$  and  $e^{2r}/4$ , respectively. At this point it is also useful to define a squeezing level in decibel as

$$\mathcal{S} = -10 \log_{10} \left[ (\Delta X_{\text{sq}})^2 / 0.25 \right], \quad (2.27)$$

where we compare the variance of the squeezed quadrature  $(\Delta X_{\text{sq}})^2$  with the vacuum variance.  $(\Delta X_{\text{sq}})^2$  can also be expressed in terms of the signal moments up to second order [44], resulting in the expression

$$\mathcal{S} = -10 \log_{10} \left[ \langle \hat{a}^2 \rangle e^{-i\varphi} + \langle (\hat{a}^\dagger)^2 \rangle e^{i\varphi} + 2\langle \hat{a}^\dagger \hat{a} \rangle + 1 - \langle \hat{a} \rangle^2 e^{-i\varphi} - \langle \hat{a}^\dagger \rangle^2 e^{i\varphi} - 2\langle \hat{a}^\dagger \rangle \langle \hat{a} \rangle \right]. \quad (2.28)$$

For an ideal squeezer with vacuum as an input state, the squeezing would be  $\mathcal{S}_{\text{ideal}} = 20r \log_{10}(e)$ . Therefore a positive squeezing  $\mathcal{S}$  means squeezing below the vacuum and larger  $\mathcal{S}$  means higher squeezing.  $\mathcal{S} < 0$  indicates that the state is not squeezed below vacuum but nevertheless it gives information about the quadrature variance.

The Wigner function of a squeezed vacuum state takes the form

$$W(q,p) = \frac{2}{\pi} \exp \left[ -(e^{2r} + e^{-2r})|q+ip|^2 - \frac{1}{2}(e^{2r} - e^{-2r})e^{-i\varphi}(q+ip)^2 - \frac{1}{2}(e^{2r} - e^{-2r})e^{i\varphi}(q-ip)^2 \right], \quad (2.29)$$

where the  $1/e$  contour takes the form of an ellipse around the origin in phase space. An example for a squeezed vacuum state is shown in Fig. 2.3. When imagining the squeezed state rotating around the origin, the marginal distribution  $w(q)$  is changing in time. This

results in an oscillating uncertainty of the amplitude above and below the one of the vacuum state. Furthermore, the timetrace illustrates that one needs more than the first order moments of the signal to obtain full information about the squeezed state, since first order moments only give the mean value of the amplitude which is zero.

## Squeezed coherent states

In general, there are two possibilities to generate squeezed coherent states. They differ in the order of applying the squeezing  $\hat{S}(\xi)$  and the displacement operators  $\hat{D}(\alpha)$  to the vacuum state. Let us consider the case where we first squeeze the vacuum and then displace the squeezed state. The displaced squeezed coherent state then reads

$$|\alpha, \xi\rangle = \hat{D}(\alpha)\hat{S}(\xi)|0\rangle, \quad (2.30)$$

where  $\xi = re^{i\varphi}$  and  $\alpha = |\alpha|e^{i\Theta}$ . In this order, the displacement of the final state is independent of the previous squeezing parameters  $r$  and  $\varphi$  and is solely given by  $\alpha$ . By changing the order to  $\hat{S}(\xi)\hat{D}(\alpha)|0\rangle$ , the final displacement depends on the squeezing parameters and we refer the reader to a deeper theoretical description in Ref. [44] or an experimental implementation in the microwave regime in Ref. [24].

The moments for an ideal displaced squeezed state with a displacement operation after the squeezing of the vacuum are

$$\langle \hat{a} \rangle = \alpha, \quad (2.31)$$

$$\langle \hat{a}^2 \rangle = \alpha^2 - e^{i\varphi} \sinh r \cosh r, \quad (2.32)$$

$$\langle \hat{a}^\dagger \hat{a} \rangle = |\alpha|^2 + \sinh^2 r, \quad (2.33)$$

$$\langle \hat{a}^3 \rangle = \alpha^3 - 3\alpha e^{i\varphi} \sinh r \cosh r, \quad (2.34)$$

$$\langle \hat{a}^\dagger \hat{a}^2 \rangle = |\alpha|^2 \alpha + 2\alpha \sinh^2 r - \alpha^* e^{i\varphi} \sinh r \cosh r, \quad (2.35)$$

$$\langle \hat{a}^4 \rangle = \alpha^4 - 6\alpha^2 e^{i\varphi} \sinh r \cosh r + 3e^{2i\varphi} \sinh^2 r \cosh^2 r, \quad (2.36)$$

$$\langle \hat{a}^\dagger \hat{a}^3 \rangle = |\alpha|^2 \alpha^2 + 3\alpha^2 \sinh^2 r - 3|\alpha|^2 e^{i\varphi} \sinh r \cosh r - 3e^{i\varphi} \sinh^3 r \cosh r, \quad (2.37)$$

$$\begin{aligned} \langle \hat{a}^{\dagger 2} \hat{a}^2 \rangle &= |\alpha|^4 - \alpha^2 e^{-i\varphi} \sinh r \cosh r - \alpha^{*2} e^{i\varphi} \sinh r \cosh r \\ &\quad + 4|\alpha|^2 \sinh^2 r + \sinh^2 r \cosh^2 r. \end{aligned} \quad (2.38)$$

Other moments with  $m + n \leq 4$  are calculated via  $\langle (\hat{a}^\dagger)^m \hat{a}^n \rangle = \langle (\hat{a}^\dagger)^n \hat{a}^m \rangle^*$ . By setting  $r$  or  $\alpha$  to zero one can also use these expressions to obtain the moments for coherent or squeezed states, respectively.

The Wigner function of a displaced squeezed state is the same as for a squeezed state but shifted by the displacement  $\alpha = |\alpha|e^{i\Theta} = Q + iP$ . This corresponds to the operation  $p \rightarrow p - P$  and  $q \rightarrow q - Q$  in Eq. (2.29). Various squeezed vacuum states with different displacement angles  $\theta$  but with a fixed squeezing angle  $\gamma = 90^\circ$  are shown in

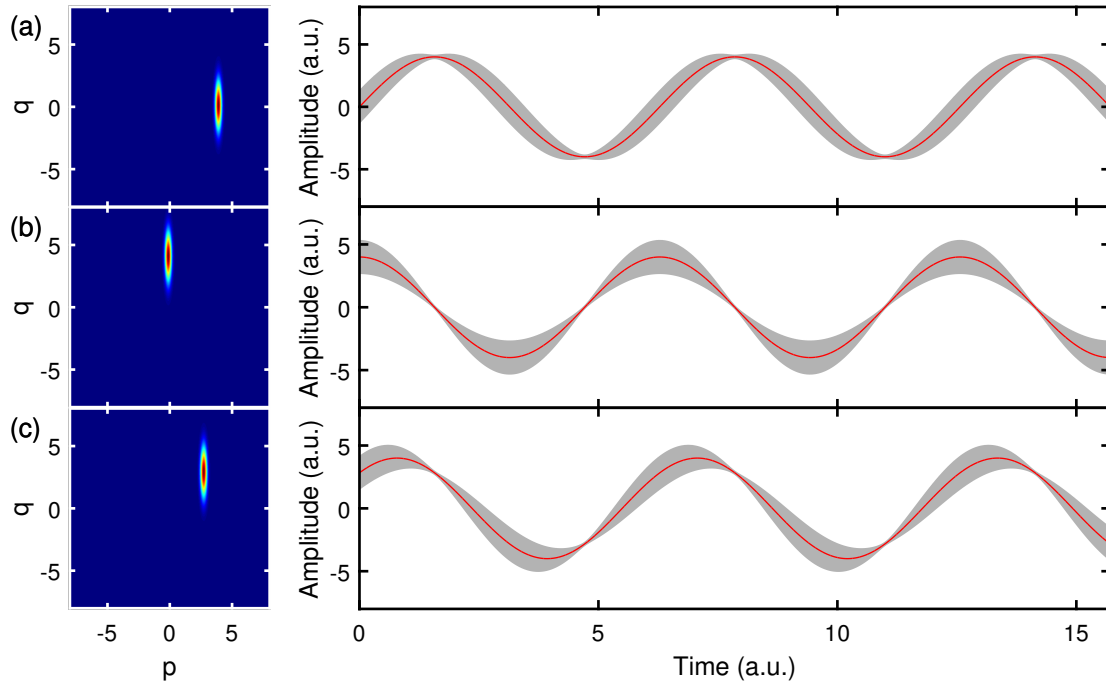


**Figure 2.4:** Various squeezed vacuum states displaced by  $|\alpha|^2 = 16$  photons with different displacement angles  $\theta$ , squeezing angle  $\gamma = 90^\circ$  and  $r = 1$ . Left figures show Wigner functions and right figures show the time dependence of the signal amplitude for the respective states. The red line represents the expectation value and the shaded grey area illustrates the uncertainty for the amplitude at a given time. (a) Amplitude squeezed state with  $\theta = 0^\circ$ , (b) Phase squeezed state with  $\theta = 90^\circ$  and (c) mixture of amplitude and phase squeezed state with  $\theta = 45^\circ$ .

Fig. 2.4. Subfigures (a) and (b) represent amplitude squeezed and phase squeezed states, respectively, whereas (c) is a mixture of both. The uncertainty in amplitude for each shown timetrace exhibits different time dependencies while the expectation value is the same as for a coherent state.

### 2.1.3 Dual-path state reconstruction method

Depending on the quantum state under investigation, there exist various methods to detect certain properties of a quantum state. In the optical domain quantum correlations are routinely measured by optical homodyning [31], using the fact, that optical photons have vacuum temperatures much higher than room temperatures, allowing for efficient single photon detectors. In the microwave regime, these techniques can not be easily implemented due to a low energy of microwave photons. The lack of efficient single microwave photon detectors requires the use of linear amplifiers. Due to the uncertainty principle, phase-insensitive linear amplifiers add at least half a photon of noise to the signal [16]. To avoid this issue, one can use phase-sensitive amplifiers to amplify only one field quadrature and add less than half a photon of noise to it [46].

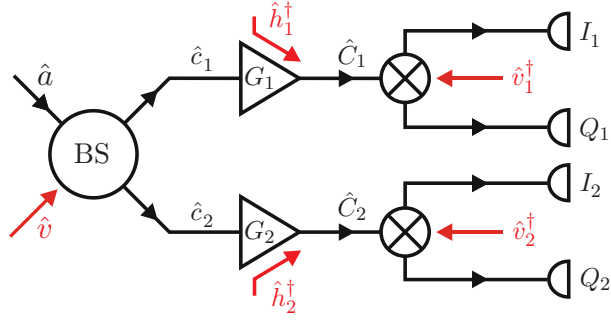


**Figure 2.5:** Scheme of the dual-path reconstruction method. The signal  $\hat{a}$  and a weak thermal state  $\hat{v}$  are incident on a hybrid ring, acting as beam splitter (BS). Each path is amplified by  $G_{1,2}$ , adding uncorrelated noise  $\hat{h}_{1,2}^\dagger$  to the signal. The quadratures  $\hat{I}_{1,2}$  and  $\hat{Q}_{1,2}$  for each path are obtained via IQ-demodulation, adding the noise  $\hat{v}_{1,2}^\dagger$  and subsequently measured.

An alternative way to detect quantum microwave signals makes use of phase-insensitive amplifiers, which add a substantial amount of noise photons. In Refs. [47, 48] a single amplification path is used to reconstruct the signal moments, whereas the vacuum is used as a reference state to account for the added noise of the amplification path. Another approach is based on the idea of splitting the signal into two paths and measuring cross-correlations between them (see Fig. 2.5). This approach bears the name "dual-path state reconstruction". It has been recently developed at WMI and applied for the detection of propagating quantum signals [17–19, 49]. In this thesis we make use of the dual-path detection method and explain the scheme in more detail below.

The basic operation principle is depicted in Fig. 2.5 where a signal  $\hat{a}$  is equally split by a hybrid ring (which functions as a 50:50 beam splitter for microwaves) and then each path is individually amplified, adding uncorrelated noise  $\hat{h}_{1,2}^\dagger$  to the signal. Afterwards each amplified signal is split into its quadratures  $I_{1,2}$  and  $Q_{1,2}$  by an IQ-mixer, again adding noise  $\hat{v}_{1,2}^\dagger$ , and finally detected.

Using the beam splitter relations

$$\begin{pmatrix} \hat{c}_1 \\ \hat{c}_2 \end{pmatrix} = \frac{1}{\sqrt{2}} \begin{pmatrix} 1 & 1 \\ -1 & 1 \end{pmatrix} \begin{pmatrix} \hat{a} \\ \hat{v} \end{pmatrix}, \quad (2.39)$$

one obtains a superposition of the signal  $\hat{a}$  and the reference state  $\hat{v}$ . The dual-path reconstruction assumes full knowledge of this reference state. In our experiments, a natural choice for the reference state is a weak thermal state with a temperature around 25 mK. According to quantum theory for linear amplifiers [16] the amplification by  $G_{1,2}$  adds a certain amount of noise, represented by a bosonic creation operator  $\hat{h}_{1,2}^\dagger$ , to the signal

$$\hat{C}_{1,2} = \sqrt{\frac{G_{1,2}}{2}} (\pm \hat{a} + \hat{v}) + \sqrt{G_{1,2} - 1} \hat{h}_{1,2}^\dagger. \quad (2.40)$$

Finally, by taking into account the IQ-mixer, one arrives at

$$\hat{\xi}_1 = \sqrt{\frac{G_1}{2}}(+\hat{a} + \hat{v}) + \sqrt{G_1 - 1}\hat{h}_1^\dagger + \hat{v}_1^\dagger, \quad (2.41)$$

$$\hat{\xi}_2 = \sqrt{\frac{G_2}{2}}(-\hat{a} + \hat{v}) + \sqrt{G_2 - 1}\hat{h}_2^\dagger + \hat{v}_2^\dagger, \quad (2.42)$$

where we introduced the unitless complex envelope function  $\xi_{1,2}$ . It is defined by the relation

$$\hat{\xi}_{1,2} \equiv (\hat{I}_{1,2} + i\hat{Q}_{1,2}) / \sqrt{\kappa}, \quad (2.43)$$

where  $\hat{I}_{1,2}$  and  $\hat{Q}_{1,2}$  are the corresponding operators of the measured quadratures and  $\kappa$  is the photon number conversion factor, relating the measured quadratures to number of photons (see Sec. 3.2.3).

Introducing

$$\hat{V}_{1,2} \equiv \sqrt{\frac{2}{G_{1,2}}}(\sqrt{G_{1,2} - 1}\hat{h}_{1,2} + \hat{v}_{1,2}), \quad (2.44)$$

$$\hat{S}_{1,2} \equiv \sqrt{\frac{2}{G_{1,2}}}\hat{\xi}_{1,2}, \quad (2.45)$$

we obtain from Eqs. (2.41) and (2.42)

$$\hat{S}_1 = +\hat{a} + \hat{v} + \hat{V}_1^\dagger, \quad (2.46)$$

$$\hat{S}_2 = -\hat{a} + \hat{v} + \hat{V}_2^\dagger, \quad (2.47)$$

where the signal  $\hat{S}_{1,2}$  is now referred to the input of the hybrid ring.

With Eqs. (2.43) and (2.45) it is possible to relate the measured quadratures  $\langle \hat{I}_1^j \hat{I}_2^k \hat{Q}_1^m \hat{Q}_2^n \rangle$  to  $\langle (\hat{S}_1^\dagger)^{j'} (\hat{S}_2^\dagger)^{k'} \hat{S}_1^{m'} \hat{S}_2^{n'} \rangle$ . This enables us to calculate the signal moments  $\langle (\hat{a}^\dagger)^r \hat{a}^l \rangle$  in a recursive fashion. For a more detailed description we refer the reader to Ref. [49] or [19]. Theoretically, this approach allows for the calculation of moments up to an arbitrary order with  $r, l \in \mathbb{N}_0$ , enabling one to calculate the Wigner function according to Eq. (2.12) and therefore fully describe an arbitrary quantum state. In this thesis we calculate the signal moments only up to the fourth order  $r + l \leq 4$ . This is equivalent to a calculation of the measured quadrature moments up to the fourth order  $j + k + m + n \leq 4$ . For Gaussian states only signal moments up to the second order are required for full state reconstruction and the Wigner function is given by Eq. (2.13). To verify that the measured states are Gaussian, we evaluate the cumulants up to fourth order as described in Appendix B. For pure Gaussian states only the cumulants up to the second order are non-zero and all higher orders vanish.

## 2.2 The Josephson Parametric Amplifier

As the name already suggests, the Josephson Parametric Amplifier (JPA) is a parametric device which allows to modulate one of its respective parameters, which, in turn, may lead to a parametric amplification of an input signal. A flux-driven JPA consists of a superconducting microwave resonator in a coplanar waveguide (CPW) geometry. By terminating the microwave resonator on one side to the ground plane via a direct current superconducting quantum interference device (dc-SQUID), the resonant frequency can be tuned by an external magnetic flux applied to the dc-SQUID loop. In the following we introduce the physics relevant for a description of the flux-driven JPA.

### 2.2.1 Josephson junctions

Both the microwave resonator and the dc-SQUID consist of superconducting materials, namely niobium and aluminum, respectively. An important property of the superconducting state is the Meissner-Ochsenfeld effect, where magnetic fields are expelled from the bulk material below the transition temperature. One consequence of this effect is the perfect conductivity of a superconductor, which makes superconducting materials a natural choice for building resonators and, thus, minimizing resistive losses. Since superconductivity is a quantum phenomenon manifesting on macroscopic scales, various interesting effects such as the Josephson effect can be observed. The Josephson effect which was first theoretically predicted by Josephson [50] is observed for two weakly coupled superconductors and originates from an overlap of the macroscopic wave functions of each superconductor

$$\Psi_{1,2}(\mathbf{r},t) = \sqrt{n_{1,2}^*(\mathbf{r},t)} e^{i\theta_{1,2}(\mathbf{r},t)}, \quad (2.48)$$

where the indices 1 and 2 represent superconductor 1 and 2, respectively.  $\sqrt{n_i^*(\mathbf{r},t)}$  is the density of superconducting Cooper pairs, and  $\theta_i(\mathbf{r},t)$  is the global phase of the wave function for each superconductor. One way to establish such a weak link is to place an insulating layer between the two superconductors (see Fig. 2.6 (a)).

The gauge invariant phase difference between the two superconductors is [51]

$$\varphi(\mathbf{r},t) = \theta_2(\mathbf{r},t) - \theta_1(\mathbf{r},t) - \frac{2\pi}{\Phi_0} \int_1^2 \mathbf{A}(\mathbf{r},t) \cdot d\mathbf{l}, \quad (2.49)$$

where  $\Phi_0 = \frac{h}{2e}$  is the magnetic flux quantum and  $\mathbf{A}(\mathbf{r},t)$  is a magnetic vector potential. The integration path is along a line from superconductor 1 to superconductor 2. For simplicity, we consider only lumped Josephson junctions, where the supercurrent density and the phase difference is spatially homogeneous in the junction area. The first Josephson equation, also called the current-phase relation, describes the supercurrent  $I_s$  through the Josephson junction

$$I_s(\varphi) = I_c \sin(\varphi), \quad (2.50)$$

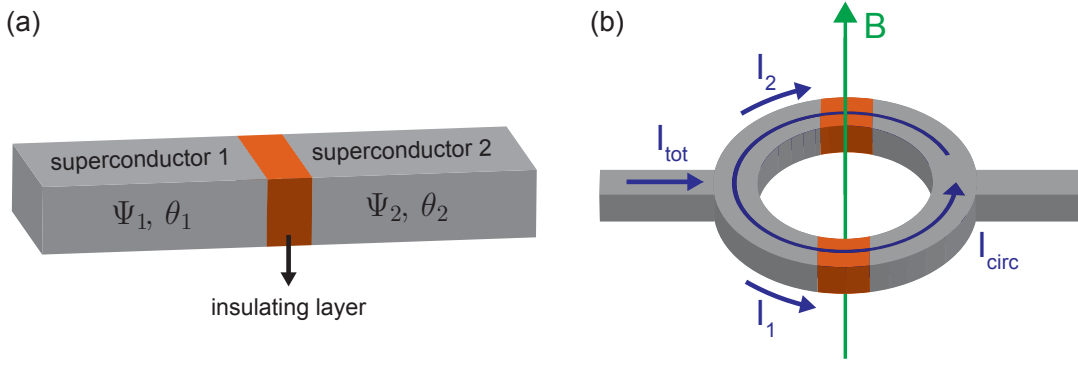


**Figure 2.6:** (a) Josephson junction with superconductors in grey and insulating barrier in orange. (b) dc-SQUID with total transport current  $I_{tot}$ , circulating current  $I_{circ}$ , currents through each arm  $I_{1,2}$  and magnetic field  $B$  through the SQUID loop.

where  $I_c$  is the critical Josephson current.

The second Josephson equation relates the voltage  $V$  across the Josephson junction to the derivative of the phase difference

$$\frac{\partial \varphi}{\partial t} = \frac{2\pi}{\Phi_0} V(t), \quad (2.51)$$

and is therefore called the voltage-phase relation. By applying a constant voltage across the Josephson junction, the phase difference increases linearly in time

$$\varphi(t) = \varphi_0 + \frac{2\pi}{\Phi_0} V \cdot t, \quad (2.52)$$

and according to the first Josephson equation this leads to a sinusoidal oscillation of the supercurrent  $I_s$ . In turn, if no voltage is applied across the Josephson junction, the phase difference stays constant in time, resulting in a dc supercurrent depending on the phase difference  $\varphi$ .

Due to the finite overlap of the wave functions, there is a binding energy  $E_J$  called the Josephson coupling energy associated with the Josephson junction

$$E_J(\varphi) = \frac{\Phi_0 I_c}{2\pi} (1 - \cos \varphi) = E_{J0} (1 - \cos \varphi), \quad (2.53)$$

where  $E_{J0} = \Phi_0 I_c / (2\pi)$ . When a current  $I_s$ , acting as a generalized force, is flowing through a Josephson junction the potential energy is given by the tilted washboard potential

$$E_{pot}(\varphi) = E_J(\varphi) - I_s \left( \frac{\Phi_0}{2\pi} \varphi \right) = E_{J0} \left( 1 - \cos \varphi - \frac{I_s}{I_c} \varphi \right). \quad (2.54)$$

The phase difference  $\varphi$  can be considered as a classical particle inside this potential. For  $|I| < I_c$  the particle resides in one of the local minima of the potential. For  $|I| > I_c$ ,

no local minima exist anymore and the particle will move down the potential. For these two scenarios, the Josephson junction is in the zero-voltage and the voltage state, respectively. A more detailed model of the Josephson junction is the so called Resistively and Capacitively Shunted Junction (RCSJ) model, taking into account a finite capacitance  $C$  and a normal resistance  $R$ , yielding an equation of motion for the phase difference [52, 53]

$$\frac{\ddot{\varphi}}{\omega_p^2} + \frac{\dot{\varphi}}{\omega_c} = j - \sin \varphi = -\frac{1}{E_{J0}} \frac{\partial E_{\text{pot}}(\varphi)}{\partial \varphi}, \quad (2.55)$$

where  $\omega_p = \sqrt{2\pi I_c / \Phi_0 C_s}$  is the plasma frequency,  $\omega_c = 2\pi I_c R_s / \Phi_0$  is a characteristic frequency and  $j = I_s / I_c$  is the normalized current through the Josephson junction. By neglecting the resistive term and using the kinetic energy  $K(\dot{\varphi})$  corresponding to the first term on the left hand side, one can write down a Lagrangian for the Josephson junction

$$\mathcal{L} = K(\dot{\varphi}) - E_{\text{pot}}(\varphi) = \frac{\hbar^2 \dot{\varphi}^2}{4E_C} - E_{J0} (1 - \cos \varphi - j\varphi), \quad (2.56)$$

where  $E_C = (2e)^2 / 2C_s$  is the charging energy of the capacitor corresponding to one Cooper pair. The equation of motion

$$\frac{d}{dt} \frac{\partial \mathcal{L}}{\partial \dot{\varphi}} - \frac{\partial \mathcal{L}}{\partial \varphi} = 0 \quad (2.57)$$

can readily be derived from the Lagrangian.

By using the two Josephson equations and the definition of the inductance  $V = L \frac{dI_s}{dt}$ , one arrives at an expression for a non-linear inductance of a Josephson junction

$$L_s = \frac{\Phi_0}{2\pi I_c \cos \varphi} = L_c \frac{1}{\cos \varphi}, \quad (2.58)$$

where  $L_c = \frac{\Phi_0}{2\pi I_c}$  corresponds to the minimal inductance of the Josephson junction.

### 2.2.2 Dc-SQUID

A direct current quantum interference device (dc-SQUID) consists of a superconducting loop biased by a transport current  $I_{\text{tot}}$ , as shown in Fig. 2.6 (b). Each arm of the loop incorporates a Josephson junction with a current  $I_{1,2}$  flowing through it. A magnetic field  $\mathbf{B}$  is applied through the loop, resulting in a magnetic flux  $\Phi_{\text{ext}}$ . The total phase change along a closed contour  $C$  around the dc-SQUID loop needs to be  $2\pi n$  with  $n \in \mathbb{N}_0$

$$\oint_C \nabla \theta = 2\pi n. \quad (2.59)$$

To evaluate the integral, we use the gauge invariant phase difference across the Josephson junctions in Eq. (2.49) as well as the phase gradient in the bulk superconductor [51]

$$\nabla\theta = \frac{2\pi}{\Phi_0}(\Lambda\mathbf{J}_s + \mathbf{A}), \quad (2.60)$$

where  $\mathbf{J}_s$  is the supercurrent density,  $\mathbf{A}$  is the vector potential and  $\Lambda = m^*/n_s^*q^{*2}$  is the London parameter with superconducting particles of mass  $m^*$ , density  $n_s^*$  and charge  $q^*$ . If the integration path is deeper inside the bulk superconductor than the London penetration depth, one can neglect the terms with  $\mathbf{J}_s$  and obtains the condition

$$\varphi_2 - \varphi_1 = \frac{2\pi\Phi}{\Phi_0} + 2\pi n. \quad (2.61)$$

This generates a link between the phase differences  $\varphi_{1,2}$  across the junctions and the total magnetic flux  $\Phi$  through the loop. The total magnetic flux is determined by the externally applied flux and a contribution originating from the self inductance  $L_{\text{loop}}$  of the superconducting loop

$$\Phi = \Phi_{\text{ext}} + L_{\text{loop}}I_{\text{circ}}, \quad (2.62)$$

where we introduced the circulating current

$$I_{\text{circ}} = \frac{I_1 - I_2}{2} = I_c \cos\left(\frac{\varphi_1 + \varphi_2}{2}\right) \sin\left(\frac{\varphi_1 - \varphi_2}{2}\right) = -I_c \cos\varphi_+ \sin\varphi_-. \quad (2.63)$$

We also introduced new phase differences

$$\varphi_+ \equiv \frac{\varphi_1 + \varphi_2}{2}, \quad (2.64)$$

$$\varphi_- \equiv \frac{\varphi_2 - \varphi_1}{2}, \quad (2.65)$$

to simplify the notation.

Now we can write the total flux in the form

$$\frac{\Phi}{\Phi_0} = \frac{\Phi_{\text{ext}}}{\Phi_0} - \frac{\beta_L}{2} \cos\varphi_+ \sin\varphi_-, \quad (2.66)$$

where a screening parameter

$$\beta_L \equiv \frac{2L_{\text{loop}}I_c}{\Phi_0}, \quad (2.67)$$

relates the maximal induced flux  $L_{\text{loop}}I_c$  by the circulating current  $I_c$  to half of a flux quantum  $\Phi_0/2$ .

The total transport current is given by the sum of the currents through each arm

$$I_{\text{tot}} = I_1 + I_2 = 2I_c \sin\left(\frac{\varphi_1 + \varphi_2}{2}\right) \cos\left(\frac{\varphi_1 - \varphi_2}{2}\right) = 2I_c \sin\varphi_+ \cos\varphi_-. \quad (2.68)$$

Furthermore, the fluxoid quantization with the new phase difference (2.65) reads

$$\varphi_- = \pi \frac{\Phi}{\Phi_0} + \pi n. \quad (2.69)$$

For the case  $\beta_L \approx 0$ , the self inductance  $L_{\text{loop}}$  of the dc-SQUID loop can be neglected and Eq. (2.66) simplifies to  $\Phi \approx \Phi_{\text{ext}}$ . Then the maximum supercurrent is given by the expression [52]

$$I_c^{\text{max}}(\Phi_{\text{ext}}) = 2I_c \left| \cos \left( \pi \frac{\Phi_{\text{ext}}}{\Phi_0} \right) \right|. \quad (2.70)$$

This means that in this case the dc-SQUID can be considered as a single Josephson junction with a flux-modulated maximum supercurrent and thus, in analogy to Eq. (2.58), an inductance for the dc-SQUID can be defined [54]

$$L_{c,\text{SQUID}}(\Phi_{\text{ext}}) = \frac{\Phi_0}{2\pi I_c^{\text{max}}} = \frac{\Phi_0}{4\pi I_c \left| \cos \left( \pi \frac{\Phi_{\text{ext}}}{\Phi_0} \right) \right|}. \quad (2.71)$$

For the case  $\beta_L > 0$ , the self inductance of the loop cannot be neglected anymore. Therefore, the full Eqs. (2.66) and (2.68) describe the behavior of the dc-SQUID and need to be solved self-consistently under the constraint of Eq. (2.61). In general, it is not possible to give an analytic expression but nevertheless it is convenient to write

$$I_c^{\text{max}}(\Phi_{\text{ext}}) = 2I_c \cdot j_c(\Phi_{\text{ext}}), \quad (2.72)$$

$$L_{c,\text{SQUID}}(\Phi_{\text{ext}}) = \frac{\Phi_0}{4\pi I_c \cdot j_c(\Phi_{\text{ext}})}, \quad (2.73)$$

where  $j_c(\Phi_{\text{ext}})$  is a dimensionless normalized critical supercurrent through the dc-SQUID. We refer the reader to Sec. 4.1 for a detailed discussion of  $j_c(\Phi_{\text{ext}})$ . It should also be noted, that  $j_c(\Phi_{\text{ext}})$ , in general, is a multi-valued function of  $\Phi_{\text{ext}}$ . It also depends on the history of the phase particle movement in the dc-SQUID potential.

Similarly to the case of one Josephson junction, one can write Kirchhoff's law for both junctions

$$\frac{\ddot{\varphi}_1}{\omega_{p1}^2} + \frac{\dot{\varphi}_1}{\omega_{c1}} = -\sin \varphi_1 + j + \frac{1}{\pi\beta_L}(\varphi_2 - \varphi_1 - 2\pi\varphi_{\text{ext}}), \quad (2.74)$$

$$\frac{\ddot{\varphi}_2}{\omega_{p2}^2} + \frac{\dot{\varphi}_2}{\omega_{c2}} = -\sin \varphi_2 + j - \frac{1}{\pi\beta_L}(\varphi_2 - \varphi_1 - 2\pi\varphi_{\text{ext}}), \quad (2.75)$$

where the indices 1 and 2 denote the two Josephson junctions,  $\varphi_{\text{ext}} = \Phi_{\text{ext}}/\Phi_0$ ,  $j = I_{\text{tot}}/(2I_c)$ . The sum of the second and the third term on the right hand side is equal to  $I_i/I_c$  for junctions 1 and 2, respectively<sup>1</sup>. Neglecting the dissipative terms and assuming

<sup>1</sup>This can be seen by using Eqs. (2.63) and (2.68) to express  $I_i$  in terms of  $I_{\text{tot}}$  and  $I_{\text{circ}}$  and then use Eqs. (2.62) and (2.61) to replace  $I_{\text{circ}}$ .

that both junctions have the same critical current  $I_c$ , the Lagrangian of a dc-SQUID is given by

$$\mathcal{L} = \frac{\hbar^2}{4E_C}(\dot{\varphi}_1^2 + \dot{\varphi}_2^2) - E_{J0}(2 - \cos \varphi_1 - \cos \varphi_2 - j(\varphi_1 + \varphi_2)) - \frac{E_{J0}}{2\pi\beta_L}(\varphi_2 - \varphi_1 - 2\pi\varphi_{\text{ext}})^2, \quad (2.76)$$

which can also be written in the form

$$\mathcal{L} = \frac{\hbar^2}{2E_C}(\dot{\varphi}_+^2 + \dot{\varphi}_-^2) - E_{J0}(2 - 2\cos \varphi_+ \cos \varphi_- - 2j\varphi_+) - \frac{2E_{J0}}{\pi\beta_L}(\varphi_- - \pi\varphi_{\text{ext}})^2. \quad (2.77)$$

### 2.2.3 Coplanar waveguide resonator

Another important part of the JPA is a coplanar waveguide resonator. Since the dimensions of the resonator are comparable to the wavelength of the microwave field, one needs to use a distributed-element model to describe the resonator correctly. For a detailed description, we refer the reader to Ref. [55]. For a homogeneously distributed, lossless transmission line, the characteristic impedance is given by

$$Z = \sqrt{\frac{L'}{C'}}, \quad (2.78)$$

where  $L'$  and  $C'$  are the inductance and capacitance per unit length, respectively. The phase velocity of an electromagnetic waves inside the transmission line is

$$v_p = \frac{1}{\sqrt{L'C'}}, \quad (2.79)$$

from which, one can find a frequency  $\omega$  for a given wavelength  $\lambda$

$$\omega = \frac{2\pi}{\lambda\sqrt{L'C'}}. \quad (2.80)$$

By considering a transmission line, which is short-circuited to the ground after a certain length  $d$  and coupled to an input line via a coupling capacitance  $C_c$ , one obtains a reflection-type resonator. Such a resonator is often called a  $\lambda/4$  resonator, since the wavelength of a fundamental mode  $\lambda = 4d$  is four times the length of the resonator. With Eq. (2.80), one obtains the resonant frequency of the fundamental mode

$$\omega_0 = \frac{2\pi}{4d\sqrt{L'C'}} = \frac{\pi}{2\sqrt{LC}}, \quad (2.81)$$

where  $L = L'd$  and  $C = C'd$  are the total inductance and capacitance of the resonator, respectively. Since an ideal resonator is harmonic, the frequency of higher modes is given by  $(2n + 1) \cdot \omega_0$  with  $n \in \mathbb{N}_0$ .

There exist several approaches to experimentally characterize a resonator. In the case of a  $\lambda/4$  resonator, the reflection coefficient  $\Gamma$  is an important quantity. Imagine a traveling microwave signal with amplitude  $a_{\text{in}}$  from a region with impedance  $Z_0$  to another one with an input impedance  $Z_{\text{in}}$  (see Fig. 2.7). Then part of the signal is reflected back, giving rise to an output signal with amplitude  $a_{\text{out}}$ . The ratio between the amplitude of the back reflected signal  $a_{\text{out}}$  and the input signal  $a_{\text{in}}$  is called the reflection coefficient [55]

$$\Gamma = \frac{a_{\text{out}}}{a_{\text{in}}} = \frac{Z_{\text{in}} - Z_0}{Z_{\text{in}} + Z_0}. \quad (2.82)$$

Finding an expression for the frequency dependent input impedance  $Z_{\text{in}}(\omega)$ , allows to calculate  $\Gamma(\omega)$ . To this end the resonator can be modeled by lumped-elements, whereas a description based on distributed elements is also possible and provides more accurate results in the microwave regime [55] (see Fig. 2.7 (a,b)). In analogy to a cavity in quantum optics (see Fig. 2.7 c)), one can also consider the microwave resonator to be a cavity with reflective mirrors, which allows one to use the input-output formalism to calculate the reflection coefficient [56]

$$\Gamma = \frac{(\omega - \omega_0)^2 + i\kappa_2(\omega - \omega_0) + \frac{\kappa_1^2 - \kappa_2^2}{4}}{(\omega - \omega_0 + i\frac{\kappa_1 + \kappa_2}{2})^2}, \quad (2.83)$$

where

$$\kappa_1 = \frac{\omega_0}{Q_{\text{ext}}}, \quad (2.84)$$

$$\kappa_2 = \frac{\omega_0}{Q_{\text{int}}}, \quad (2.85)$$

are the coupling rates to the input line and a loss port, respectively. Here we also introduced an external quality factor  $Q_{\text{ext}}$  and an internal quality factor  $Q_{\text{int}}$ .

The external quality factor  $Q_{\text{ext}}$  is mainly determined by the coupling capacitance  $C_c$  and describes how strongly the resonator is coupled to the input port. For a weak coupling, the external quality factor is high and vice versa.

The internal quality factor  $Q_{\text{int}}$  describes internal losses of the resonator originating from several loss mechanisms. Microwave losses at milli-Kelvin temperatures are usually caused by two level systems (TLS) residing on the surface of the superconductor or in the dielectric [57]. A finite surface resistance of superconductors at microwave frequencies also contributes to internal losses of a superconducting resonator. Since experiments are done at a finite temperature, there is always a finite amount of excited quasi-particles. They can also interact with the microwave signals and lead to additional dissipation [58]. Another loss mechanism are radiation losses, which dependent on the geometry of the waveguide [59].

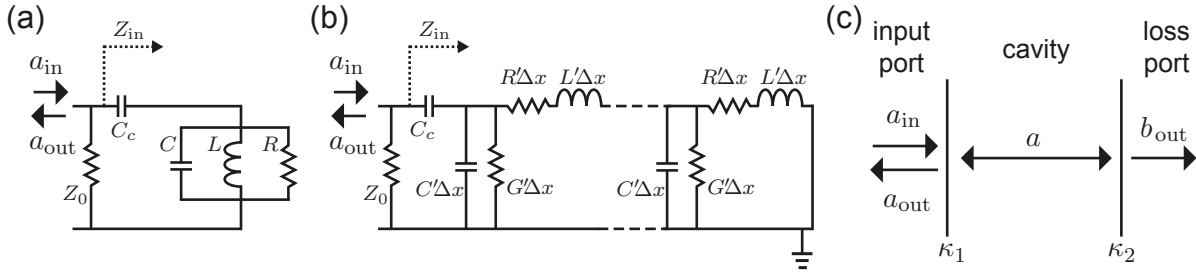


**Figure 2.7:** Different models for microwave resonators with input signal of amplitude  $a_{\text{in}}$  and output signal of amplitude  $a_{\text{out}}$ .  $Z_0$  denotes the impedance of the input line and  $Z_{\text{in}}$  the input impedance to the resonator.  $C_c$  denotes a coupling capacitance, which couples the resonator to the input/output line. a) Lumped-element model of the resonator with capacitance  $C$ , inductance  $L$  and resistance  $R$ . b) Distributed element model, where  $C'\Delta x$  describes an elementary capacitance of the transmission line with a length  $\Delta x$  and so on. c) Input-output formalism for a double sided cavity modeled by partially transparent mirrors, where one side of the cavity acts as input/output port of a  $\lambda/4$  resonator and the other one as loss port. Input modes  $a_{\text{in}}$  and output modes  $a_{\text{out}}$  couple to the cavity modes  $a$  via a coupling  $\kappa_1$ . The loss port is modeled by a coupling rate  $\kappa_2$  to a loss mode  $b_{\text{out}}$ . Here the modes  $a_{\text{in}}$ ,  $a_{\text{out}}$  and  $b_{\text{out}}$  are treated as quantum mechanical modes.

Both quality factors can be combined into a loaded quality factor [55]

$$\frac{1}{Q} = \frac{1}{Q_{\text{int}}} + \frac{1}{Q_{\text{ext}}}, \quad (2.86)$$

which compares the stored energy in the resonator to the energy lost per cycle

$$Q = \omega_0 \frac{\text{average energy stored}}{\text{energy loss per second}}. \quad (2.87)$$

The full width at half maximum  $\Delta\omega_{\text{FWHM}}$  of the resonance peak relates to the loaded quality factor

$$\Delta\omega_{\text{FWHM}} = \frac{\omega_0}{Q}. \quad (2.88)$$

## 2.2.4 Coplanar waveguide resonator grounded by a dc-SQUID

Until now, we assume that the inner electrode of the resonator is connected directly to the ground plane. In the following, we will present the influence of a dc-SQUID on the resonator. As depicted in Fig. 2.9 the dc-SQUID effectively grounds the transmission line with an additional non-linear inductance  $L_{c,\text{SQUID}}(\Phi_{\text{ext}})$ , originating from the dc-SQUID. The added inductance is flux-dependent and therefore the resonant frequency of the resonator is also flux-dependent. In a straightforward approach, one writes the total

inductance as a sum of both inductances

$$L_{\text{tot}} = L_{\text{res}} + L_{c,\text{SQUID}}(\Phi_{\text{ext}}), \quad (2.89)$$

where  $L_{\text{res}}$  is the inductance of the bare resonator without dc-SQUID. Hence, by inserting  $L_{\text{tot}}$  in Eq. (2.81), the flux-dependent resonant frequency reads

$$f_0(\Phi_{\text{ext}}) = \frac{f_{\text{res}}}{\sqrt{1 + \frac{L_{c,\text{SQUID}}(\Phi_{\text{ext}})}{L_{\text{res}}}}}, \quad (2.90)$$

where we introduced the resonant frequency of the bare resonator  $f_{\text{res}} = \frac{1}{4\sqrt{L_{\text{res}}C_{\text{res}}}}$  without a dc-SQUID.

This approach does not take into account that the resonator is of distributed-element nature and the dc-SQUID is grounding the resonator at the end. To find a better expression for  $f_0(\Phi_{\text{ext}})$ , we follow Ref. [60] and use the Lagrangian of the resonator to obtain a field equation for a  $\lambda/4$  resonator

$$\ddot{\phi}(x,t) - \nu^2 \phi''(x,t) = 0, \quad (2.91)$$

where  $\nu = 1/\sqrt{L'C'}$  is the phase velocity, depending on the inductance and capacitance per unit length and  $\phi(x,t)$  is the phase.

With the boundary condition at the input of the cavity

$$\phi'(0,t) = 0, \quad (2.92)$$

we obtain possible solutions of the form

$$\phi(x,t) = \phi_1 \sin(k\nu t) \cos(kx), \quad (2.93)$$

where  $k = 2\pi/\lambda$  is the wave vector, corresponding to a wavelength  $\lambda$ . The boundary condition at the dc-SQUID side reads

$$\phi(d,t) = \varphi_+(t). \quad (2.94)$$

Using the total Lagrangian  $\mathcal{L}_{\text{tot}} = \mathcal{L}_{\text{SQUID}} + \mathcal{L}_{\text{resonator}}$  and approximating the dc-SQUID Lagrangian (see Eq. (2.77)) for  $\varphi_+ \approx 0$  with  $\cos \varphi_+ \approx 1 - \varphi_+^2$  and using Eq. (2.57), we find the boundary condition to be

$$\frac{\Phi_0^2 C_s}{(2\pi)^2} \ddot{\phi}(d,t) + \frac{\Phi_0^2 d}{(2\pi)^2 L_{\text{res}}} \phi'(d,t) + 2E_{J0} |\cos \varphi_-| \phi(d,t) = 0, \quad (2.95)$$

where  $C_s$  is the capacitance of one Josephson junction,  $L_{\text{res}} = dL'$  is the total inductance of the resonator. Using Eq. (2.93), one arrives at the dispersion relation for the flux-dependent

resonant frequency  $f_0$

$$\left(\frac{\pi f_0}{2 f_{\text{res}}}\right) \tan\left(\frac{\pi f_0}{2 f_{\text{res}}}\right) = 2 \frac{(2\pi)^2}{\Phi_0^2} L_{\text{res}} E_{J0} |\cos \varphi_-| - \frac{C_s}{C_{\text{res}}} \left(\frac{\pi f_0}{2 f_{\text{res}}}\right)^2, \quad (2.96)$$

where we used the substitution  $kd = \frac{\pi f_0}{2 f_{\text{res}}}$ . For  $f_0 \rightarrow 0$ , which corresponds to zero Josephson energy or infinite Josephson inductance, one obtains an open transmission line. For  $f_0 \rightarrow f_{\text{res}}$ , corresponding to infinite Josephson energy or zero Josephson inductance, one obtains a standard  $\lambda/4$  resonator without any dc-SQUID. In general, an externally applied flux will change the Josephson energy as well as the Josephson inductance, and hence the resonant frequency of the whole resonator, according to Eq. (2.96).

## 2.2.5 Parametric amplification and generation of squeezed light

A parametric oscillator can, in general, be described as an oscillator where one or more of its parameters are periodically varied in time, hence the name parametric oscillator. From such a system various phenomena with different applications emerge. We put our focus on parametric amplification, which can be understood as a non-linear interaction between a strong pump tone  $f_{\text{pump}}$ , a signal mode  $f_{\text{signal}}$  and an idler mode  $f_{\text{idler}}$  (see Fig. 2.8). Depending on whether the amplifier exhibits three or four photon processes, one or two pump photons are split into a signal and an idler photon, obeying the relations  $f_{\text{pump}} = f_{\text{signal}} + f_{\text{idler}}$  or  $2f_{\text{pump}} = f_{\text{signal}} + f_{\text{idler}}$  [23]. If the generated signal and idler photons have different frequencies  $f_{\text{signal}} \neq f_{\text{idler}}$ , the process is usually referred to as non-degenerate or phase-insensitive parametric amplification.

For any phase-insensitive linear amplifier, linear meaning that the output and input are linearly related, it was shown by Caves [16] that the minimum number of added noise quanta  $A$  is related to the power gain  $G$  by

$$A \geq \frac{1}{2} \left| 1 - \frac{1}{G} \right|. \quad (2.97)$$

Thus, for large gains  $G$  the minimum added noise approaches 1/2 added noise photons. For a phase-sensitive amplifier, one obtains different numbers of noise quanta added for each quadrature

$$A_1 A_2 \geq \frac{1}{16} \left| 1 - \frac{1}{\sqrt{G_1 G_2}} \right|^2, \quad (2.98)$$

where  $A_1$  and  $A_2$  are the noise numbers added and  $G_1$  and  $G_2$  are the gains for the quadratures  $X_1$  and  $X_2$ , respectively. One can identify the two quadratures with the in-phase  $q$  and out-of-phase  $p$  quadratures as it was defined in Sec. 2.1.1. This means that for fixed  $G_1 G_2 = 1$ , no noise is added to the signal. One can amplify one signal quadrature ( $G_1 > 1$ ) but in turn needs to deamplify the other one ( $G_2 < 1$ ). In fact, this phenomenon corresponds to squeezing of a coherent input state incident to the phase-sensitive amplifier

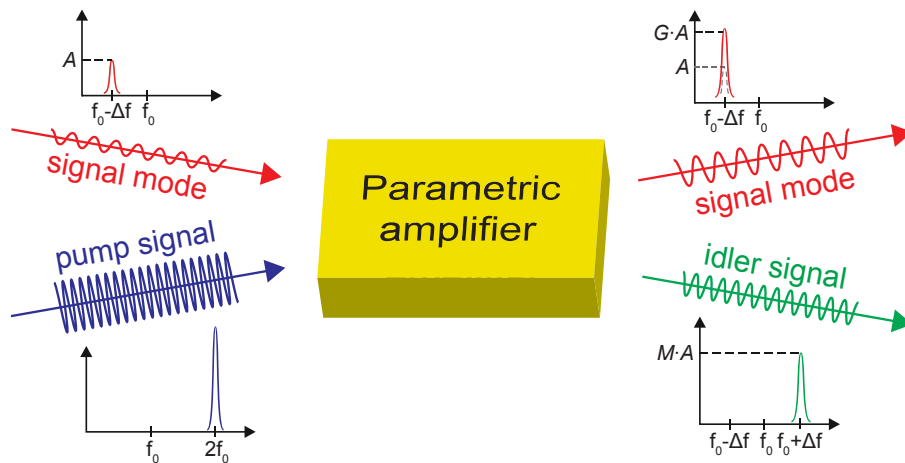


**Figure 2.8:** Scheme for parametric amplification with a three photon process. A signal mode with an amplitude of  $A$  at frequency  $f_{\text{signal}} = f_0 - \Delta f$  and a pump signal with frequency  $f_{\text{pump}} = 2f_0$  are incident to the JPA. For  $\Delta f \neq 0$ , the signal is amplified by  $G$  and an idler mode is generated at frequency  $f_{\text{idler}} = f_0 + \Delta f$ . For  $\Delta f = 0$ , the signal and idler mode have a degenerate frequency  $f_0$ .

as experimentally shown in Ref. [24], where a flux-driven JPA was used for this purpose. The variance of the deamplified quadrature is then reduced below the vacuum level while the variance of the amplified quadrature is increased, giving rise to a squeezed coherent state.

A parametric amplifier can be understood as such a phase-sensitive amplifier. In the degenerate operation mode, the signal and idler photons are frequency degenerate with  $f_{\text{signal}} = f_{\text{idler}}$ . From the Hamiltonian describing the interaction between the signal mode  $a$  and the pump tone one can derive that the quadratures related to the signal mode  $a$  can be squeezed [30, 44]. This is done by solving the Heisenberg equations of motion and identifying the result with the generator of a squeezed state given in Eq. (2.25).

In the non-degenerate mode with  $f_{\text{signal}} = f_0 - \Delta$  and  $f_{\text{idler}} = f_0 + \Delta$  one obtains a two-mode squeezed state, where there are correlations between the upper and lower sidebands around  $f_0$ , corresponding to the signal and idler mode, respectively [26].

Squeezed states are an important resource for continuous variables in quantum information processing. In the optical as well as in the microwave regime squeezed states can be used as a resource to create and distribute entanglement, enabling realizations of quantum teleportation, quantum key distribution and other protocols which require entanglement between bipartite or multipartite systems.

## 2.2.6 Flux-driven JPA

Now we focus on the flux-driven Josephson Parametric Amplifier shown in Fig. 2.9. The JPA is a parametric amplifier, where the  $\lambda/4$  coplanar waveguide resonator acts as an

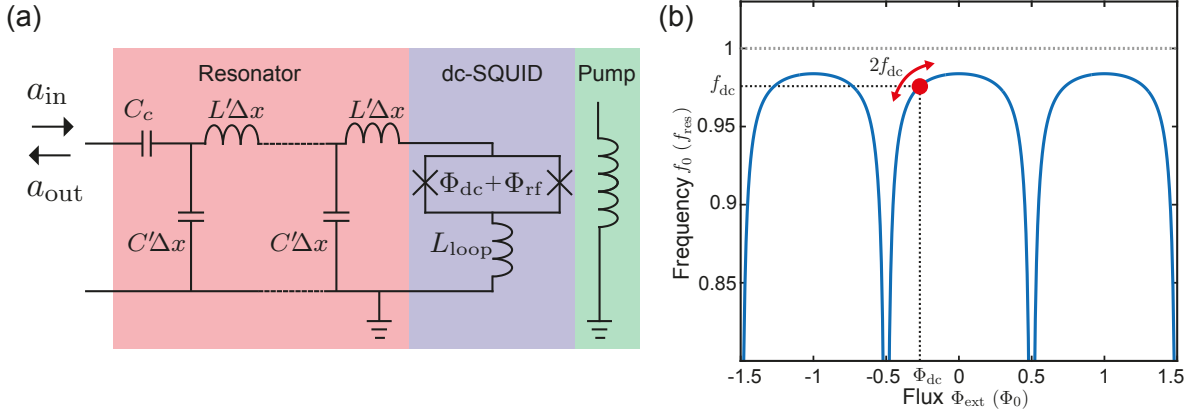


**Figure 2.9:** (a) Coplanar waveguide resonator (red) with inductance  $L'\Delta x$  and capacitance  $C'\Delta x$  per unit length grounded by a dc-SQUID (blue). The dc-SQUID loop has a loop inductance  $L_{\text{loop}}$ , which allows to inductively couple to a flux  $\Phi_{\text{dc}} + \Phi_{\text{rf}}$  generated by a coil and a pump line (green), respectively. Crosses indicate Josephson junctions. (b) Resonant frequency vs externally applied flux according to Eq. (2.96). The resonant frequency  $f_0$  is normalized to the bare resonator frequency without dc-SQUID  $f_{\text{res}}$ .  $\Phi_{\text{dc}}$  determines a working point at a frequency  $f_{\text{dc}}$ . A pump tone with  $2f_{\text{dc}}$  induces a time varying flux, resulting in an oscillating resonant frequency, which is required for parametric amplification.

oscillator and the dc-SQUID together with the pump line allow one to periodically vary the resonant frequency. By applying a dc magnetic field  $\Phi_{\text{dc}}$  through the dc-SQUID loop, one can tune the resonant frequency to a desired operating point  $\omega_{\text{dc}}$  (see Fig. 2.9 (b)). A time varying flux through the dc-SQUID loop  $\Phi_{\text{rf}}$  is induced via a pump line and allows for a modulation of the resonant frequency with the frequency of the pump tone  $2f_{\text{dc}}$ . The periodic modulation gives rise to parametric amplification [20], where one pump photon splits into a signal and an idler photon. Thus, the dc-SQUID allows to in-situ tune the resonant frequency of the JPA and is the central component of the parametric oscillator.

Starting with the equation of motion for an unperturbed harmonic oscillator

$$\frac{d^2 q}{dt^2} + \omega_0^2 q = 0, \quad (2.99)$$

and assuming a modulation of the resonant frequency  $\omega_0 \rightarrow \omega_0[1 + \delta \cos(\alpha\omega_0 t)]$ , one arrives at

$$\frac{d^2 q}{dt^2} + \omega_0^2 [1 + 2\delta \cos(\alpha\omega_0 t)] q = 0, \quad (2.100)$$

where we neglected the  $\delta^2$  term, since we assume a small modulation amplitude of the resonant frequency. After introducing the creation and annihilation operators for a harmonic oscillator, one arrives at the Hamiltonian of the parametrically-modulated harmonic oscillator

$$\mathcal{H} = \hbar\omega_0 \left[ a^\dagger a + \frac{1}{2} + 2\delta \cos(\alpha\omega_0 t) (a + a^\dagger)^2 \right]. \quad (2.101)$$

Yamamoto *et al.* [56] investigated the flux-driven JPA using the input-output formalism for both the non-degenerate and degenerate operation mode. In Ref. [61], the detailed theoretical description of Ref. [56] can be found. For the degenerate case, where the pump frequency is twice the signal frequency  $\omega_{\text{pump}} = 2\omega_{\text{signal}}$ , one arrives at a signal gain of

$$G_{\text{d}} = \frac{\left(\frac{\kappa_1^2 - \kappa_2^2}{4} + 4\delta^2\omega_0^2\right)^2 + 4\delta^2\kappa_1^2\omega_0^2 - 4\delta\kappa_1\omega_0\left(\frac{\kappa_1^2 - \kappa_2^2}{4} + 4\delta^2\omega_0^2\right)\sin(2\theta)}{\left(\frac{(\kappa_1 + \kappa_2)^2}{4} - 4\delta^2\omega_0^2\right)^2}, \quad (2.102)$$

where  $\theta$  is a constant phase between the signal and pump tones,  $\kappa_1$  and  $\kappa_2$  are the coupling rates defined in Eqs. (2.84) and (2.85),  $\delta$  is the pump amplitude and  $\omega_0$  is the resonant frequency. The  $\sin(2\theta)$  term shows, that the JPA is acting as phase sensitive amplifier. Furthermore, the minimum and maximum signal gains are

$$G_{\text{d}}^{\text{min}} = \left(\frac{2\delta\omega_0 - \frac{\kappa_1 - \kappa_2}{2}}{2\delta\omega_0 + \frac{\kappa_1 + \kappa_2}{2}}\right)^2 \quad \text{for } \theta = \frac{\pi}{4} + n\pi, \quad (2.103)$$

$$G_{\text{d}}^{\text{max}} = \left(\frac{2\delta\omega_0 + \frac{\kappa_1 - \kappa_2}{2}}{2\delta\omega_0 - \frac{\kappa_1 + \kappa_2}{2}}\right)^2 \quad \text{for } \theta = \frac{3\pi}{4} + n\pi, \quad (2.104)$$

where we use the condition  $(\kappa_1^2 - \kappa_2^2)/4 + 4\delta^2\omega_0^2 > 0$  and thereby assuming higher internal than external quality factors.

We also note, that for  $\kappa_2 = \omega_0/Q_{\text{int}} = 0$  the product of the maximum and minimum gain is

$$G_{\text{d}}^{\text{min}} \cdot G_{\text{d}}^{\text{max}} = 1, \quad (2.105)$$

and therefore it is theoretically possible to amplify one quadrature with the flux-driven JPA without adding any noise photons to the overall signal if the JPA has no internal losses. In fact, several experiments have shown that JPAs operated in the phase sensitive mode exhibit noise temperatures below the standard quantum limit [23–25]. In combination with the generation of squeezed light, the JPA is a useful tool in the field of propagating quantum microwaves, either as resource for the generation of quantum states or as nearly noiseless amplifier.



# Chapter 3

## Experimental techniques

### 3.1 Cryogenic setup

In our studies, we focus on squeezed light generated by a JPA. The generated microwave signals have a frequency around 6 GHz, which corresponds to a characteristic temperature of 288 mK. To study the quantum properties of the generated microwave signals, one needs to strongly reduce the number of thermal excitations, which degrade the quantum signal. Therefore, temperatures well below 288 mK are required to reduce thermal contributions to a minimum. Furthermore, low temperatures are required for the superconducting circuits we use to generate quantum microwave signals. For that, a cryogen-free or dry  $^3\text{He}/^4\text{He}$ -dilution refrigerator is used.

#### 3.1.1 Cryostat

The cryostat was designed and constructed at the Walther-Meißner-Institute by A. Marx, K. Uhlig, S. Höss, T. Brenninger, and the workshop team. Details on the cryostat can be found in Refs. [62, 63]. As depicted in Fig. 3.1, the dilution refrigerator has six temperature stages, where the first two stages pre-cool the cryostat with a Cryomech PT410-RM pulse tube cryocooler (PTC) to 50 K and 3 K, respectively. To increase the cooling power up to 100 mW at around 1 K, an additional  $^4\text{He}$ -1K-loop is installed as third temperature stage. The  $^4\text{He}$  circulation reduces the heat load on the dilution circuit by acting as heat sink for output lines as well as the  $^3\text{He}/^4\text{He}$  gas flow. The dilution circuit consists of one continuous heat exchanger, two step heat exchangers, a mixing chamber and the still. The still constitutes the fourth temperature stage at around 600 mK and is also fixed to a large copper plate so input and output lines can be thermalized. After the continuous heat exchanger, the first step exchanger is fixed to the fifth stage at around 100 mK. Finally, the mixing chamber is bolted to a copper plate. In the present setup the cryostat reaches a base temperature of approximately 15 mK. The usable space at the lowest temperature stage has an approximate height of 60 cm and a diameter of 30 cm and, thus, allows for multiple experiments to fit simultaneously in the cryostat. Furthermore, the cryostat is equipped with a  $^4\text{He}$  pre-cool loop, which is thermally connected to all temperature stages.

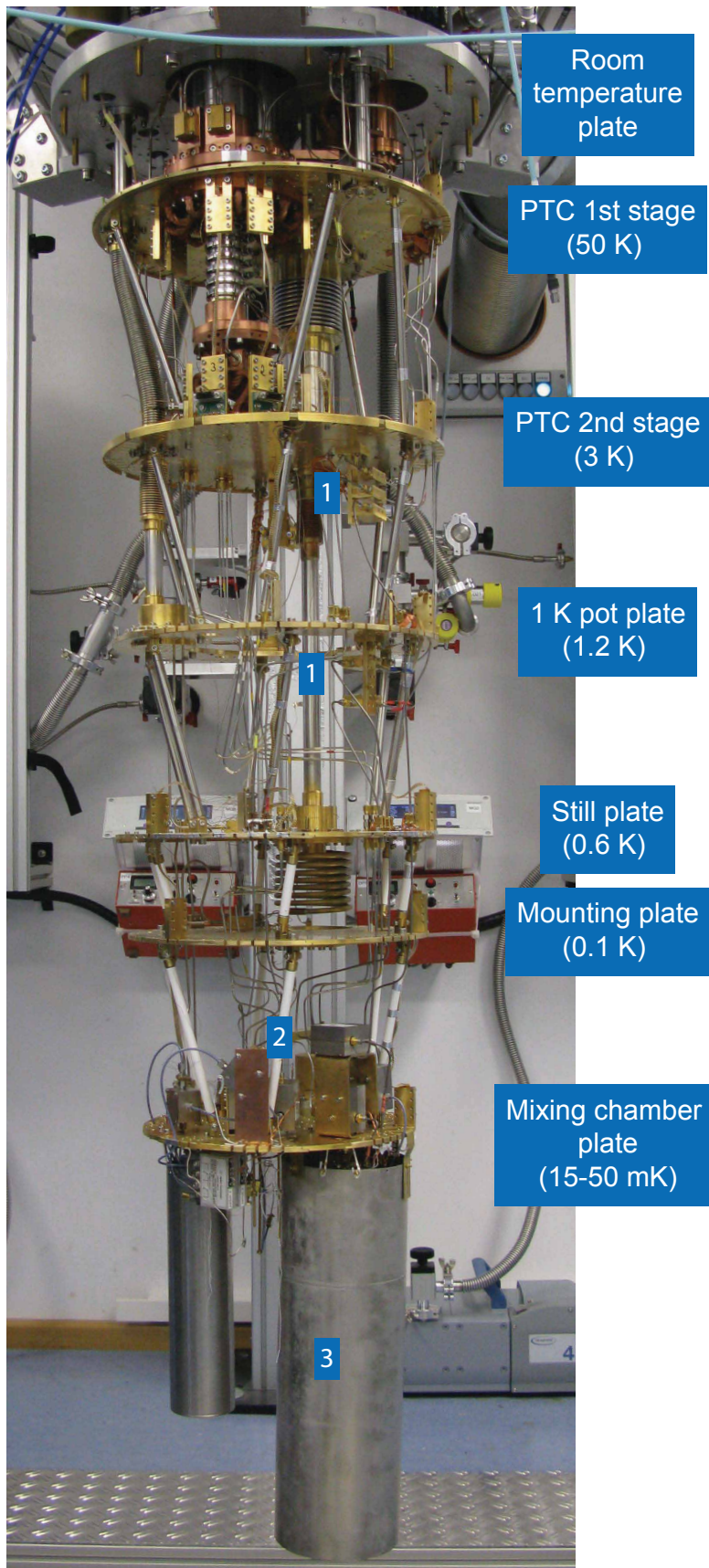


**Figure 3.1:** Photograph of the  $^3\text{He}/^4\text{He}$ -dilution refrigerator. 1: HEMT amplifiers, 2: Microwave circulators for isolation of output lines and 3: Cryoperm shield with the sample rod inside.

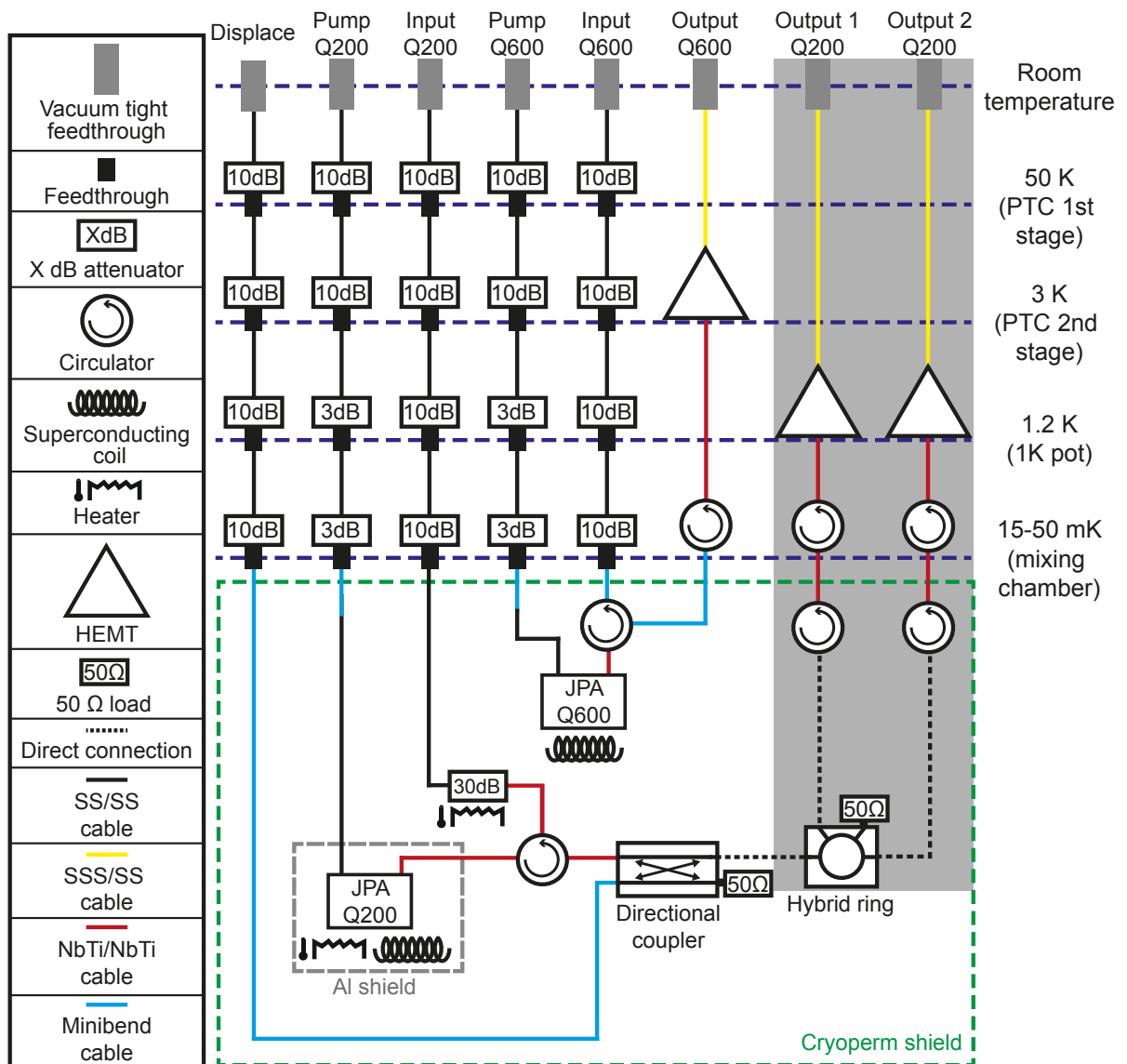


**Figure 3.2:** Schematic of the cryogenic setup with JPA Q200 (in a dual-path configuration) and JPA Q600 (in a single-path configuration). JPA Q200 is replaced by JPA Q200new for the measurements discussed in chapter 5. The grey region indicates the cryogenic part of the dual-path setup. Female-female adapters between cables are omitted. SS: Stainless steel, SSS: silver plated stainless steel. For cables: XX/YY denotes the inner conductor XX and outer conductor YY.

Since the temperature stages of the dilution circuit are thermally well isolated from each other by mounting tubes made from glass fiber reinforced epoxy, the precooling loop is required to cool these stages as well as the 1K stage to  $\sim 10$  K during the cool-down procedure.

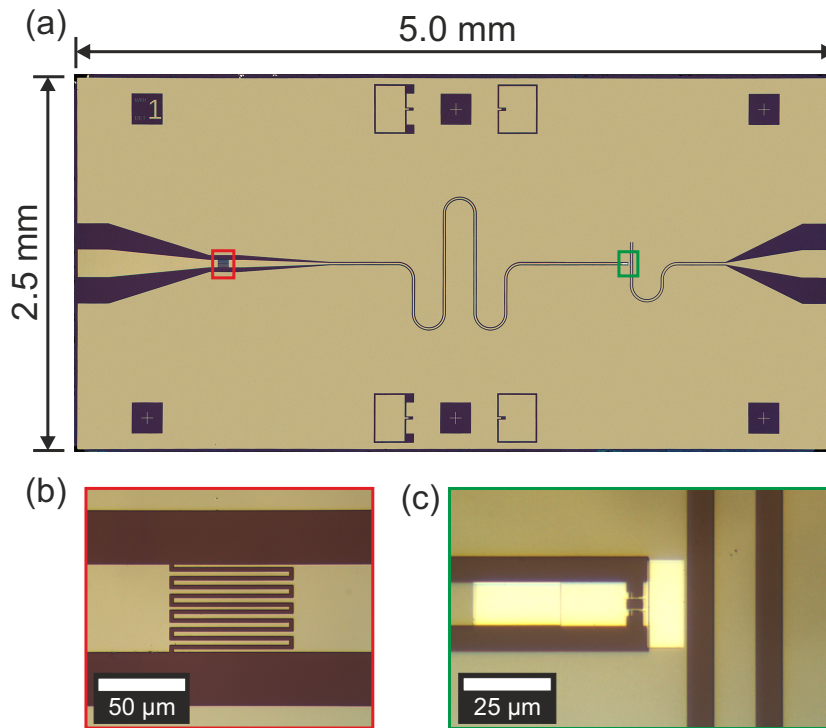


**Figure 3.3:** Optical micrographs of a JPA sample chip (JPA Q200). (a) JPA sample with a designed external quality factor of  $Q_{\text{ext}} = 200$ . Red and green rectangles mark the coupling capacitor and the dc-SQUID with the pump line, respectively. (b) Zoom-in to the coupling capacitor. (c) Zoom-in to the dc-SQUID with the adjacent pump line. The size of the dc-SQUID loop is  $4.2 \times 2.4 \mu\text{m}^2$ .

### 3.1.2 Sample preparation

The JPA samples were designed and fabricated at NEC Smart Energy Research Laboratories, Japan and RIKEN, Japan. In this thesis, three JPA samples are investigated. The samples JPA Q200 and JPA Q200new have a designed external quality factor  $Q_{\text{ext}} = 200$ . The third sample, JPA Q600, has a designed external quality factor  $Q_{\text{ext}} = 600$ . An optical micrograph of JPA Q200 is shown in Fig. 3.3. Thermally oxidized silicon with a thickness of  $300 \mu\text{m}$  is used as substrate. The silicon is visible as black/dark brown color in Fig. 3.3 (a)/(b,c). The resonator and the pump line are patterned into a previously sputtered Nb film with a thickness of 50 nm. A coplanar waveguide geometry (CPW) is used for the resonator and the pump line. The remaining Nb is visible as light brown color in the figure. The dc-SQUID is fabricated using a shadow evaporation technique [64] and consists of aluminum (white color in Fig. 3.3 (c)). The chip with a designed external quality factor  $Q_{\text{ext}} = 600$  has a smaller coupling capacitor and a higher designed critical current of the Josephson junctions in the dc-SQUID but otherwise an identical sample layout.

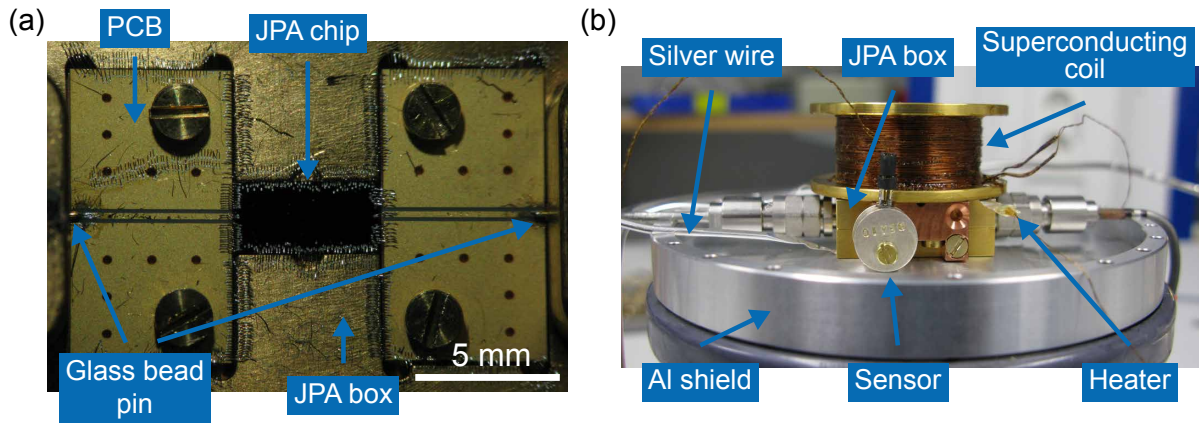


**Figure 3.4:** (a) Photograph of the JPA Q200 in the side-mounted sample box. The signal and pump lines are connected to microwave connectors via a PCB and a glass bead. (b) Photograph of the JPA sample box mounted in the aluminum shield (shown without cover). The sample box is thermalized with two silver wires connected to a silver rod. A temperature sensor and a heater are installed inside the aluminum shield. A magnetic field can be generated by a coil made of NbTi wire, mounted on top of the JPA sample box.

As seen in Fig. 3.4 (a), the JPA chips are glued to a sample box with GE-varnish to ensure mechanical fixation and thermal coupling to the box. Electrical connection of the center conductors on the chip to the printed circuit board (PCB) is realized by aluminum wires, which are placed with an ultrasonic bonding machine. The PCBs also have a CPW geometry. Furthermore, the ground planes of the chip and the PCBs are grounded to the sample box by aluminum bond wires. At one side of the PCBs, the center pin of a glass bead (V-110, Anritsu) is soldered to the center conductor. The PCBs improve the stability and reproducibility of the high frequency connection between a microwave connector and the JPA chip. The other side of the glass bead is connected to the center pin of a V-Male connector (V102M-R, Anritsu), where a SMA connector (2.4 mm, Southwest) is connected. We note that for JPA Q200 and JPA Q200new, a side-mounted sample box is used, whereas for JPA Q600, a top-mounted one is used. For further details on the influence of bonding and the connectors, we refer to Ref. [61].

The side-mounted sample box is installed inside an aluminum shield to provide screening from stray magnetic fields as shown in Fig. 3.4 (b). Inside the shield, a superconducting coil is installed which allows to control the magnetic flux through the dc-SQUID loop. Furthermore, a temperature sensor and a heater are installed to stabilize the temperature of the JPA during experiments. The sample box is thermalized by silver wires, which are connected to the sample rod.

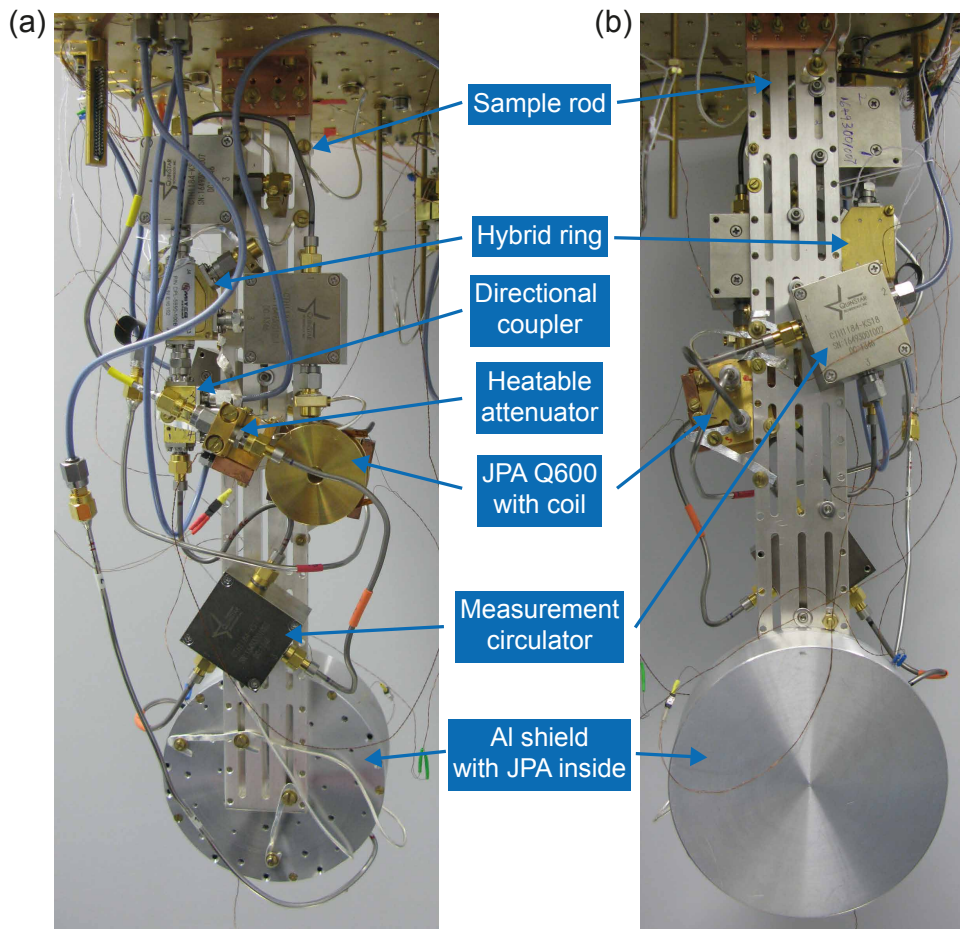


**Figure 3.5:** (a) Front and (b) rear views of the sample rod with experimental components. The rod is made out of silver and is attached to the mixing chamber plate.

### 3.1.3 Sample stage

As shown in Fig. 3.2, most of the microwave components and the JPA samples are located inside a cryoperm shield mounted to a silver rod. Only three additional circulators are placed on top of the mixing chamber plate and provide isolation from signals coming down the outputs lines (see Fig. 3.1). A photograph of the sample rod made out of silver is shown in Fig. 3.5 from the (a) front and (b) rear view. The sample rod is fixed to the mixing chamber plate by two copper pieces and additionally thermalized with multiple silver wires. A 'measurement circulator' separates the incoming and outgoing signals to and from the JPA, respectively. One is placed in front of each JPA.

For the Q200 samples, a heatable 30 dB attenuator is placed in the input line to the measurement circulator and is used for the calibration of the dual-path setup (see Sec. 3.2.3). The output of the measurement circulator is connected to a directional coupler (CPL-4000-8000-20-C) from Miteq with a coupling of -20 dB and an insertion loss of at least -0.2 dB. The directional coupler applies a displacement operation to an incident state

if a coherent signal is applied to the coupled port. The transmitted port is connected to a customized hybrid ring (CPL-5850-100B) from Miteq [65], which acts as a microwave beam splitter. The second input to the hybrid ring is terminated with a  $50\ \Omega$  load, providing a vacuum state incident to the input. The two outputs of the hybrid ring are directly connected to two circulators on the sample rod and from there to additional circulators on top of the mixing chamber plate as seen in Fig. 3.2 and Fig. 3.5.

For JPA Q600, no dual-path setup is used and therefore the output of the measurement circulator is connected to the output line via an additional circulator. Also, no 30 dB attenuator is installed in the input line.

Each component is either thermalized by fixing it tightly to the sample rod or by silver wires. The  $50\ \Omega$  loads, the 30 dB attenuator and bigger components, such as the JPA sample boxes with a coil and the aluminum shield, are additionally thermalized by silver wires. The silver wires are bent into the desired shape and thermally annealed at  $900^\circ$  for one hour to heal defects in its crystal structure. Subsequently they are installed without further bending them. This procedure increases the thermal conductivity of the silver wires and allows for better thermal coupling.

### 3.1.4 Input and output lines

#### Input lines

As shown in the sketch of our setup in Fig. 3.2, we use coaxial cables with inner and outer conductors made of stainless steel (SS) for the input lines. The dielectric layer consists of PTFE and the cables are manufactured by Coax Co., Ltd. With a specified loss of 9.44 dB/m at a frequency of 5 GHz, the losses are quite high. Therefore we use such cables mainly for input lines, where power dissipation is of minor importance. At four different temperature stages, the input lines are attenuated by 10 dB at the feedthroughs through the respective plates. This helps to thermalize the inner and outer conductors of the cables, so that thermal noise, coming from room temperature, is reduced by the attenuator value down to a local equilibrium noise level and the heat load on lower temperature stages is reduced. In short, attenuators at the different temperature stages are needed to obtain a desired power level but keep an acceptable signal-to-noise ratio and keep up to the cooling power of the cryostat at each temperature stage. The JPA pump lines are attenuated by 14 dB less, since higher pump power levels are required.

Each signal input line is connected to a measurement circulator from which a superconducting NbTi/NbTi cable is connected to the JPA signal input. Here we use a superconducting cable to minimize losses, since this cable acts simultaneously as output cable. For the Q200 samples, a heatable 30 dB attenuator is installed before the measurement circulator and is connected to this circulator by a superconducting NbTi/NbTi cable. This cable reduces the thermal coupling and cable losses between the attenuator and the measurement circulator, which is important during calibrations of the detection chains (see Sec. 3.2.3).

## Output lines

For detecting quantum states, low losses of the microwave components until the first amplification stage are crucial. Therefore, up to the high electron mobility transistor (HEMT) amplifier, the output lines of the dual-path configuration consist of superconducting NbTi/NbTi cables. After the HEMT amplifier stainless steel cables with a silver plated stainless steel inner conductor are used. The superconducting cables are ordered from Coax Co., Ltd. and come in a length of 1 m and an outer diameter of 2.19 mm. After cutting and bending them into the desired shape, SMA connectors from Radiall are crimped to the ends. For the stainless steel cables, the SMA connectors are soldered to the previously prepared cables.

To isolate the setup on the sample rod at millikelvin temperatures from thermal noise and downward propagating microwaves from higher temperature stages, the output lines are connected to circulators at the mixing chamber plate. The output superconducting cables are thermally coupled to each temperature stage by annealed silver wires or copper braids, which are pressed to the outer conductor of the cable.

The cryogenic HEMT amplifiers (LNF-LNC4 8A, Low Noise Factory) constitute the first amplification stage. With a specified amplification and noise temperature of approximately 38 dB and 2 K, respectively, they determine the noise temperature of the whole detection chain. The specified values were measured by the manufacturer at 10 K. To stabilize the HEMT gains over several days, the temperature of the power supply of the HEMT amplifiers is PID controlled within  $\pm 0.1^\circ\text{C}$ .

## 3.2 IQ Cross-correlation detector

The IQ cross-correlation detector consists of three parts. A cryogenic part, discussed in the previous section, a room temperature dual-path receiver, and the data acquisition and processing by the Acqiris card. In the following, the latter two parts are discussed in more detail.

### 3.2.1 Room temperature dual-path receiver

As seen in Fig. 3.6, the room temperature dual-path receiver is the extension of the cryogenic dual-path setup. An input signal to the hybrid ring, for example a displaced squeezed vacuum state, is split into two independent amplification paths. The second input port of the hybrid ring is terminated with a broadband precision  $50\ \Omega$  load, which is at a temperature of approximately 25 mK and, thus, serves as a vacuum reference state for the dual-path reconstruction<sup>1</sup>. Various isolators and circulators reduce spurious correlations between the two amplification chains. After the first amplification stage with

<sup>1</sup>The finite temperature causes the emission of a weak thermal state of the load which is taken into account during the state reconstruction.

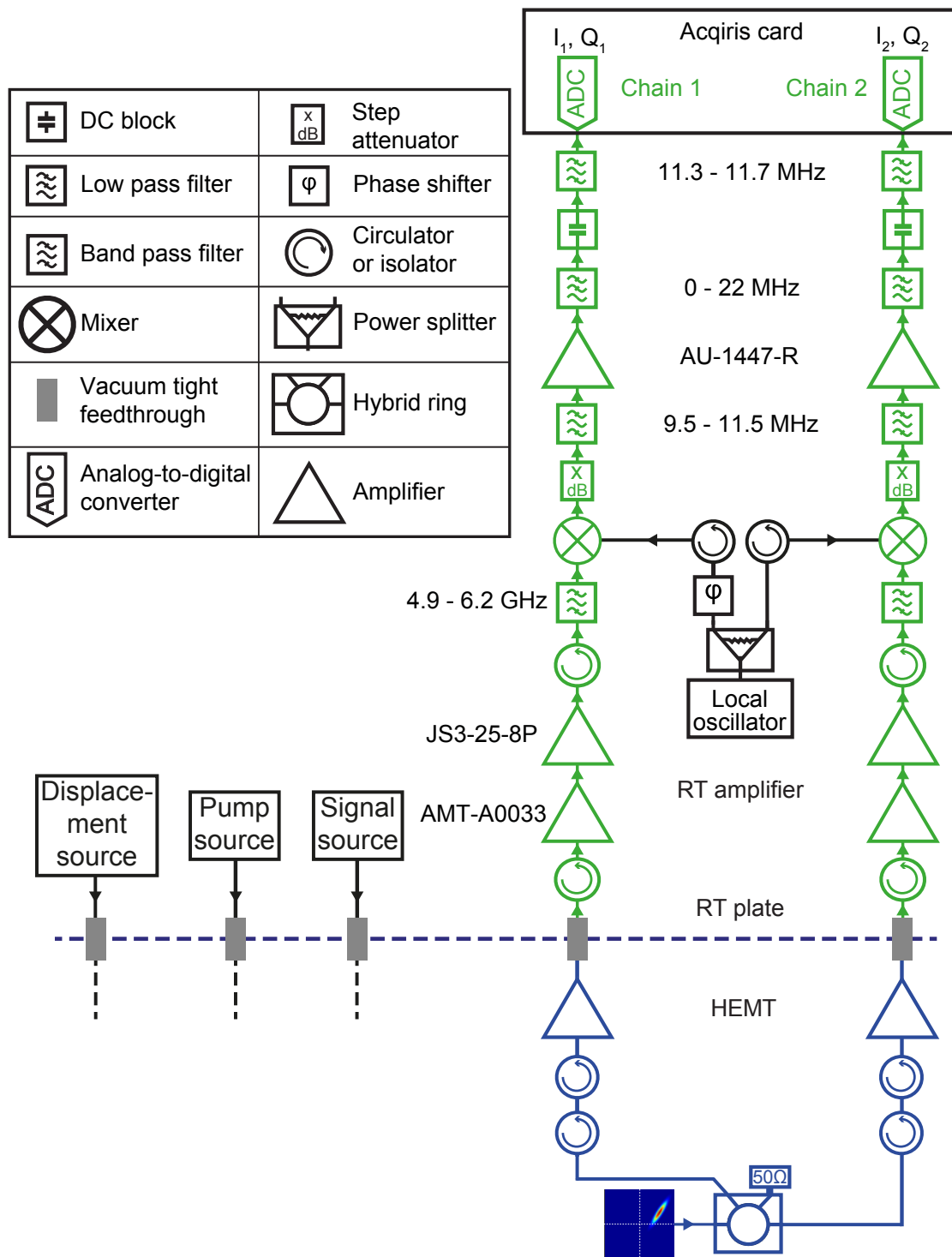


**Figure 3.6:** Setup of the dual-path receiver for JPA Q200new with analog filters at the Acqiris card input. Blue parts are the cryogenic part of the dual-path setup. Green parts constitute the room temperature dual-path receiver. Displacement, pump and signal source are connected to the corresponding inputs in Fig. 3.2. Numbers next to filters denote the passband range.

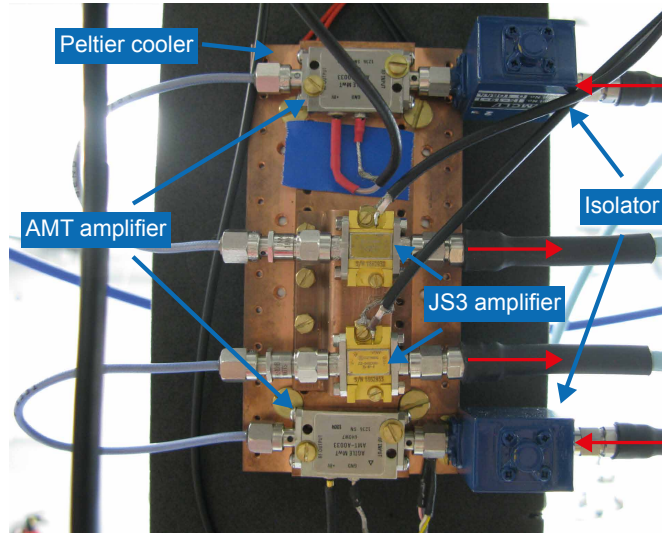


**Figure 3.7:** Peltier cooler with installed room temperature AMT and JS3 amplifiers. Red arrows indicate the signal direction.

the cryogenic HEMT amplifiers, the paths are further amplified at room temperature by AMT-A0033 (Agile MWT) and JS3-25-8P (Miteq) amplifiers, which are stabilized at a temperature of  $19.5 \pm 0.05$  °C by a Peltier cooler (see Fig. 3.7). A bandpass filter with a passband from 4.9 to 6.2 GHz provides a rough filtering around the desired RF frequency.

Now a mixer, biased by a strong local oscillator signal  $A_{\text{LO}} \cos(\omega_{\text{LO}}t + \phi_{\text{LO}})$ , down-converts the RF signal to an intermediate frequency (IF) around 11 MHz. The local oscillator signal for both mixers is generated by a single microwave source and a subsequent beam splitter. In one path of the local oscillator signal, a phase shifter is inserted to adjust the relative phase between the IF signals in both chains to  $180^\circ$ . An incident arbitrary RF signal  $A \cos(\omega t + \phi)$  to the mixer, produces an output  $A(t)$  of the form

$$A(t) = \tilde{A} \cos(\omega_{\text{IF}}t + \phi), \quad (3.1)$$

where  $\omega_{\text{IF}} = \omega - \omega_{\text{LO}}$  and  $\tilde{A}$  is the amplitude of the IF signal after the mixer. The sum frequency  $\omega_{\text{IF}} + \omega_{\text{LO}}$ , which is also generated, can be neglected due to bandpass filters after the mixer, which efficiently filter the high RF frequency. We note here, that also a sideband at the RF frequency  $\omega - 2\omega_{\text{IF}}$  is down-converted to a IF signal with the frequency  $-\omega_{\text{IF}}$ . This unwanted contribution to the IF signal cannot be filtered away digitally after the down-conversion in the current setup configuration. Rather, a very steep analog RF filter would be required to filter the sideband frequency  $\omega - 2\omega_{\text{IF}}$  before the mixer. This approach, however, would limit the receiver to a certain frequency  $\omega$ . This problem can potentially be circumvented by using image reject mixers which filter out a blue or a red sideband of an incident RF-signal, in respect to a LO, during down-conversion to the intermediate frequency. Also, if a digitizer with four input channels is available, IQ-mixers instead of single ended mixers can be used, where it is possible to filter the sideband

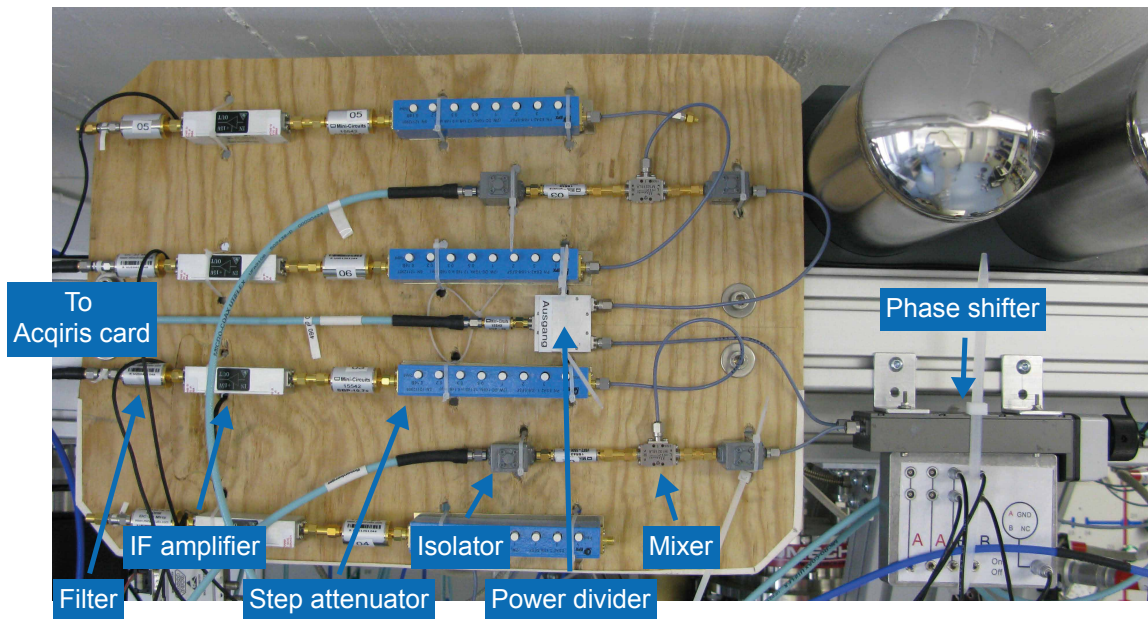


**Figure 3.8:** Photograph of the room temperature dual-path receiver. The top and bottom chains would be used for an FPGA-based setup, where IQ mixers are used instead of mixers.

frequency during digital down-conversion of the I and Q signals to dc for each chain [49].

After the mixers, step attenuators are inserted to adjust the amplitude of the IF signal to the detection range of the ADCs inside the Acqiris card and also to balance the signal amplitude in the chains relative to each other. Bandpass filters provide filtering of the high frequency output of the mixers and also reduce the incident power to the IF amplifiers to prevent compression effects. IF amplifiers (AU-1447-R, Miteq) further amplify the IF signals, where the noise bandwidth is reduced by subsequent low pass filters with a passband from 0 to 22 MHz. DC-blocks prevent dc-currents from the receiver to the ADCs. Finally, narrow band-pass filters with a passband from 11.3 to 11.7 MHz determine the measurement bandwidth and are installed directly at the Acqiris card input. ADCs then digitize the input signal with a sampling rate of 400 MHz, where calculations of the moments from the digitized data are performed on the computer, as described in the following in more detail. All microwave sources are synchronized by a 10 MHz reference signal from a rubidium clock.

### 3.2.2 Data acquisition and processing with Acqiris card

We use an Acqiris DC440 card with 12-bit resolution to digitize IF signals with a sampling rate of 400 MHz. Two ADC inputs with adjustable input voltage ranges from  $\pm 125$  mV to  $\pm 5$  V are available. Depending on the attenuation of the step attenuators and whether narrow analog filters at the input to the Acqiris card are used or not, different input voltage ranges are used to maximize the resolution of the ADCs. A sketch depicting the data processing is shown in Fig. 3.9. Each segment recorded by the Acqiris card

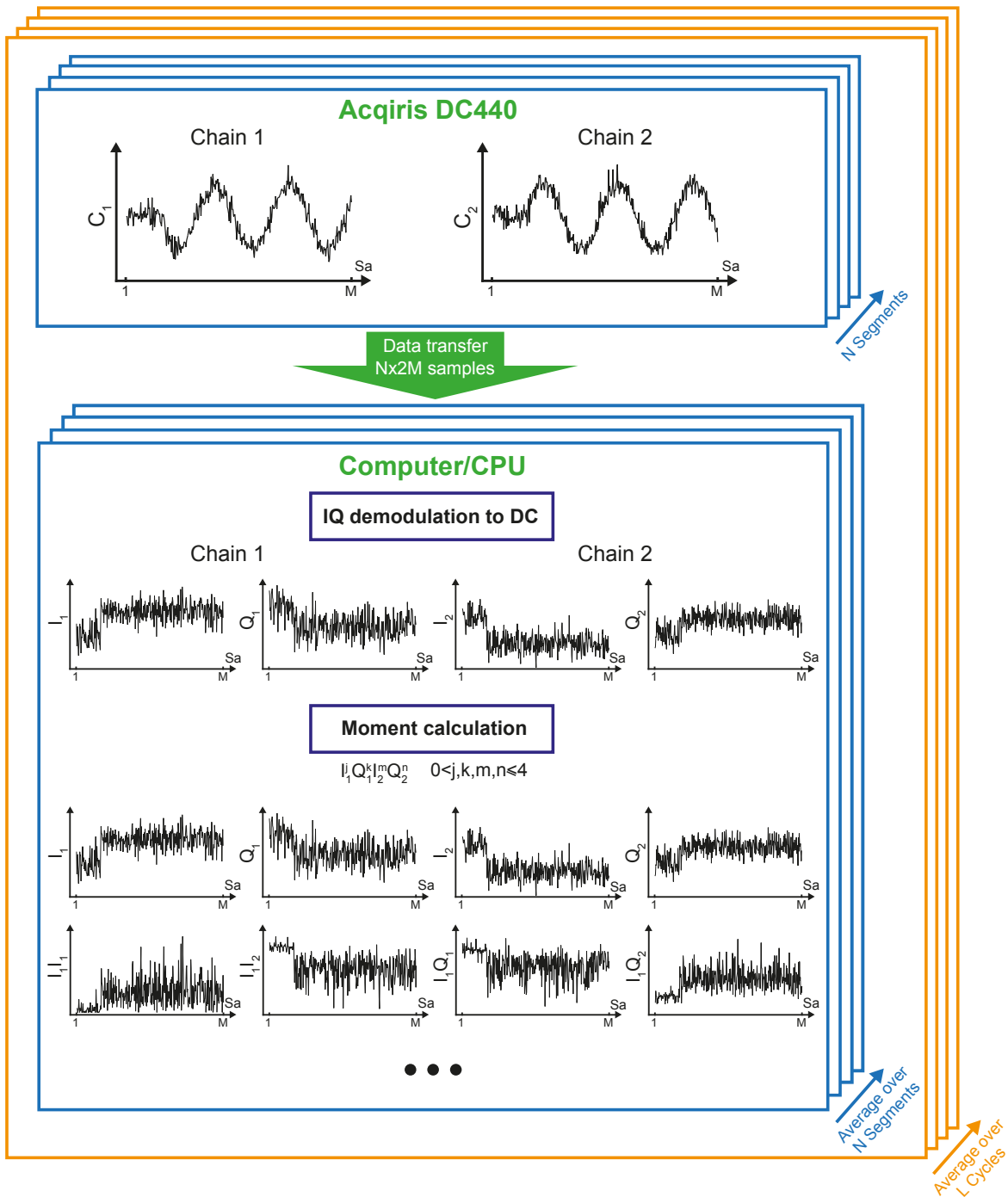


**Figure 3.9:** Sketch of the Acqiris card based data acquisition and processing. Each segment is triggered by a trigger pulse from a DTG. Figures show exemplary data recorded for a coherent input signal. The first part of the traces is without coherent input signal for comparison. "Sa" denotes the sample index. Averaging over segments and cycles is performed on a computer.

contains  $M$  sample points for each detection chain. Due to the limited internal memory of the Acqiris card,  $N$  segments are recorded and then sent to a computer for further data processing. The raw data is transferred to a computer via a PXI-8570 module (ADLINK Technology INC.) installed in the Acqiris card. In the computer a PXI-to-PCI card (ADLINK Technology INC.) is installed in one PCI slot on the mainboard. Each raw trace, containing  $M$  samples, is then digitally IQ demodulated to dc, so for each chain both quadratures are obtained. The quadratures  $I$  and  $Q$  are obtained by numerical integration over one period of the IF signal  $A(t) = \tilde{A} \cos(\omega_{\text{IF}}t + \phi)$ , following the formulas

$$I = \frac{\omega_{\text{IF}}}{2\pi} \int_{t-2\pi/\omega_{\text{IF}}}^t \cos(\omega_{\text{IF}}\tau) A(\tau) d\tau = \frac{\tilde{A}}{2} \cos(\phi), \quad (3.2)$$

$$Q = \frac{\omega_{\text{IF}}}{2\pi} \int_{t-2\pi/\omega_{\text{IF}}}^t \sin(\omega_{\text{IF}}\tau) A(\tau) d\tau = \frac{\tilde{A}}{2} \sin(\phi). \quad (3.3)$$

Since a whole period of data points needs to be available for the numerical integration, the quadrature components of the first 35 samples<sup>2</sup> of each segment cannot be calculated and are thus discarded in the further data analysis. If no analog band pass filter is used at the Acqiris card input, a digital FIR filter is used after the IQ demodulation, to filter the higher frequency components and reduce the detection bandwidth to a desired value. As next step, the quadrature moments  $\langle I_1^{j'} I_2^{k'} Q_1^{m'} Q_2^{n'} \rangle$  up to fourth order  $0 < j' + k' + m' + n' \leq 4$  for each sample point are calculated. Afterwards the whole process is repeated for  $L$  cycles. Each segment is triggered by a pulse generated by a Data Timing Generator DTG5334 from Tektronix which is also referenced to the rubidium 10 MHz reference source. Finally, the calculated moments for each sample trace of length  $M$  are averaged over segments and cycles, so every quadrature moment is averaged  $N \times L$  times. This procedure preserves the time information in one sample trace, so time-domain measurements are possible if needed. During the calculation of the signal moments  $\langle (\hat{a}_i^\dagger)^r \hat{a}_i^l \rangle$  from the quadrature moments  $\langle I_1^{j'} I_2^{k'} Q_1^{m'} Q_2^{n'} \rangle$  of each sample point  $i$ , following the dual-path reconstruction method [19], the sample trace is averaged to obtain the averaged signal moments  $\langle (\hat{a}^\dagger)^r \hat{a}^l \rangle$ .

### 3.2.3 Calibration

This section describes the calibration procedure of the IQ cross-correlation detector. Even though, the dual-path method does not rely on identical amplification paths, amplitude and phase balancing improve the measurement precision. Furthermore, the determination of the photon number conversion factor (PNCF) for each quadrature is an important issue.

#### Amplitude and phase balancing between the amplification chains

Before each PNCF calibration, the balancing between the amplification chains with respect to amplitude and phase is checked. For that, we first stabilize the heatable attenuator to

<sup>2</sup>The exact number depends on the intermediate frequency  $\omega_{\text{IF}}$  and the sampling rate of the ADCs.

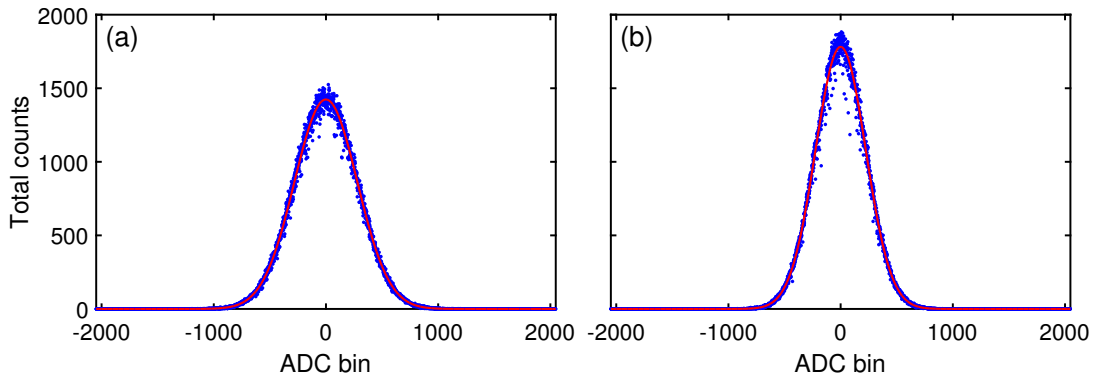


**Figure 3.10:** Unbalanced histograms of the total counts for each ADC bin for (a) channel 1 and (b) channel 2. The ADC bins correspond to the 12-bit resolution of the ADCs and thus span the x-axis with 4096 points. Red lines are Gaussian fits to the data.

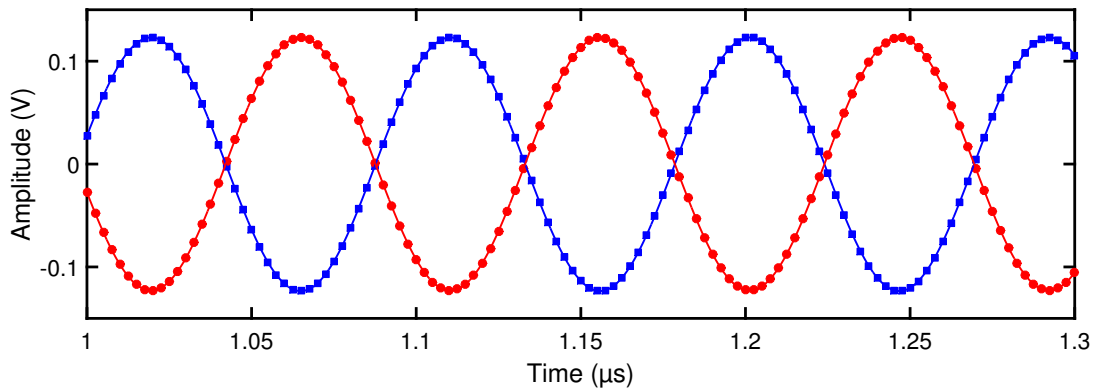


**Figure 3.11:** Balanced time traces for a strong coherent signal incident to the Acqiris card input for channel 1 (blue squares) and channel 2 (red dots). The lines are sinusoidal fits to the data.

600 mK and record the raw ADC readings for each chain. If we observe clipping effects, meaning that the ADCs are overloaded in the chosen input voltage range, the voltage range is adjusted or the attenuation of the step attenuators is increased. In Fig. 3.10 an exemplary unbalanced measurement for both channels is shown. By adjusting the step attenuators we balance both chains, so that both Gaussian distributions are identical and no clipping effects occur.

Next, we apply a strong coherent test signal to the JPA input line and record the signal with the Acqiris card. After fitting sinusoidal curves to the data (see Fig. 3.11), we can extract a balancing factor and also the relative phase between each input. In the measurement program for the Acqiris card, the balancing factor serves as a voltage pre-factor for one channel, so that both channel amplitudes are equal. These corrected amplitudes are also used for the moment calculation in later measurements. The relative phase between the two channels is manually adjusted by an analog phase shifter in one local oscillator signal path. The relative phase needs to be  $180^\circ$ , since the dual-path reconstruction assumes this phase difference between the two chains, due to the use of the

hybrid ring. The hybrid ring output signals have a relative phase of  $180^\circ$  in respect to each other, due to the device geometry. Fig. 3.11 shows a balanced measurement with respect to amplitude and relative phase of the two channels.

### Photon number conversion factor (PNCF) calibration

After balancing both chains the photon number conversion factors (PNCFs) for each quadrature component of the detected IF signals are determined. The detected quadrature moments  $\langle I_1^{j'} I_2^{k'} Q_1^{m'} Q_2^{n'} \rangle$  have units of volts to a power depending on the order of the moment. However, the desired signal moments  $\langle (\hat{a}^\dagger)^l \hat{a}^m \rangle$ , obtained from dual-path state reconstruction are given in units of photon number. Thus, a conversion factor between the measured voltages and the corresponding number of photons at the input to the hybrid ring is needed.

To this end, a calibrated photon source needs to be placed in front of the hybrid ring in order to provide a known number of photons. A qubit could be used for that purpose, but in the absence of a qubit, we use a heatable noise source and conduct a Planck spectroscopy experiment [66]. A heatable 30 dB attenuator is installed in the input line to the JPA. The attenuator acts as broadband black body emitter, whose temperature and thus its output power in a given bandwidth can be experimentally controlled. Due to the weak thermal coupling of the attenuator to the mixing chamber plate and the other microwave components, the temperature can be varied in the range  $T_{\text{att}} = 40 - 600$  mK, while other component retain a stable temperature. By using a superconducting NbTi/NbTi cable between the attenuator and the measurement circulator we further reduce the thermal coupling to the cryostat and also reduce losses. The total detected power  $P_{1,2}$  of each amplification chain is

$$\begin{aligned} P_{1,2}(T_{\text{att}}) &= \frac{\langle I_{1,2}^2 \rangle + \langle Q_{1,2}^2 \rangle}{R} \\ &= \frac{\kappa G_{1,2}}{R} \left[ \frac{1}{2} \coth \left( \frac{hf_0}{2k_B T_{\text{att}}} \right) + n_{1,2} \right], \end{aligned} \quad (3.4)$$

where  $R = 50 \Omega$ ,  $h$  is the Planck constant,  $k_B$  is the Boltzmann constant, and  $f_0$  the center frequency of the detection bandwidth. The hyperbolic cotangent term describes the emitted photons of the black body emitter at a frequency  $f_0$  and temperature  $T_{\text{att}}$ .  $n_{1,2}$  is the number of added noise photons and  $G_{1,2}$  the signal gain in each amplification chain. The product of  $\kappa = R \times 2 \times BW \times hf_0$  and  $G_{1,2}$  relates the measured quadrature moments  $\langle I_{1,2}^2 \rangle$  and  $\langle Q_{1,2}^2 \rangle$ , with units  $V^2$ , to the number of photons emitted by the attenuator. Here, we treat both quadratures identically. In the data analysis, however, we fit all four moments  $\langle I_1^2 \rangle, \langle Q_1^2 \rangle, \langle I_2^2 \rangle$  and  $\langle Q_2^2 \rangle$  individually and retrieve  $\kappa G$  and  $n$  for each moment.

During fitting, we take losses between the attenuator and the hybrid ring input with the beam splitter model into account and also consider a temperature gradient along the

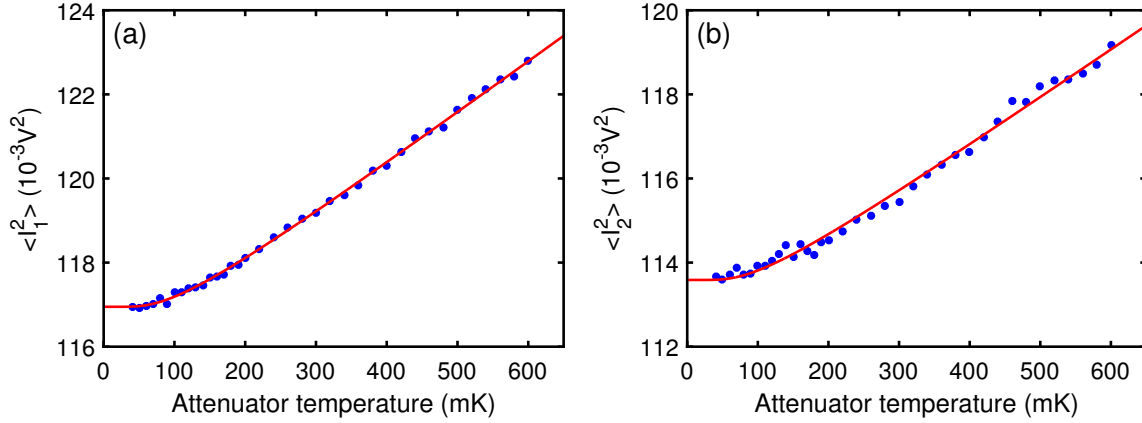


**Figure 3.12:** (a)  $\langle I_1^2 \rangle$  and (b)  $\langle I_2^2 \rangle$  plotted as a function of the attenuator temperature  $T_{\text{att}}$ . Blue dots are experimental data and the red line is a fit according to Eq. (3.4). The JPA temperature is stabilized to 50 mK. Each data point is averaged over  $5.6 \times 10^8$  samples.

cable between the heatable attenuator and the measurement circulator. The losses from the heatable attenuator to the measurement circulator are estimated to be 0.15 dB and the losses from the measurement circulator to the input of the hybrid ring, including the JPA insertion losses, are estimated to be 0.98 dB. Thus, we obtain a conversion factor between measured voltages and number of photons at the input to the hybrid ring.

In Fig. 3.12, the measured in-phase quadrature moments  $\langle I_1^2 \rangle$  and  $\langle I_2^2 \rangle$  are shown, corresponding to amplification path 1 and 2, respectively. Extracted fitting parameters are summarized in Tab. 3.1. We observe, that below approximately 60 mK, the contribution of the heatable attenuator to the measured quadrature moments is negligible and the detected signal mainly consists of noise added by the amplification paths. Furthermore,  $\langle I_2^2 \rangle$  corresponding to the cryostat output 2 in Fig. 3.2, yields slightly higher number of noise photons and deviates stronger from the theory curve (see Fig. 3.12 (b)), as compared to the other chain. After various tests, we conclude that the inferior performance of one chain originates from inside the cryostat, since swapping the amplification chains at several points outside the cryostat always yields a poorer performance for the cryostat output 2. Furthermore, we observe, that thermal anchoring of the superconducting output cables to the different temperature stages is important, since otherwise a thermal equilibrium of the cables is only reached after several days after cooling down the cryostat.

		PNCF $\kappa G$ ( $10^{-3} \cdot \text{V}^2$ )	Noise photons $n$
Chain 1	$I_1$ channel	$8.4 \pm 0.1$	$27.1 \pm 0.3$
	$Q_1$ channel	$8.5 \pm 0.1$	$26.9 \pm 0.3$
Chain 2	$I_2$ channel	$7.9 \pm 0.2$	$28.1 \pm 0.9$
	$Q_2$ channel	$7.9 \pm 0.2$	$28.1 \pm 0.8$

**Table 3.1:** PNCF and number of noise photons in the two detection chains calculated from fitting Eq. (3.4). Uncertainties are from 95% confidence bounds of fitting.

# Chapter 4

## JPA characterization

In this chapter, we characterize three different JPA samples, JPA Q200, JPA Q600 and JPA Q200new. First, the dependence of the resonant frequency on an external magnetic flux for the different JPA samples is studied. For JPA Q600 we observe a strong hysteretic behavior, originating from a large screening parameter  $\beta_L$ . We developed an approach to describe the flux dependence for an arbitrary  $\beta_L$  and apply it to our measurement results. Furthermore, we present both the extracted quality factors for the different samples and finally, the non-degenerate amplification properties of a JPA.

### 4.1 Flux dependence

As already discussed in Sec. 2.2.6, a dc-flux  $\Phi_{dc}$  applied to the dc-SQUID loop will tune the resonant frequency  $f_0$  of a flux-driven JPA. Additionally, a superposed oscillating magnetic field, with a frequency of approximately  $2f_0$  applied via a pump line, will cause parametric amplification. The amount of amplification depends on the amplitude of the modulation of  $f_0$  caused by the pump tone and thereby on the pump power as well as on the slope of the dependence of the JPA resonant frequency on the external flux. A careful choice of a flux working point is essential, since a flat flux dependence will not allow for reasonable gains and a too steep dependence makes the JPA susceptible to flux noise.

The flux dependence of the resonant frequency  $f_0$  is measured by sweeping the frequency of the JPA input signal and measuring the response with a Vector Network Analyzer (VNA) at different coil currents, corresponding to different flux values. Since a  $\lambda/4$  resonator geometry is used, one needs to measure the signal reflected from the JPA, as depicted in Fig. 4.1. We use a measurement circulator to separate the input signal  $a_{in}$  to the JPA from the back-reflected signal  $a_{out} = \Gamma a_{in}$ . Both the magnitude and the phase of the reflected signal, which correspond to  $|\Gamma|$  and  $\arctan \frac{\text{Im}\Gamma}{\text{Re}\Gamma}$ , respectively, are recorded. The VNA measures complex S-parameters by comparing the output and input signals going into and coming out of the device under test. In our measurements, we record the transmission coefficient  $S_{12}$  through the whole setup, including the JPA reflection coefficient as well as the input and output lines. Thus, one needs a calibration of the input and output lines to extract only the reflection coefficient  $\Gamma$  of the JPA alone.

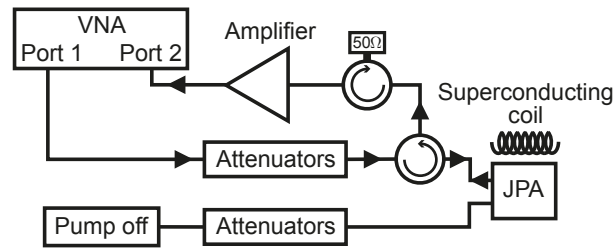


**Figure 4.1:** Setup for the measurement of the flux dependence with a Vector Network Analyzer (VNA). The reflected signal from the JPA is separated from the input signal by a measurement circulator. The pump is turned off during these measurements. The current through a superconducting coil determines the flux  $\Phi_{dc}$  through the dc-SQUID loop.

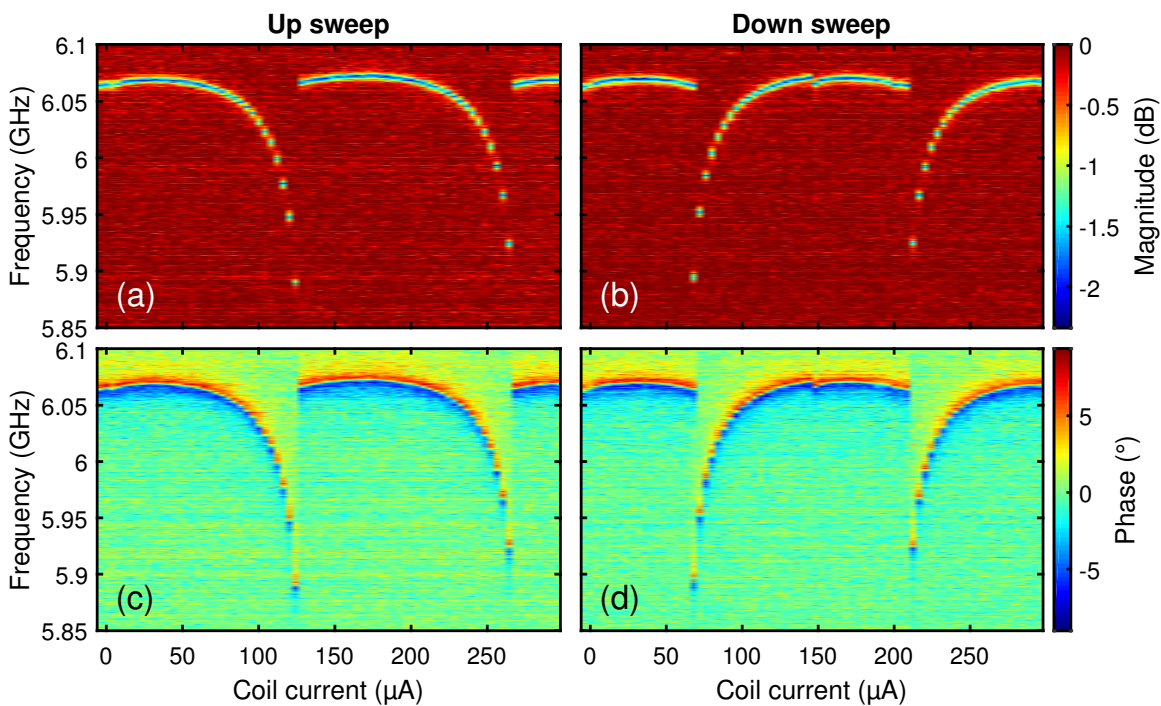


**Figure 4.2:** Flux dependence of JPA Q600 without a pump tone. For an increasing current through the coil (a) and (c) show the reflected magnitude and phase, respectively. (b) and (d) show the reflected magnitude and phase, respectively, for decreasing coil current.

In the presented data this is achieved by looking for coil currents, where the resonant frequency of the JPA is outside of the measured frequency window and, thus, no magnitude or phase response of the JPA are visible in the reference measurements. The recorded magnitude and phase of the VNA at these coil currents are then averaged and subtracted from the actual measurement data. For the phase, one additionally needs to perform a linear fit over the measured frequency range and subtract this fit from the measured phase data, since the VNA records the unwrapped phase resulting in a linear phase increase with frequency.

Fig. 4.2 shows the recorded flux dependence for the strongly hysteretic JPA Q600 with

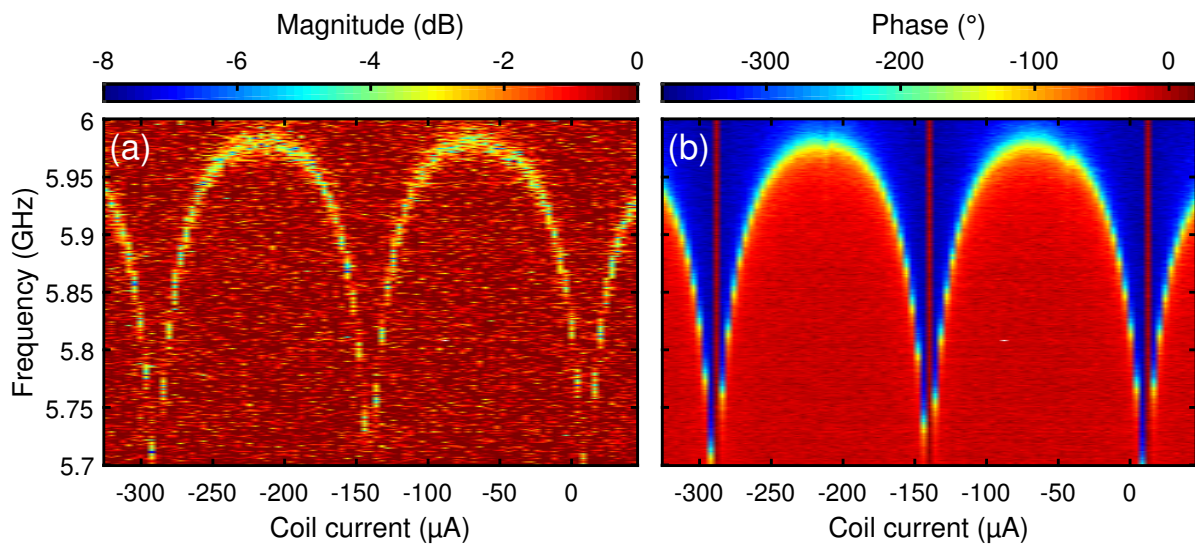


**Figure 4.3:** Flux dependence of JPA Q200 without a pump tone. (a) Magnitude and (b) phase for increasing coil current. No hysteretic behavior is observed in the measured frequency range.

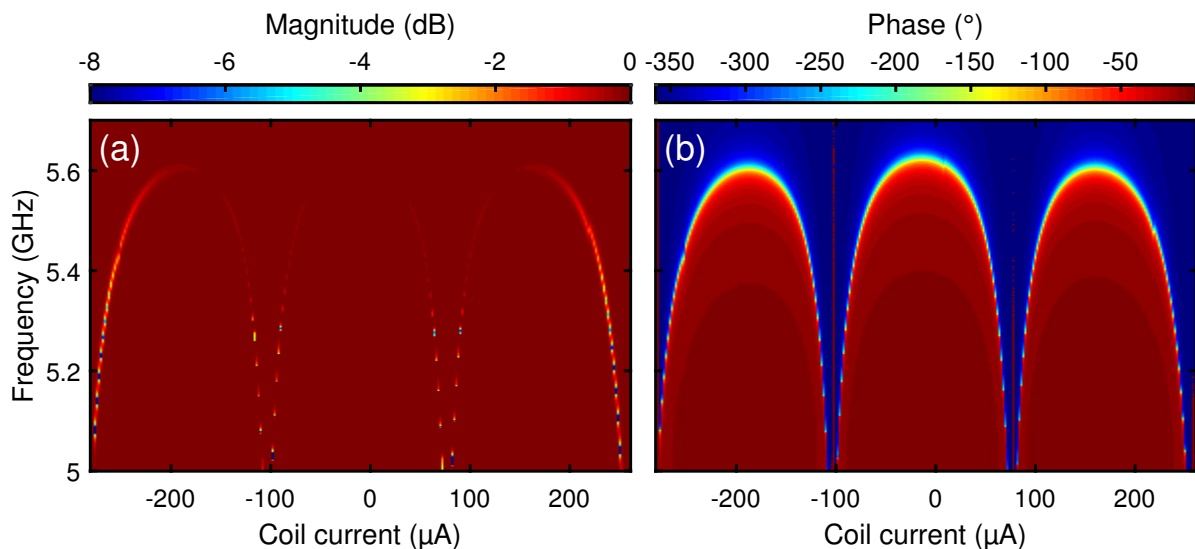


**Figure 4.4:** Flux dependence of JPA Q200new without a pump tone. (a) Magnitude and (b) phase for increasing coil current. No hysteretic behavior is observed in the measured frequency range. The central period shows a very weak magnitude response indicating high internal quality factors  $Q_{\text{int}}$ .

a designed external quality factor of 600. The resonant frequency  $f_0$  depends on the direction of the current sweep. The dependence is periodic in the externally applied magnetic field and at certain field values the resonant frequency  $f_0$  jumps from a low to a high value if one follows the direction of the magnetic field sweep.

We also investigated two other samples, JPA Q200 and JPA Q200new, which both have a designed external quality factor of 200. Fig. 4.3 and Fig. 4.4 show the flux dependencies for these samples. The resonant frequencies for both samples are single-valued and, thus,

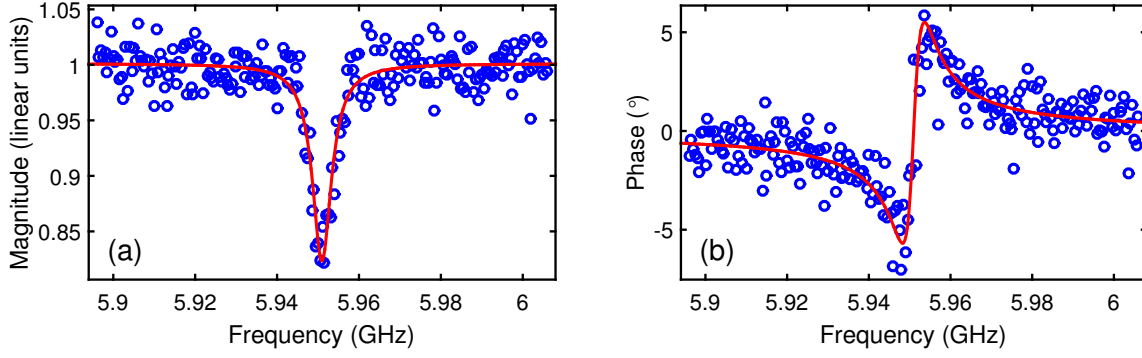


**Figure 4.5:** (a) and (b) show the reflection magnitude and phase of JPA Q600, respectively, at a coil current of  $72 \mu\text{A}$ . The measured data (blue) is fitted according to input-output formalism (red). The extracted quality factors for the shown fit are  $Q_{\text{ext}} = (11.3 \pm 0.8) \cdot 10^3$  and  $Q_{\text{int}} = (1.1 \pm 0.1) \cdot 10^3$ . Since the external quality factor is larger than the internal one, the JPA Q600 is undercoupled. This can easily be seen in the characteristic change in phase when crossing the resonant frequency. The phase does not make a complete  $360^\circ$  phase shift but rather exhibits a dip-peak structure.

no hysteretic behavior is observed. For JPA Q200 we observe a clear dip in the magnitude response of approximately 3 dB, which is independent of the coil current. In contrast, for JPA Q200new the magnitude response depends on the coil current. The central period shows a very weak dip in the reflected magnitude but a similar phase response over the whole coil current range. This behavior indicates an increased internal quality factor for low coil currents.

### 4.1.1 Quality factors

For resonators, or in our case JPAs, the internal and external quality factors are important quantities. The internal quality factor  $Q_{\text{int}}$  provides information about internal losses of the resonator. In general one wants to achieve  $Q_{\text{int}}$  as high as possible to minimize such losses and, thus, improve the lifetime of photons inside the resonator. The external quality factor  $Q_{\text{ext}}$  is mainly defined by the coupling capacitor  $C_c$  (see Fig. 2.7), which couples the resonator to the input and output port. If  $Q_{\text{ext}}$  is large then the coupling is weak and the chance for photons to enter or to leave the resonator is small.

As discussed in Sec. 2.2.3, one can model the  $\lambda/4$  resonator with the input-output formalism, leading to a reflection coefficient

$$\Gamma = \frac{(\omega - \omega_0)^2 + i\kappa_2(\omega - \omega_0) + \frac{\kappa_1^2 - \kappa_2^2}{4}}{(\omega - \omega_0 + i\frac{\kappa_1 + \kappa_2}{2})^2}, \quad (4.1)$$

where  $\kappa_1 = \frac{\omega_0}{Q_{\text{ext}}}$  and  $\kappa_2 = \frac{\omega_0}{Q_{\text{int}}}$  are the coupling rates, related to the external and the internal quality factors, respectively, and  $\omega_0$  is the resonant frequency of the JPA for a given external flux. By fitting the magnitude and the phase of the reflected JPA signal

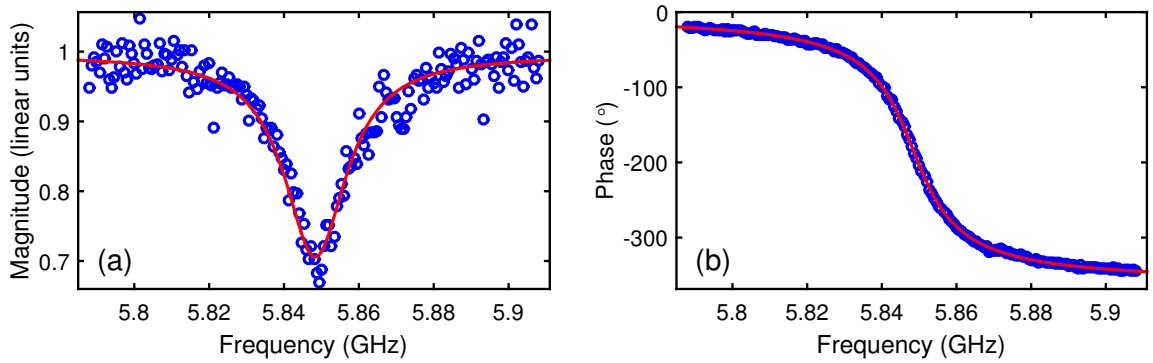


**Figure 4.6:** (a) and (b) show the reflection magnitude and phase of JPA Q200, respectively, at a resonant frequency of 5.85 GHz. The measured data (blue) is fitted according to input-output formalism (red). The extracted quality factors for the shown fit are  $Q_{\text{ext}} = 310 \pm 2$  and  $Q_{\text{int}} = (1.8 \pm 0.1) \cdot 10^3$ . Since the external quality factor is smaller than the internal one, the JPA Q200 is overcoupled, as seen in the  $360^\circ$  phase shift, when crossing the resonant frequency.

simultaneously for every coil current, one can determine the three fitting parameters  $\omega_0$ ,  $Q_{\text{ext}}$  and  $Q_{\text{int}}$ .

Fig. 4.5 shows an exemplary fit of JPA Q600 at a coil current of  $72 \mu\text{A}$ . The extracted quality factors from the fit are  $Q_{\text{ext}} = (11.3 \pm 0.8) \cdot 10^3$  and  $Q_{\text{int}} = (1.1 \pm 0.1) \cdot 10^3$  with uncertainties given by the 95% confidence bounds. The averaged quality factors for the coil current range shown in Fig. 4.2 are  $Q_{\text{ext}} = (12.0 \pm 0.7) \cdot 10^3$  and  $Q_{\text{int}} = (1.2 \pm 0.1) \cdot 10^3$ . Both  $Q_{\text{ext}}$  and  $Q_{\text{int}}$  show no obvious dependence of the coil current. The external quality factor strongly differs from the design parameter  $Q_{\text{ext}}^{\text{design}} = 600$  as well as the internal quality factor. Thus, JPA Q600 is in the undercoupled regime, resulting in the typical reflection phase response shown in Fig. 4.5 (b), where the phase exhibits a dip-peak structure when crossing the resonant frequency. Due to the low internal quality factor, JPA Q600 is not suitable for squeezing measurements.

For the sample JPA Q200 we observe an overcoupled behavior, where  $Q_{\text{int}}$  is larger than  $Q_{\text{ext}}$  as shown in Fig. 4.6. A characteristic phase shift of  $360^\circ$ , when crossing the resonant frequency is clearly visible. However, the average internal quality factor with a mean value of  $Q_{\text{int}} = (1.8 \pm 0.1) \cdot 10^3$  is not very large, indicating high internal losses of the JPA. Furthermore, a resonant frequency dependent external quality factor  $Q_{\text{ext}}$  in the range of 270–310, similar as discussed later for JPA Q200new, is observed. The external quality factor for this sample is therefore quite close to the design value  $Q_{\text{ext}}^{\text{design}} = 200$ .

For sample JPA Q200new, we again observe an overcoupled behavior, as shown in Fig. 4.7. The magnitude of the reflected signal is barely visible and the reflection phase undergoes a  $360^\circ$  phase shift when crossing the JPA resonant frequency. The extracted quality factors for the shown fit at a coil current of  $44 \mu\text{A}$  are  $Q_{\text{ext}} = 275 \pm 5$  and  $Q_{\text{int}} = (33.1 \pm 4.9) \cdot 10^3$ . This internal quality factor is surprisingly high and the scatter

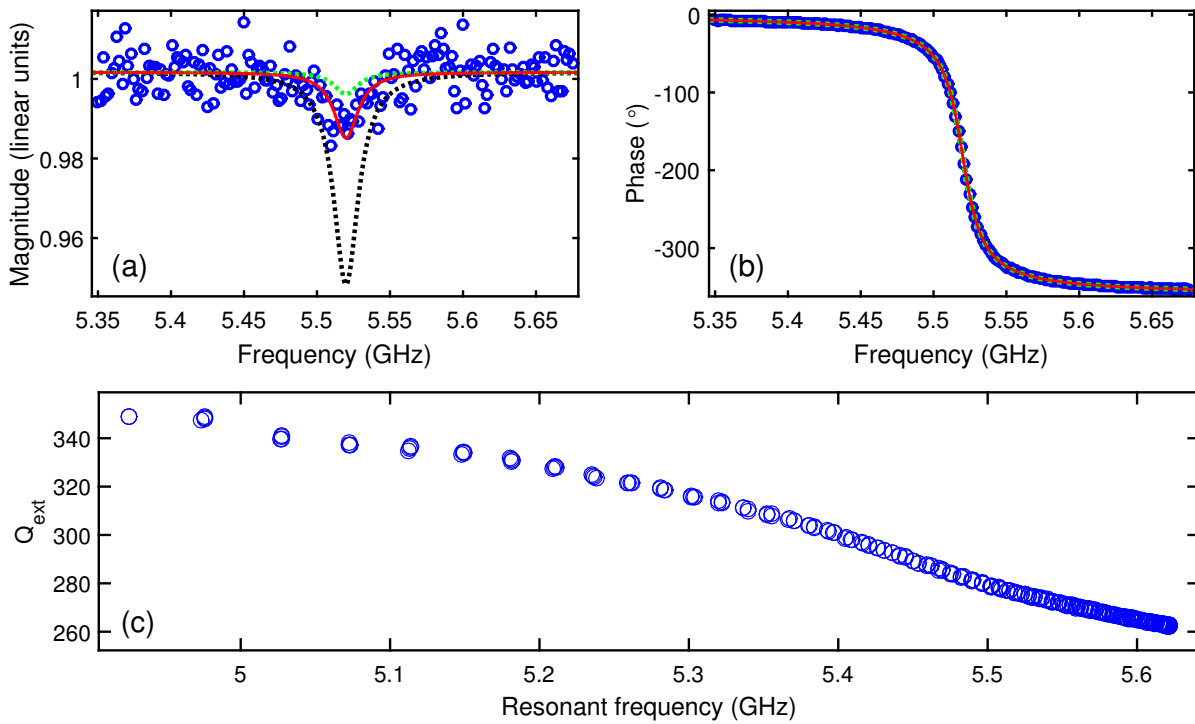


**Figure 4.7:** (a) and (b) show the reflection magnitude and phase of JPA Q200new, respectively, at a coil current of  $44 \mu\text{A}$ . The measured data (blue) is fitted according to input-output formalism (red). For comparison fits with fixed internal quality factors of  $Q_{\text{int}} = 10 \cdot 10^3$  (black) and  $Q_{\text{int}} = 100 \cdot 10^3$  (green) are shown as dashed lines. The extracted quality factors for the shown red fit are  $Q_{\text{ext}} = 275 \pm 5$  and  $Q_{\text{int}} = (33.1 \pm 4.9) \cdot 10^3$ . Since the external quality factor is much smaller than the internal one, the JPA Q200new is strongly overcoupled, as seen in the  $360^\circ$  phase shift, when crossing the resonant frequency. (c) shows the external quality factors  $Q_{\text{ext}}$  extracted from fitting as a function of the resonant frequency  $f_0$ . The fits are performed for coil currents between  $-150 \mu\text{A}$  and  $150 \mu\text{A}$ .

in the data is rather large. Therefore, fitted curves with fixed internal quality factors of  $Q_{\text{int}} = 10 \cdot 10^3$  and  $100 \cdot 10^3$  are shown for comparison. One can clearly see, that the unbounded fit describes the data best, whereas the fits with fixed internal quality factors lead to a too high or low dip in the reflected magnitude.

For this sample the designed external quality factor of  $Q_{\text{ext}}^{\text{design}} = 200$  is again close to the extracted ones (see Fig. 4.7 (c)). Furthermore, the fitted external quality factors decrease by a factor of approximately 80 when going from resonant frequencies around 5 GHz to the maximal values at 5.62 GHz. The external quality factors are equal for every period in the external flux dependence of the JPA resonant frequency.

The internal quality factors, on the other hand, exhibit a strong dependence on the coil current, which can already be seen in the reflection magnitude shown in Fig. 4.4 (a). The left and right period show a visible magnitude response, yielding internal quality factors in the range of  $5 \cdot 10^3 - 50 \cdot 10^3$ . For the central period, the magnitude response vanishes completely for low magnetic fields and, thus, the fitting procedure fails and no internal

quality factors can be extracted. Nevertheless, for lower frequencies in the central period, e.g. at a coil current of  $44 \mu\text{A}$ , as shown in Fig. 4.7 (a,b), one can still find reasonable quality factors.

We note that even when the reflection magnitude cannot be fitted, one can still extract the external quality factor from fitting the phase response, which is clearly visible for all coil currents. JPA Q200new exhibits high internal quality factors for regions where no clear response in the reflection magnitude is observed. For high internal quality factors the phase response is only weakly dependent on the exact value of the internal quality factor but depends mainly on the external one. To understand this, we look again at the fits with fixed quality factors and the unbounded fit shown in Fig. 4.7 (a,b). The magnitude response is clearly different, but the phase response is nearly identical for all three fits<sup>1</sup> and the extracted external quality factors only scatter by 1%. Thus, under the assumption of high internal quality factors in the regions, where no clear reflection magnitude is seen, one can still extract reasonable external quality factors from the phase response (see Fig. 4.7 (c)).

### 4.1.2 Simulation of the dc-SQUID potential

We now focus on the dependence of the resonant frequency on the external flux through a dc-SQUID loop. As shown in Sec. 2.2.4, the resonant frequency  $f_0$  depends on the Josephson energy, which in turn is depending on the external flux  $\Phi_{\text{ext}}$ . For an arbitrary  $\beta_L$ , a numerical approach is required to describe the flux dependence of  $f_0$ , since the induced circulating currents depend on the history of the applied flux and are, in general, multi-valued. Since, we are only interested in equilibrium states of the dc-SQUID, we start from the normalized potential of the dc-SQUID (see Sec. 2.2.2)

$$u(\varphi_+, \varphi_-) = \frac{U(\varphi_+, \varphi_-)}{E_{J0}} = 2 - 2 \cos \varphi_+ \cos \varphi_- - 2j\varphi_+ + \frac{2}{\pi\beta_L}(\varphi_- - \pi\varphi_{\text{ext}})^2, \quad (4.2)$$

where  $\varphi_+ = (\varphi_1 + \varphi_2)/2$  and  $\varphi_- = (\varphi_2 - \varphi_1)/2$ ,  $j = I_{\text{tot}}/(2I_c)$  and  $\varphi_{\text{ext}} = \Phi_{\text{ext}}/\Phi_0$ . The potential can be derived from the Lagrangian in Eq. (2.77) by using  $\mathcal{L} = K(\dot{\varphi}_+, \dot{\varphi}_-) - U(\varphi_+, \varphi_-)$ .

For  $\beta_L = 0$ , it follows from the last term in Eq. (4.2), that one needs to satisfy  $\varphi_- = \pi\varphi_{\text{ext}}$  in order to minimize the potential<sup>2</sup>, and thus an imaginary phase-particle is effectively moving inside the one-dimensional potential  $u(\varphi_+, \pi\varphi_{\text{ext}})$ . In this case, one recovers the result that the dc-SQUID can be seen as one Josephson junction with  $I_c \rightarrow 2I_c \left| \cos \left( \pi \frac{\Phi_{\text{ext}}}{\Phi_0} \right) \right|$ . An analog to this system would be two rigidly coupled pendula. Due to the strong coupling, only one degree of freedom remains. If one now loosens

<sup>1</sup>The phase response for all three fits are plotted in Fig. 4.7 (b), however the frequency dependence is nearly identical so the topmost phase response covers the other two.

<sup>2</sup>This is consistent with the fluxoid quantisation in Eq. (2.69), if one substitutes  $\Phi = \Phi_{\text{ext}} + L_{\text{loop}}I_{\text{circ}} = \Phi_{\text{ext}}$  for  $\beta_L = 0$ .

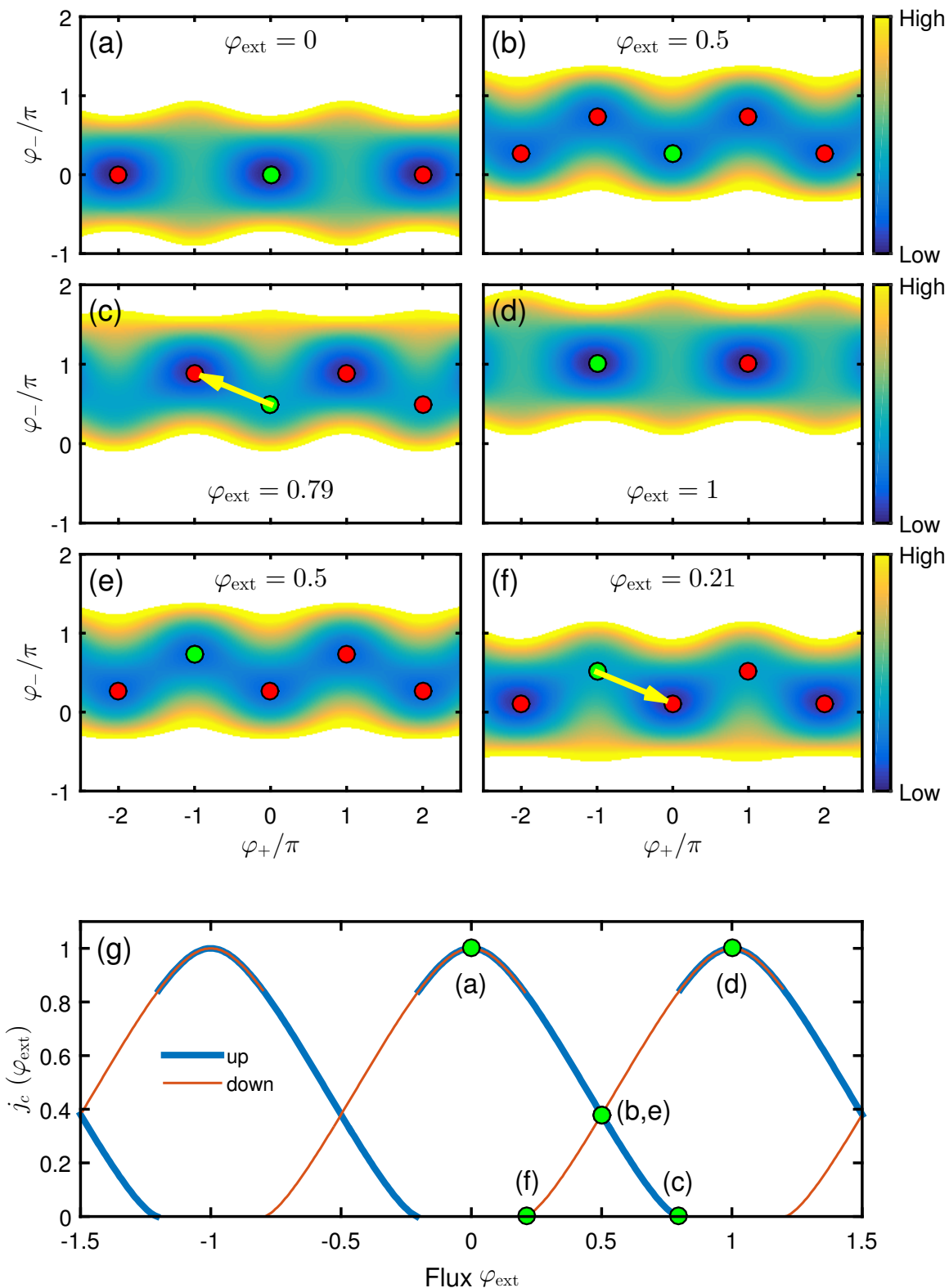


**Figure 4.8:** (a-f) show the dc-SQUID potential for different external flux values  $\varphi_{\text{ext}}$  and  $\beta_L = 0.592$ . Green dots denote the present position of the phase particle, whereas red dots are adjacent local minima. (a-d) and (e,f) correspond to increasing and decreasing  $\varphi_{\text{ext}}$ , respectively. Yellow arrows indicate a jump of the phase particle to an adjacent minimum, when the present minimum disappears. The obtained normalized dc-SQUID critical currents  $j_c(\varphi_{\text{ext}})$  when sweeping  $\varphi_{\text{ext}}$  up (blue line) and down (orange line) are shown in (g). Furthermore, the corresponding  $j_c$  values of the phase particle in (a-f) are denoted by green dots in (g).

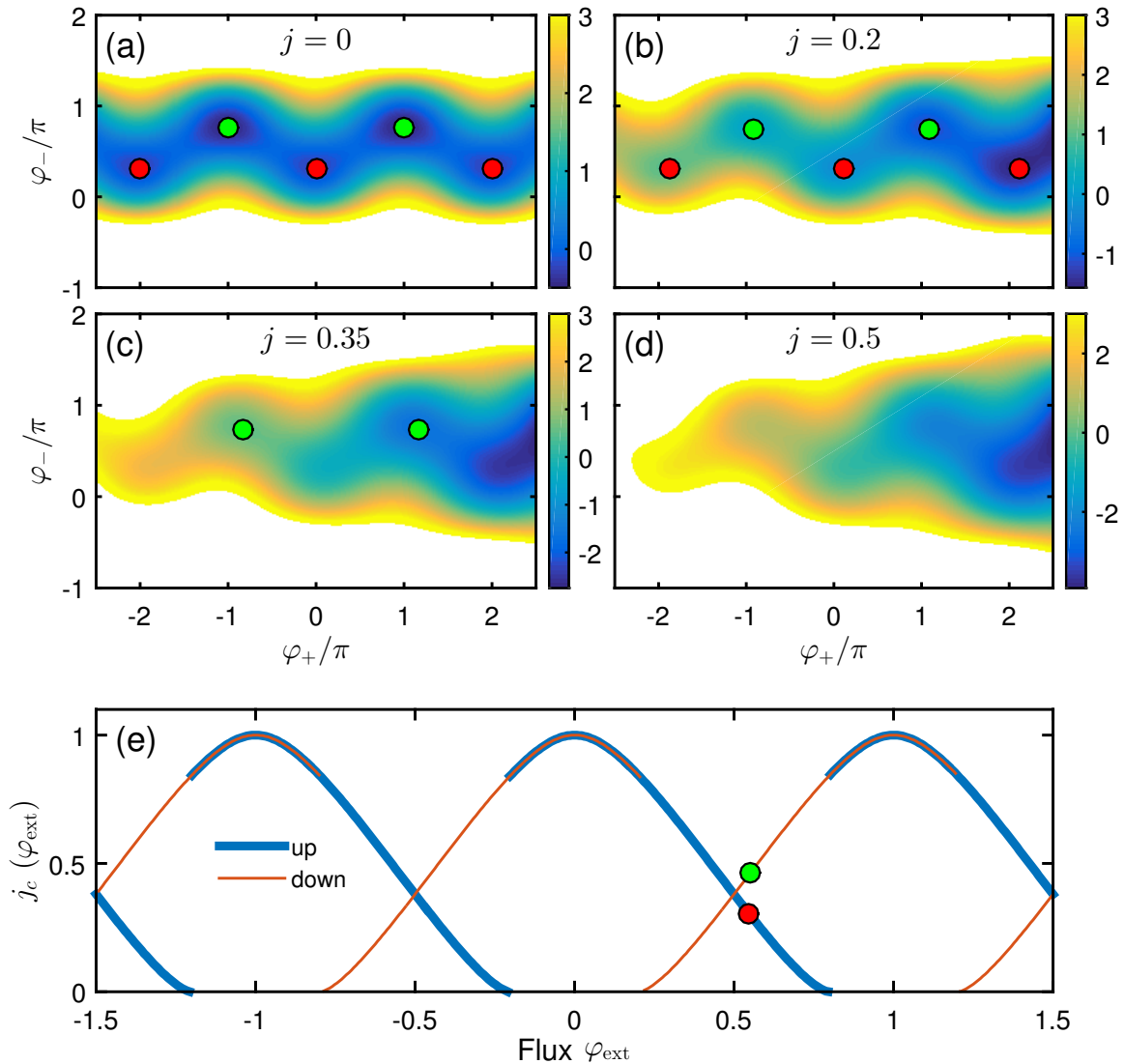
the coupling, by increasing  $\beta_L$ , one needs to consider both coordinates,  $\varphi_1$  and  $\varphi_2$ , or equivalently  $\varphi_+$  and  $\varphi_-$ , of the phase particle moving inside the potential of Eq. (4.2).

Fig. 4.8 illustrates the behavior of the phase particle (shown as a green dot) for increasing and decreasing the external flux for a screening parameter  $\beta_L = 0.592$  and no transport current through the dc-SQUID  $j = 0$ . If one looks at the  $\varphi_+$ -axis, the local minima (shown as red dots) are located at multiples of  $\pi$ , thus  $\varphi_+ = n\pi$  with  $n \in \mathbb{Z}$ . To be more precise, if the local minima have even  $\varphi_-/\pi$ , then the local minima are also located at even  $\varphi_+/\pi$ . If  $\varphi_-/\pi$  is odd, then the local minima are located at odd  $\varphi_+/\pi$ . Thus, it can be understood that the phase particle needs to jump at a certain flux value, if  $\varphi_{\text{ext}}$ , and therefore  $\varphi_-$ , is varied. The position of the jump depends on the magnitude of  $\beta_L$ . We assume, that the phase particle will reside in one minimum as long as the minimum exists and will then jump to an adjacent one. In general, the depths of the minima will be different, thus leading to a discontinuity of the dc-SQUID critical current  $2I_c \cdot j_c$ . Here we introduced the normalized critical current  $j_c$ , which denotes the normalized current  $j$  at which the local minimum of the phase particle vanishes. The discontinuity, in turn leads to a discontinuity of the dc-SQUID inductance  $L_{\text{SQUID}}(\Phi_{\text{ext}})$ , which can be experimentally observed in a jump of the resonant frequency  $f_0(\Phi_{\text{ext}})$  of the JPA.

Let us come back to Fig. 4.8 and explain the behavior in more detail. Fig. 4.8 (a-f) show a surface plot of the dc-SQUID potential for consecutive external flux values  $\varphi_{\text{ext}} = 0, 0.5, 0.79, 1, 0.5$  and  $0.21$ . In (a) the phase particle (green dot) starts at  $\varphi_+ = \varphi_- = 0$  for the external flux  $\varphi_{\text{ext}} = 0$ . When the external flux increases, the minimum of the green dot gets shallower while other minima at  $\varphi_+ = \pm\pi$  appear and get deeper. (b) For  $\varphi_{\text{ext}} = 0.5$ , all minima have the same depth and therefore the same normalized critical current  $j_c$ , nevertheless the phase particle will stay in its present minimum, since there is still a potential barrier separating the minima. (c) If the external flux is increased to a threshold flux  $\varphi_{\text{ext}}^{\text{jump}} = 0.79$ , the potential barrier vanishes and the phase particle will jump to one of the minima at  $\varphi_+ = \pm\pi$ . The threshold flux depends on the magnitude of  $\beta_L$ . For  $\beta_L = 0$ , it is exactly  $0.5^3$  and increases with increasing  $\beta_L$ . (d) While further increasing  $\varphi_{\text{ext}}$ , the phase particle resides in the new minimum until it would vanish again at  $\varphi_{\text{ext}} = \varphi_{\text{ext}}^{\text{jump}} + 1$  and so on. In general, one obtains jumps for increasing flux at  $\varphi_{\text{ext}} = \varphi_{\text{ext}}^{\text{jump}} + n$  with  $n \in \mathbb{Z}$ . (e) If the external flux is now decreased to  $\varphi_{\text{ext}} = 0.5$  again, the phase particle resides in the minimum at  $\varphi_+ = -\pi$  contrary to (b), where it was at  $\varphi_+ = 0$  for this particular  $\varphi_{\text{ext}}$ . (f) If the external flux is further decreased to  $\varphi_{\text{ext}} = 0.21$ , we again reach a jump point of the phase particle. For decreasing flux, these jump points are at  $\varphi_{\text{ext}} = n - \varphi_{\text{ext}}^{\text{jump}}$ . (g) depicts the normalized critical current  $j_c$  for increasing (blue) and decreasing (orange) external flux. Furthermore, the  $j_c$  values for (a-f) are also marked by green dots. One observes regions of  $j_c$  where the upward and downward sweep yield overlapping curves as well as regions where they do not overlap.

---

<sup>3</sup>For  $\beta_L = 0$  no hysteretic behavior is observed, since for  $\varphi_{\text{ext}} = 0.5$  all minima vanish and thus  $j_c = 0$ .



**Figure 4.9:** (a-d) show the dc-SQUID potential for different transport currents  $j$  at a fixed external flux  $\varphi_{\text{ext}} = 0.55$  and  $\beta_L = 0.592$ . Green and red dots denote local minima with uneven  $\varphi_+/\pi$  and even  $\varphi_-/\pi$ , respectively. For this particular external flux, the green local minima are deeper than the red ones. When the transport current  $j$  is increased above a certain threshold  $j_c^{\text{red}}$ , the red local minima disappear, while the green ones are still present. When reaching the second threshold  $j_c^{\text{green}}$ , also the green local minima disappear and the phase particle will inevitably slide down the two dimensional washboard potential. (e) shows the critical current  $j_c(\varphi_{\text{ext}})$ , which is obtained by looking at the local minima of the phase particle when increasing the transport current  $j$  for different  $\varphi_{\text{ext}}$ . When the local minimum disappears at a certain  $j$ , we denote this transport current as  $j_c$  for this particular  $\varphi_{\text{ext}}$ . When comparing with Fig. 4.8, one sees that  $j_c^{\text{red}}$  and  $j_c^{\text{green}}$  correspond to increasing and decreasing  $\varphi_{\text{ext}}$ , respectively.

The procedure to determine the normalized critical current  $j_c(\varphi_{\text{ext}})$  for every flux step is shown in Fig. 4.9. (a-d) show the dc-SQUID potential for different transport currents  $j = 0, 0.2, 0.35$  and  $0.5$ . For a given external flux  $\varphi_{\text{ext}}$ , the phase particle will be in a local minimum with even or odd  $\varphi_+/\pi$ , which depends on whether one increases or decreases  $\varphi_{\text{ext}}$ . The even (red) and odd (green) minima have different threshold transport currents  $j_c^{\text{red}}$  and  $j_c^{\text{green}}$ , respectively. These threshold currents are given by the transport current, when the respective local minima disappear. In Fig. 4.9 (g), one can see the obtained normalized critical current  $j_c(\varphi_{\text{ext}})$  with  $j_c^{\text{red}}$  and  $j_c^{\text{green}}$  marked in red and green, respectively. Thus it can be seen, that sweeping the flux up and down produces the blue and orange curve, respectively. For a more detailed description of the numerical approach on how to simulate the dc-SQUID potential and the normalized critical current  $j_c$ , we refer the reader to Appendix A.

### 4.1.3 Comparison with experimental data

The numerically calculated  $j_c(\Phi_{\text{ext}})$ , determines a certain dc-SQUID inductance (see Eq. (2.73))

$$L_{c,\text{SQUID}}(\Phi_{\text{ext}}) = \frac{\Phi_0}{4\pi I_c \cdot j_c(\Phi_{\text{ext}})}, \quad (4.3)$$

where  $I_c$  is the critical current of one Josephson junction. This equation can be used to calculate the resonant frequency of the JPA by rewriting Eq. (2.96) in the form

$$\left(\frac{\pi}{2} \frac{f_0}{f_{\text{res}}}\right) \tan\left(\frac{\pi}{2} \frac{f_0}{f_{\text{res}}}\right) = \frac{L_{\text{res}}}{L_{c,\text{SQUID}}(\Phi_{\text{ext}}) + L_{\text{loop}}} = \frac{2L_{\text{res}}I_c}{\frac{\Phi_0}{2\pi j_c(\Phi_{\text{ext}})} + \Phi_0\beta_L}, \quad (4.4)$$

taking into account a finite loop inductance  $L_{\text{loop}}$  of the dc-SQUID ring and using  $\beta_L = \frac{2I_c L_{\text{loop}}}{\Phi_0}$ . Here  $f_{\text{res}}$  and  $L_{\text{res}}$  are the bare resonant frequency and the inductance of the resonator without the dc-SQUID, respectively, and  $f_0$  is the actual, flux-dependent, resonant frequency of the JPA. Furthermore, the last term in Eq. (2.96) is neglected, since the capacitance of the bare resonator  $C_{\text{res}}$  is much larger than the capacitance of the Josephson junctions  $C_s$  and thus  $C_s/C_{\text{res}}$  vanishes. The experimental data is fitted with Eq. (4.4) by a least-mean-square algorithm and fitting parameters  $L_{\text{res}}I_c$ ,  $\beta_L$  and  $f_0$ . Furthermore, we obtain a conversion factor between the coil current and the flux  $\Phi_{\text{ext}}$  from fitting.

For JPA Q600 the dependence of the resonant frequency  $f_0$  on the external flux  $\Phi_{\text{ext}}$  is shown in Fig. 4.10. The resonant frequencies are extracted from fits with input-output formalism. Fig. 4.10 (a) and Fig. 4.10 (b) show the obtained resonant frequencies (blue circles) and corresponding fit (red line) for increasing and decreasing coil current, respectively. When combining both sweep directions (Fig. 4.10 (c)), one observes that the fit describes the overall dependency very well. To match the jump points from the lower to

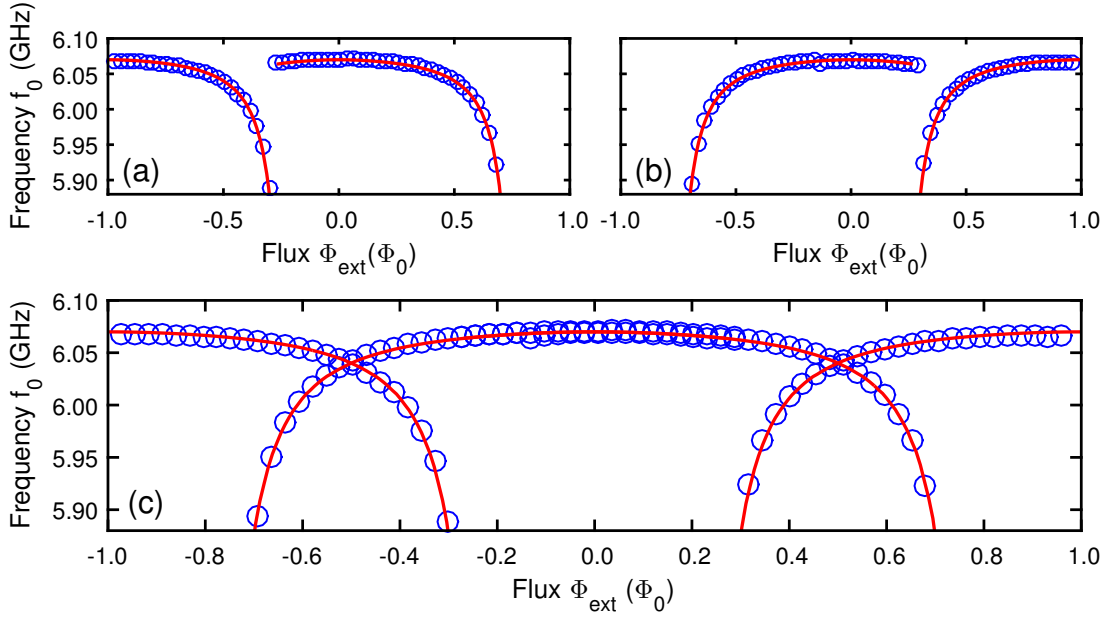


**Figure 4.10:** Resonant frequency  $f_0$  of JPA Q600 (blue circles), extracted from fitting the magnitude and phase with input-output formalism and fitted flux dependence (red). (a) and (b) show the resonant frequency for increasing and decreasing external flux, respectively, and (c) the combined resonant frequencies for both sweep directions. For fitting results see table 4.1.

the upper branches, we introduce a switching current  $j_c^{\text{sw}}$  in the simulations. If the present local minimum of the phase particle has a lower  $j_c$  than  $j_c^{\text{sw}}$ , then the particle jumps to another potential minimum, even though the present minimum did not vanish yet. The switching currents  $j_c^{\text{sw}}$  can be understood as a noise floor originating from internal losses and contributions from external noise. For a shallow potential minimum small flux changes or transport currents, induced by a noisy setup or the environment, are enough to lift the particle out of the present minimum before the minimum vanishes. Furthermore, internal losses are connected to a certain noise level. We note that including  $j_c^{\text{sw}}$  in the simulations only changes the jump points but does not influence the overall dependence shown in Fig. 4.10 (c).

To obtain  $I_c$  from the fitting parameters, we estimate  $L_{\text{res}}$  from the geometrical design parameters and matching to  $50 \Omega$ , and obtain  $L_{\text{res}} = 2 \text{ nH}$ . Table 4.1 summarizes the obtained results. We find a screening parameter of  $\beta_L = 0.592$ , critical current of one Josephson junction of  $I_c = 26.76 \mu\text{A}$  and a resonant frequency of the bare resonator of  $f_{\text{res}} = 6.158 \text{ GHz}$ .  $I_c$  is substantially higher than the design parameter  $I_c^{\text{design}} = 4 \mu\text{A}$ , thus resulting in a relative high  $\beta_L$  parameter leading to hysteretic behavior. We attribute this deviation to problems in the fabrication process of the JPA, since we observed a similar hysteretic behavior in a different JPA sample.

Fig. 4.11 depicts the flux dependence of the resonant frequency of JPA Q200 and JPA Q200new. For both measurements the coil current was only increased, since no

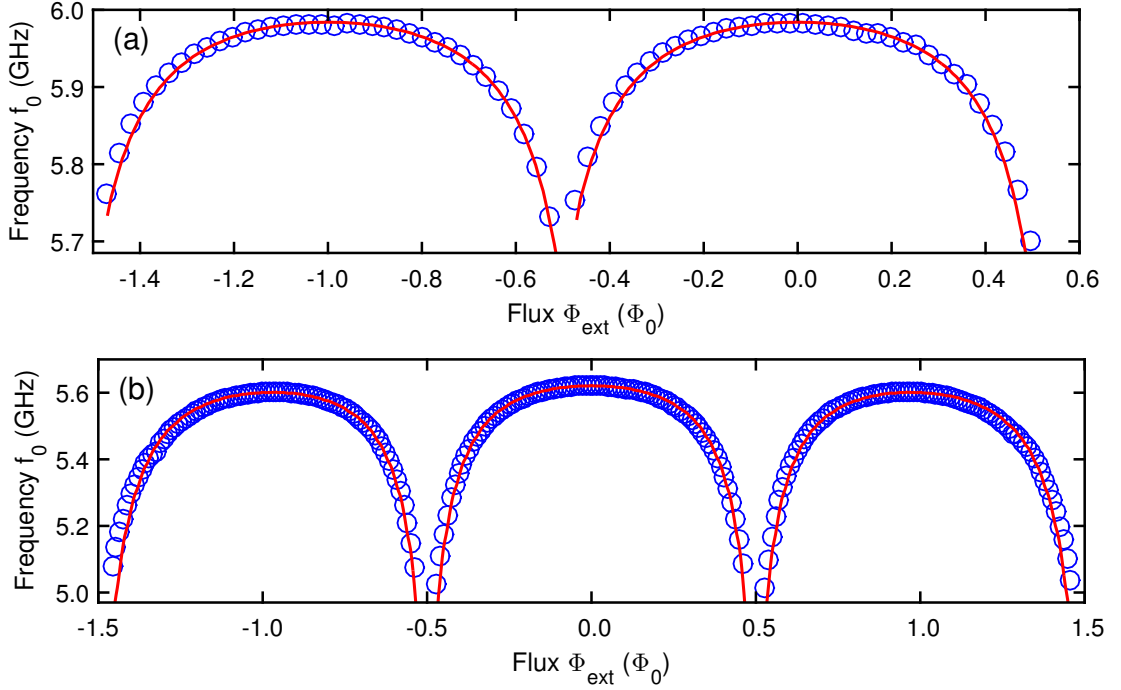


**Figure 4.11:** Resonant frequency  $f_0$  of (a) JPA Q200 and (b) JPA Q200new (blue circles), extracted from fitting the magnitude and phase with input-output formalism and fitted flux dependence (red). For fitting results see table 4.1.

Sample	$I_c$ ( $\mu\text{A}$ )	$\beta_L$	$f_{\text{res}}$ (GHz)	$E_j/h$ ( $10^3 \cdot \text{GHz}$ )	$2I_c \cdot j_c^{\text{sw}}$ ( $\mu\text{A}$ )
JPA Q600	26.76	0.592	6.158	13.29	3.05
JPA Q200	5.72	0.24	6.070	2.84	1.64
JPA Q200new	3.30	0.10	5.849	1.64	$>0.26$

**Table 4.1:** Fitting results of flux dependence of the resonant frequency for the measured samples JPA Q600, JPA Q200 and JPA Q200new under the estimation of  $L_{\text{res}} = 2 \text{ nH}$ .

pronounced hysteretic behavior is visible in the measured frequency range. Again the fitting results are summarized in table 4.1. Both  $I_c$  are now closer to the design parameter of  $I_c^{\text{design}} = 2 \mu\text{A}$ , resulting in lower  $\beta_L$  parameters. The switching current  $2I_c \cdot j_c^{\text{sw}}$  of JPA Q200 is significantly larger than for JPA Q200new, indicating a higher noise level in JPA Q200. This also coincides with the fact, that for JPA Q200new we observed very high internal quality factors, which corresponds to a lower internal contribution to the noise level and thus leading to a reduced switching current.

In order to fit the flux dependence of JPA Q200new properly, one also needs to include a modulation of  $j_c$  caused by a parasitic in-plane component of the magnetic fields penetrating the insulating tunnel barrier of the Josephson junctions. Thus, we obtain an additional modulation  $j_c(\Phi_{\text{ext}}) \rightarrow j_c(\Phi_{\text{ext}}) \cdot |\text{sinc}(B\pi\Phi_{\text{ext}}/\Phi_0)|$  [67]. The factor  $B$  accounts for the fact, that the flux penetrating the dc-SQUID loop perpendicular to the plane

$\Phi_{\text{ext}}$  and the in-plane flux through the tunnel barriers of the Josephson junctions are not the same but approximately proportional to each other. We observe this effect, because the magnetic field generated by the superconducting coil is not perfectly homogeneous or the placement of the coil is such, that the field is not exactly perpendicular to the dc-SQUID loop. For the other samples JPA Q200 and JPA Q600 the in-plane magnetic field is negligible, probably due to the placement of the coil on the sample box.

To summarize, we found an approach to describe hysteretic and non-hysteretic behaviors of the resonant frequencies of Josephson parametric amplifiers based on a  $\lambda/4$  resonator shunted with a dc-SQUID to the ground. We achieve this by simulating the position of the phase particle in the two-dimensional tilted washboard potential of the dc-SQUID, whose topology strongly depends on the screening parameter  $\beta_L$ . Furthermore, we apply a distributed-element model to describe the flux dependent resonant frequency  $f_0$  of the JPA. We conclude, that even for small screening parameters  $\beta_L$ , one obtains a quantitatively different dependence of  $f_0$  on the external flux as compared to the case with  $\beta_L = 0$ .

#### 4.1.4 Comparison to literature

Dc-SQUIDs with various  $\beta_L$  factors have already been extensively investigated in literature [68–71]. All approaches make use of numerical calculations to describe the flux dependence of the maximal supercurrent but investigate the dc-SQUID independently. In our experiments, the dc-SQUID is grounding a resonator, which leads to a characteristic change in the resonant frequency of the JPA. We only measure the resonant frequency, which is related to the inductance of the dc-SQUID by Eq. (4.4). The actual transport current through the dc-SQUID  $I_{\text{tot}}$  is at all times very small or vanishing, since we do not apply a dc-bias to the JPA. Therefore, in the presented experiments we only probe the inductance (see Eq. (4.3)), and thus  $j_c$  and not the maximum supercurrent  $I_c^{\text{max}}$  of the dc-SQUID. These two maximum currents differ in the condition how to choose the local minimum for the determination of the critical current. For  $j_c$ , one chooses the present local minimum of the phase particle, regardless of whether it is the deepest or a shallow one, and for  $I_c^{\text{max}}$  the deepest minimum is chosen.  $I_c^{\text{max}}$  then gives the maximal transport current at which the dc-SQUID is still in the zero-voltage state. Above this threshold, the dc-SQUID goes into the voltage state<sup>4</sup>.

Our simulation can be easily adjusted to also reproduce the well known modulation of the maximal supercurrent  $I_c^{\text{max}}$  depending on the externally applied flux  $\Phi_{\text{ext}}$  for different  $\beta_L$ . One just needs to replace the condition that the phase particle stays in the present minimum as long as it exists with the condition that it always resides in the deepest local minimum. Fig. 4.12 shows the resulting dependence for various screening parameters  $\beta_L$  as it can also be seen in Refs. [52, 71]. With increasing  $\beta_L$  the modulation of the maximum supercurrent is reduced.

<sup>4</sup>In fact the actual switching transport current to bring the dc-SQUID into the voltage state depends on the noise level and the junction parameters [52, 71].

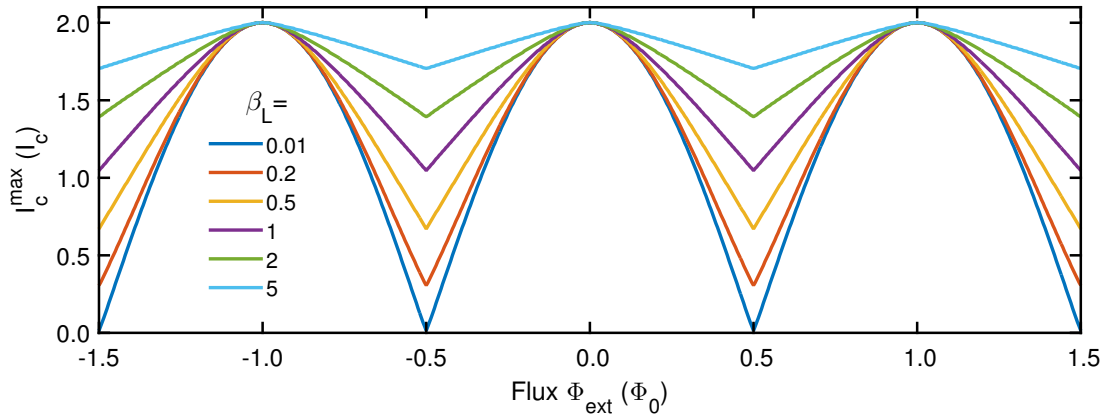


**Figure 4.12:** Maximum supercurrent of a dc-SQUID  $I_c^{\max}$  vs. external flux  $\Phi_{\text{ext}}$  for different screening parameters  $\beta_L$ .

## 4.2 Non-degenerate operation mode

### 4.2.1 Non-degenerate signal gain

Now the JPA is operated in the non-degenerate mode, meaning it acts as a phase-insensitive amplifier for an input signal at a frequency  $f_0 - \Delta f$ . To this end, we turn the pump in Fig. 4.1 on and set it to a frequency  $2f_0$  which is approximately twice the resonant frequency of the JPA without pump signal. In addition to the amplified signal at  $f_0 - \Delta f$ , an idler signal at  $f_0 + \Delta f$  is generated. As long as  $\Delta f$  is finite and thus signal and idler are at different frequencies, the JPA is operated in the non-degenerate mode.

Fig. 4.13 (a) shows the signal gain spectra for different pump powers at a pump frequency of  $2f_0 = 11.02$  GHz and a coil current of  $44 \mu\text{A}$  for JPA Q200new. The measurement is performed with a VNA by sweeping the frequency of the signal at the input to the JPA and measure the reflected signal. We thus measure only the signal gain and not the idler mode. A measurement with the pump tone turned off serves as reference measurement.

Up to a certain pump power, the signal gain increases and reaches a maximum at approximately 15 dB. For higher pump powers the signal gain decreases again, since non-linear effects set in, which hinder the signal amplification. From fitting each spectrum with a Lorentzian, we extract the maximal signal gains in Fig. 4.13 (b). The maximal signal gain for a given pump power is observed at approximately half the pump frequency  $f_0$ . In the data analysis we discard points at exactly  $f_0$ , since  $\Delta f = 0$  would mean phase sensitive degenerate amplification. In the recorded spectra, we see the effect of phase-sensitive degenerate amplification by random pronounced dips or peaks at  $\Delta f = 0$ . The dips or peaks are randomly appearing, since the VNA does not preserve the start phase for each frequency sweep and so the relative phase between VNA signal and pump tone changes for every frequency sweep.

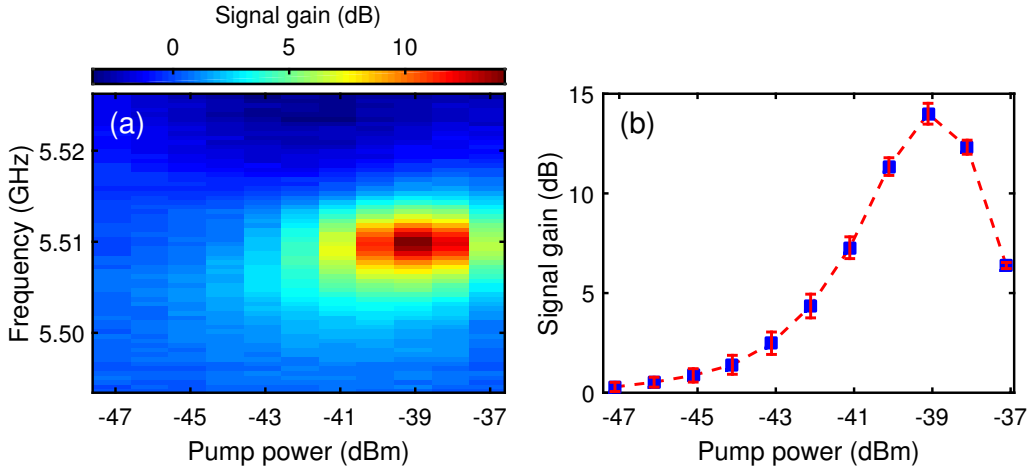


**Figure 4.13:** (a) Spectrum of the non-degenerate signal gain vs. pump power and (b) extracted maximal signal gains from Lorentzian fits for JPA Q200new. The pump frequency is at  $2f_0 = 11.02$  GHz and the coil current is  $44 \mu\text{A}$ . Error bars show 95% confidence bounds of fits.

We note that the optimal pump frequency for a given external flux is not necessarily twice the resonant frequency of the JPA at zero pump power, but rather depends on the pump power, since the pump tone will shift the resonant frequency to slightly lower values. The slightly deamplified region in Fig. 4.13 (a) can be explained by a not perfectly chosen pump frequency. If the pump frequency is too high or too low, when compared to the optimal point, one observes a dip-peak structure in a recorded spectrum as we see in the shown data for pump powers between 12 and 18 dBm.

## 4.2.2 Noise properties

The noise properties of an amplifier are important characteristics, since they describe the degradation of the signal-to-noise ratio during amplification. In our experiments, the added noise by the JPA will limit the maximum squeezing level which can be observed. We use a spectrum analyzer to measure the noise power of the two amplification chains depending on the temperature of an attenuator, acting as noise source in front of JPA Q200. The spectrum analyzer is connected to the corresponding AMT-A0033 amplifier output in Fig. 3.6 and no input or displacement signal is applied. We set the JPA to a non-degenerate signal gain of 10.7 dBm at a pump frequency of  $2f_0 = 11.788$  GHz. The spectrum analyzer is set to a resolution bandwidth of  $RBW = 200$  kHz and a video bandwidth of  $VBW = 500$  kHz. The JPA is stabilized to 50.5 mK during the measurement.

The noise power depending on the attenuator temperature  $T_{\text{att}}$  can be described by [66]

$$P(T_{\text{att}}) = GB \left[ \frac{hf_0}{2} \coth \left( \frac{hf_0}{2k_{\text{B}}T_{\text{att}}} \right) + k_{\text{B}}T_{\text{total}} \right], \quad (4.5)$$

where  $h$  is the Planck constant,  $k_{\text{B}}$  the Boltzmann constant,  $G$  the gain of the whole amplification chain and  $B$  the bandwidth of the detector, given by the resolution bandwidth

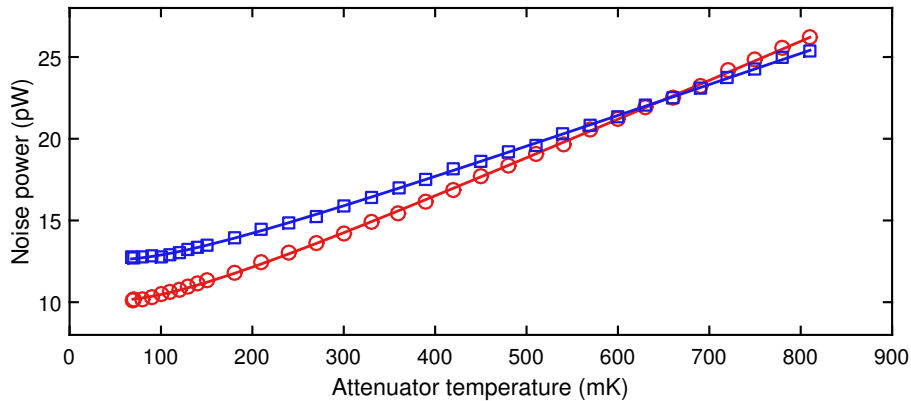


**Figure 4.14:** Detected noise power for different attenuator temperatures, acting as noise source, for chain 1 (blue squares) and chain 2 (red circles). JPA Q200 is set to a signal gain of 10.7 dBm at a pump frequency of  $2f_0 = 11.788$  GHz. Solid lines are fits according to Eq. 4.5.

$RBW$ .  $T_{\text{total}}$  gives the total noise temperature of the amplification chain, including the JPA and HEMT amplifier. The first term in Eq. (4.5) describes the emitted noise power with frequency  $f_0$  of a black body radiator at temperature  $T_{\text{att}}$ .

A heatable 30 dB attenuator acts as such a black body radiator and is connected to a measurement circulator via a 17 cm stainless steel coaxial cable. By taking the total loss of approximately 1.5 dB from the attenuator to the measurement circulator into account, we obtain the effective power incident to the JPA. The losses are modeled with the beam splitter model.

By fitting the detected noise power for different attenuator temperatures for both amplification chains, we obtain  $T_{\text{total},1} = 233 \pm 4$  mK and  $T_{\text{total},2} = 445 \pm 5$  mK, corresponding to  $n_{\text{total},1} = 0.82 \pm 0.01$  and  $n_{\text{total},2} = 1.57 \pm 0.02$  noise photons for chain 1 and chain 2, respectively. Uncertainties are given from 95% confidence bounds from fitting. We observe, that we only add a little amount of noise photons to the signal in the whole amplification chains. Chain 1 is close to the standard quantum limit for phase-insensitive amplification of 0.5 photons. Even though the setup for both chains is equal, chain 2 adds roughly double the noise photons. Noise photons are inevitably added by the JPA and the rest of the amplification chain, including the HEMT amplifier, room temperature amplifiers and various microwave components. If we also consider the gains  $G_1 = (9.74 \pm 0.06) \cdot 10^6$  and  $G_2 = (7.75 \pm 0.05) \cdot 10^6$  for chain 1 and 2, respectively, we attribute the additional added noise to a lower amplification in chain 2, which leads to a worse signal to noise ratio. In fact, we observed a poorer performance of the fridge output 2, corresponding to amplification chain 2, also for PNCF calibration measurements, which were discussed in Sec. 3.2.3. However, the measurements shown here, were recorded before the improvements of the setup. With the improved setup, the noise properties of both amplifications chains are similar.

For a detailed characterization of JPA Q200 and JPA Q600, we refer the reader to Ref. [72] and the upcoming master thesis of Martin Betzenbichler.



# Chapter 5

## Displacement of squeezed microwave states

In protocols for quantum information processing, such as remote state preparation, quantum teleportation and quantum cryptography, control over quantum states is essential. A linear transformation is an important building block for such protocols. For propagating quantum microwaves, the displacement operation facilitates such a linear transformation in phase space.

We study displaced squeezed states, where a vacuum state, incident to the JPA, is squeezed, transmitted, and subsequently displaced with a directional coupler. The resulting states take the form  $\hat{D}(\alpha)\hat{S}(\xi)|0\rangle$ . In principle, one could apply such a displacement operation to an arbitrary state incident to the directional coupler.

If not stated otherwise, the cryogenic and the room temperature setup schemes shown in Fig. 3.2 and Fig. 3.6 are used for the measurements. All shown measurements are performed with JPA Q200new.

### 5.1 Squeezed vacuum states

In order to produce a single-mode squeezed state, one needs to operate the JPA in the degenerate mode. This means that the frequency of an input signal needs to coincide with half the pump frequency. The Acqiris card is referenced to a rubidium source with 10 MHz.

Even if no signal is applied one always has a broadband vacuum state incident to the JPA input. By choosing a suitable working point and applying a pump tone, one can produce squeezed vacuum states as shown in Fig. 5.1. First, we choose a coil current of  $20\ \mu\text{A}$ , corresponding to a flux of  $0.17\ \Phi_0$  inside the dc-SQUID loop. This working point has a corresponding JPA frequency  $f_0 = 5.594\ \text{GHz}$ . At an estimated pump power  $P_{\text{pump}} = -39\ \text{dBm}$  at the input of the JPA sample box, 3.0 dB of non-degenerate signal gain is obtained. The JPA temperature is stabilized at 40 mK. As discussed in Sec. 3.2.3, an accurate PNCF calibration of the whole detection chain is crucial to reconstruct the correct state at the input to the hybrid ring, so a new PNCF calibration is performed before the measurements.

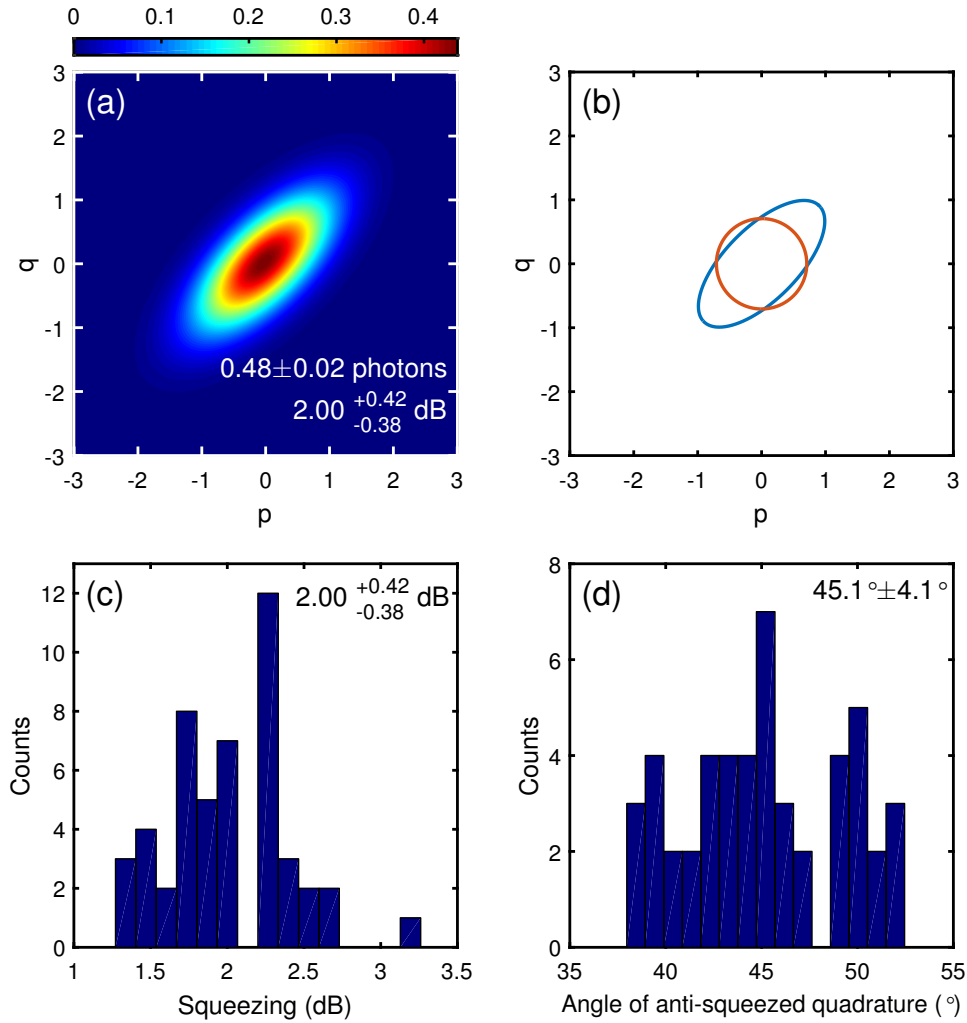


**Figure 5.1:** Evaluation of 50 measurements based on the dual-path detection. Each measurement contains  $5.6 \times 10^8$  raw data samples at a working point of  $f_0 = 5.594$  GHz. (a) Reconstructed Wigner function, calculated from the average of all 50 measurements. The average photon number and the average squeezing of the state are indicated. (b)  $1/e$  contour of the ideal vacuum state (orange) and squeezed vacuum state (blue).  $p$  and  $q$  are dimensionless variables spanning the phase space. (c) Histogram of reconstructed squeezing levels with an average of  $\mathcal{S} = 2.00_{-0.38}^{+0.42}$  dB. The averaging is performed on linear scale and afterwards converted to logarithmic scale. (d) Histogram of reconstructed angles of the anti-squeezed quadratures with an average of  $\gamma = 45.1^\circ \pm 4.1^\circ$ . The JPA temperature is stabilized at 50 mK.

All shown measurements are performed using the following phase stabilization protocol to stabilize the angle of the anti-squeezed quadrature  $\gamma$ . For that, a short measurement is recorded and state reconstruction is performed. The deviations from the setpoint in the reconstructed angle  $\gamma$  are corrected by changing the phases of the respective microwave source. In that way a higher degree of stability for the angles is obtained. In total 50 measurements with subsequent phase correction after state reconstruction are performed. Each measurement consists of  $5.6 \times 10^8$  raw data samples. Fig. 5.1 (a)

shows the reconstructed Wigner function calculated from the averaged moments of each measurement. We emphasize, that the reconstructed state corresponds to the input of the hybrid ring. The total photon number is  $0.48 \pm 0.02$  with an average squeezing of  $\mathcal{S} = 2.00_{-0.38}^{+0.42}$  dB. The averaging for the squeezing level is performed on linear scale and then converted to logarithmic scale. The  $1/e$ -contours (Fig. 5.1 (b)) show that the squeezed state (blue) is indeed squeezed below the vacuum (orange). The third and fourth order cumulants are small or vanish, giving a strong indication for the Gaussianity of the reconstructed states (see Appendix B). In Fig. 5.1 (c), the statistics of the reconstructed squeezing levels is shown. The deviations from the mean value can be explained by a limited detection efficiency of the Acqiris card based setup. Due to data processing on a CPU, one obtains rather slow averaging capabilities when compared to a FPGA based setup with real-time data processing. The reconstructed angles of the anti-squeezed quadrature  $\gamma = 45.1^\circ \pm 4.1^\circ$ , shown in Fig. 5.1 (d), also deviate from the setpoint of  $\gamma_{\text{set}} = 45^\circ$ , which again are explained by the limited detection efficiency.

## 5.2 Squeezing versus signal gain

### 5.2.1 Experimental results

By increasing the pump power, the amplitude of the modulation of the resonant frequency of the JPA also increases. This translates into an increased signal gain in the degenerate and the non-degenerate operation modes of the JPA, which leads to a higher squeezing level and higher photon numbers in the state as depicted in Fig. 5.2. The operation point and the PNCF calibration are the same as in the previous section. At this working point, we achieve the largest squeezing of  $\mathcal{S} = 2.00_{-0.38}^{+0.42}$  dB at a signal gain of 3.0 dB. If the signal gain is further increased, we observe a decrease in the squeezing level. This is attributed to the fact, that the JPA enters the bifurcation regime for high pump powers and thus high signal gains. In this regime, the squeezing is reduced, since higher order effects set in [30]. Fig. 5.2 and Fig. 5.3 (a) illustrate this behavior. The squeezing level as well as the photon number increase until a signal gain of 3.0 dB. Beyond this signal gain, the squeezing level decreases while the photon number still increases further. Also, for these high signal gains the higher order cumulants do not vanish anymore, in contrast to lower signal gains where the cumulants are reasonably small or vanish. In Sec. 5.2.2 we discuss the data in the context of two models describing the squeezing level by considering thermal contributions to the ideal squeezed vacuum states.

In the ideal case, we can identify the signal voltage gain in the non-degenerate mode with the squeezing factor  $G_v = \cosh(r)$  [23, 44]. Furthermore, the number of photons in a squeezed state is given by  $n_{\text{sq}} = \sinh^2(r)$  (see Eq. 2.33). Using both relations and

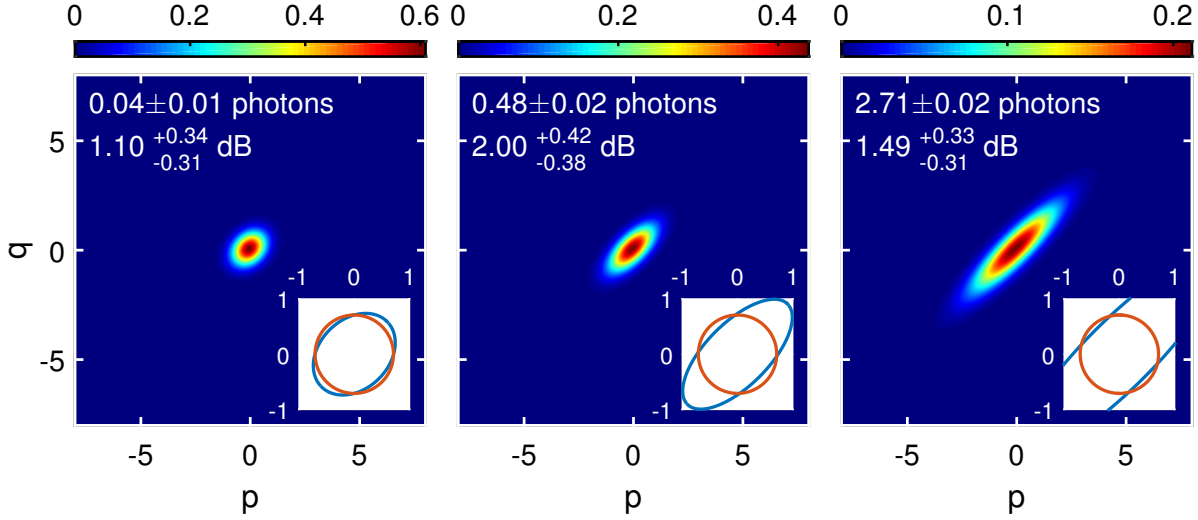


**Figure 5.2:** From left to right: Reconstructed Wigner functions for signal gains of 0.8 dB, 3.0 dB and 8.1 dB for a squeezing angle  $\gamma = 45^\circ$  at the working point of  $f_0 = 5.594$  GHz. For each signal gain, 50 measurements with the phase stabilization protocol are performed, where each measurement is averaged over  $5.6 \times 10^8$  raw data samples. The average photon number and the average squeezing of the states are indicated. Insets show  $1/e$  contours of the ideal vacuum state (orange) and corresponding squeezed vacuum state (blue). The JPA temperature is stabilized at 50 mK.

$\cosh^2(r) - \sinh^2(r) = 1$ , one can write

$$n_{\text{sq}} = G_p - 1, \quad (5.1)$$

where  $G_p = G_v^2$  is the signal power gain in the non-degenerate mode of the JPA. Thus, one expects a linear dependence of the photon number in a pure squeezed state on the non-degenerate signal power gain. The slope is one and the y-intercept is -1. However, from fitting we extract the dependence  $n_{\text{sq}} = -0.51G_p - 0.58$ , as shown in Fig. 5.3 (b). The difference by a factor of approximately 1/2 is explained by the contribution of an parasitic unsqueezed red sideband to the detected signal. The sideband only contains weakly non-degenerate amplified vacuum. The presence of a sideband contribution during the PNCF calibration of the detection chains leads to a reduction of the reconstructed number of photons in the squeezed state by approximately a factor of 1/2. For details concerning the red sideband contribution, we refer to Sec. 5.2.2.

Next the working point is shifted to a coil current of  $44 \mu\text{A}$  corresponding to a flux of  $0.28 \Phi_0$  through the dc-SQUID loop. This working point has a lower frequency of 5.51 GHz, meaning that the slope of the resonant frequency as a function of the external flux is higher compared to the previous working point at 5.594 GHz. Therefore, for the new working point, we expect higher non-degenerate signal gains of the JPA at the same pump powers compared to the previous working point. We confirm this behavior in our experiments.

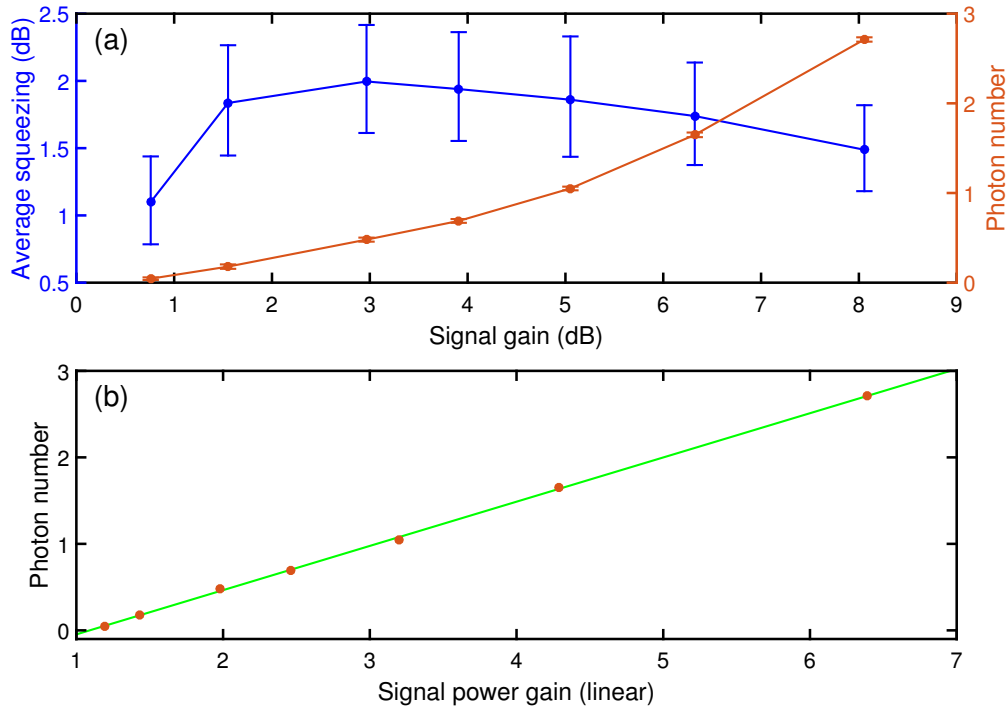


**Figure 5.3:** (a) Average squeezing below vacuum (blue) and photon number (orange) versus non-degenerate signal gain for a working point at 5.594 GHz. For each signal gain, 50 measurements with the phase stabilization protocol are performed, where each measurement is averaged over  $5.6 \times 10^8$  raw data samples. The working point is 5.594 GHz. The lines are guides for the eyes. The error bars are of statistical nature. (b) Photon number (orange) as a function of signal power gain in linear units. The green line is a linear fit. The JPA is stabilized at 50 mK.

In contrast to the previous measurements, the Acqiris card is not referenced to a rubidium source with 10 MHz and IQ-mixers (Marki, IQ4509LXP) instead of single ended mixers are used. The phase stability protocol is comprised of 150 measurements, where each measurement is averaged over  $1.68 \times 10^8$  raw data samples. Fig. 5.4 (a) shows the squeezing level and the photon number as a function of the signal gain. The highest squeezing of  $\mathcal{S} = 1.41_{-0.59}^{+0.77}$  dB is achieved at a signal gain of 1.4 dB. For higher signal gains, the squeezing level decreases again, while the number of photons in the state still increases, similar as for the working point at 5.594 GHz. For the highest two signal gains, no squeezing below vacuum is observed anymore.

For this working point, the photon number as a function of the signal power gain (see Fig. 5.4 (b)) exhibits the dependence  $n_{\text{sq}} = 0.97G_p - 0.95$ , extracted from fitting. This result is in good agreement with Eq. (5.1), however the sideband is also present for this working point. Thus, we would expect a similar behavior as for the working point at 5.594 GHz, where the slope is approximately 1/2. We attribute this to the fact that the gain calibration for the pump power is not accurate or  $n_{\text{sq}} = \sinh^2(r)$  is not valid for this working point, since it does not take into account possible thermal contributions to the number of photons.

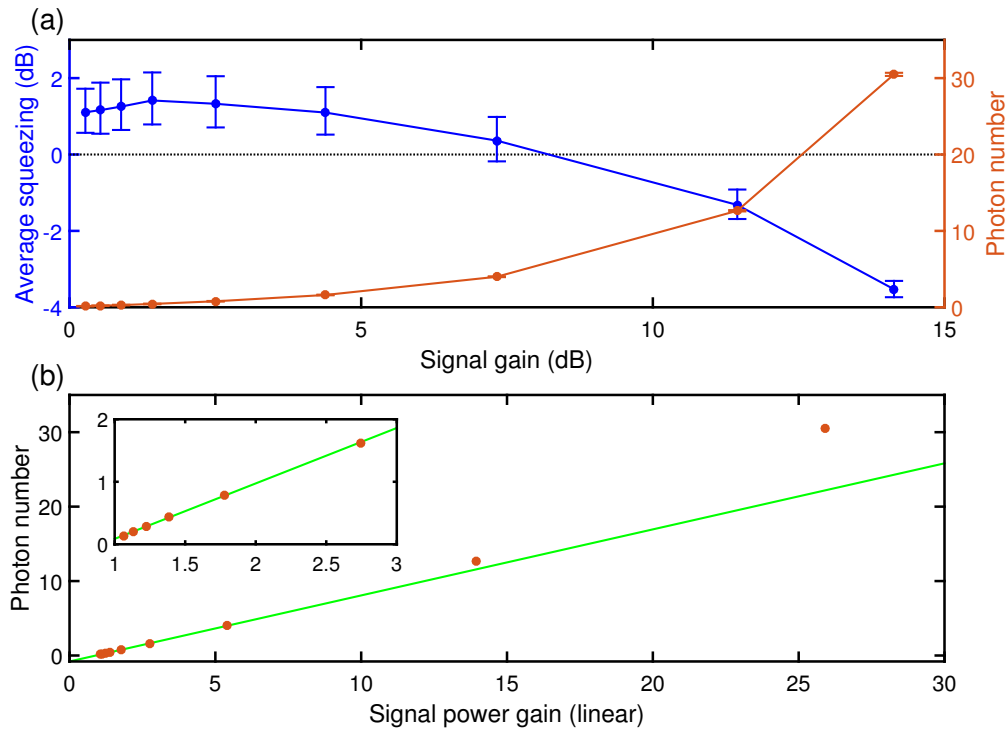


**Figure 5.4:** (a) Average squeezing (blue) and photon number (orange) versus non-degenerate signal gain for a working point at 5.51 GHz. For each signal gain, 150 measurements with the phase stabilization protocol are performed, where each measurement is averaged over  $1.68 \times 10^8$  raw data samples. The lines are guides for the eyes. The error bars are of statistical nature. (b) Photon number (orange) as a function of non-degenerate signal power gain in linear units. The green line is a linear fit, excluding the data for the highest gain. The JPA and the 30 dB attenuator temperatures are stabilized at 40 mK and 60 mK, respectively.

## 5.2.2 Models describing the squeezing level

From the theoretical model of a JPA based on the input-output formalism as described in Sec. 2.2.6, we would expect much higher levels of squeezing for the shown measurements. In the following we present two approaches for explaining the reconstructed states and give upper bounds for the achievable squeezing levels.

### Thermal squeezed vacuum state

The first approach assumes, that a vacuum state is incident to the JPA input. If a pump tone is applied, a squeezed vacuum state will be produced by the JPA. Now a certain amount of thermal photons  $n_{\text{th}}$  is added to the signal. This contribution of thermal photons may arise from various sources. On the one hand, we recently discovered, that a second sideband is down-converted into the intermediate frequency. This sideband effectively adds noise photons to the detected signal (see next part for further details). On the other hand, we observed trigger problems with the Acqiris card. This gives rise to

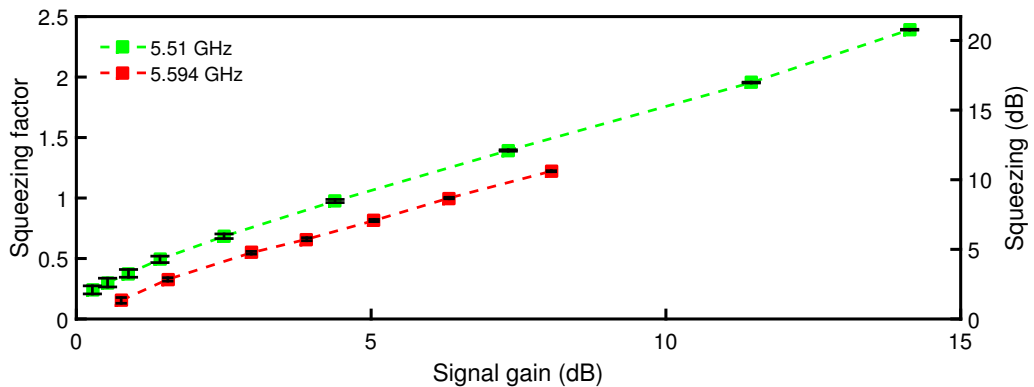


**Figure 5.5:** Squeeze factor  $r$  and squeezing level  $\mathcal{S}$  as a function of the non-degenerate signal gain of the JPA. Values are shown for the two working points at 5.51 GHz (green) and 5.594 GHz (red). Lines are guides for the eyes. The error bars are of statistical nature. The squeezing is related to  $r$  via  $\mathcal{S} = 20r \log_{10}(e)$ . Squeezing factors  $r$  are calculated for thermal squeezed states from the dual-path reconstruction.

phase fluctuations of the squeezing angle  $\gamma$  as well as the displacement angle  $\theta$ . Since these fluctuations are correlated between the two detection channels, the dual-path method assumes these fluctuations are already present at the input to the hybrid ring. The fluctuations degrade the signal, if the signal is not rotationally invariant. Thus, squeezed, coherent, and displaced squeezed states are affected by the trigger problems, whereas thermal and vacuum states are unaffected. Noise photons are also partially added by inevitable cable losses, JPA losses, and connection losses before the input to the hybrid ring. Also spurious correlations between the two amplification paths can lead to an altered reconstructed signal at the hybrid ring input. Using the relations between the moments  $\langle (\hat{a}^\dagger)^m \hat{a}^n \rangle$  up to second order and the squeezing parameters  $r, \varphi$  as well as the displacement amplitude  $\alpha$  (see Eqs. (2.31-2.33)), one obtains a system of equations, which can be solved to obtain  $r, \varphi, \alpha$  and  $n_{\text{th}}$  from the measured moments. For that, the moment  $\langle \hat{a}^\dagger \hat{a} \rangle$  is modified to also account for thermal photons in the signal

$$\langle \hat{a}^\dagger \hat{a} \rangle = |\alpha|^2 + \sinh^2 r + n_{\text{th}}. \quad (5.2)$$

We apply this analysis to our data for the working points at 5.594 GHz and 5.51 GHz shown in Fig. 5.3 and 5.4, respectively. The resulting squeezing factors  $r$  for both working points are depicted in Fig. 5.5. Furthermore, the squeezing level  $\mathcal{S}$  calculated from the squeezing factor by  $\mathcal{S} = 20r \log_{10}(e)$  is also shown. One observes that the predicted squeezing levels (see Fig. 5.5) are well beyond the maximum squeezing we observed directly in our experiments (see Fig. 5.3 and 5.4). For example at the respective signal gains with the highest measured squeezing levels, we obtain 4.8 dB and 4.3 dB of squeezing for the working points at 5.594 GHz and 5.51 GHz, respectively. In our experiments we do not observe these squeezing levels directly, since thermal photons from the unwanted

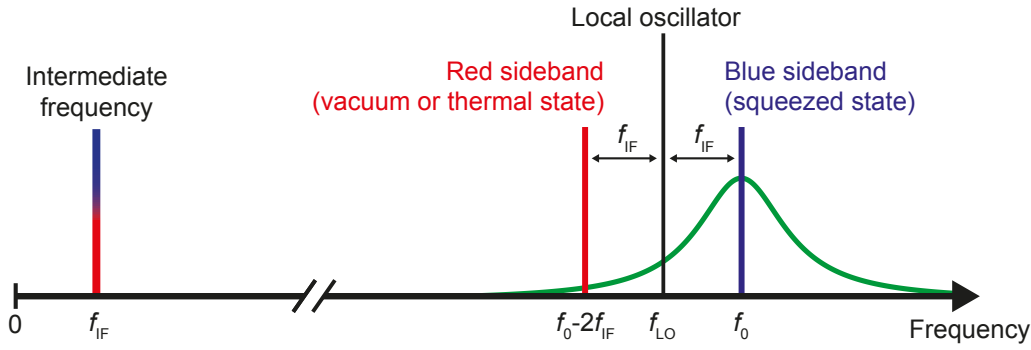


**Figure 5.6:** Sketch of the sidebands. The local oscillator with a frequency  $f_{LO}$  defines two sidebands, which are down-converted to the intermediate frequency  $f_{IF}$ . The blue sideband with a frequency equal to the working point  $f_0$ , contains a squeezed state from degenerate amplification. The red sideband with a frequency of  $f_{sb} = f_0 - 2f_{IF}$  contains a vacuum or thermal state, due to a certain bandwidth of the non-degenerate amplification of the JPA (green line).

sideband pollute our IF signal and increase the variance of the squeezed quadrature. Even contributions on the level below one thermal photon increase the reconstructed state variance drastically.

We note, that in theory the squeezing factor or, equivalently, the squeezing level of a noiseless JPAs should be the same at identical signal gains for different working points. However, the working point at 5.594 GHz exhibits lower squeezing factors compared to the other one, which is attributed to the fact that the JPA is not a perfect noiseless amplifier. This means that effectively a thermal state is incident to the JPA input, which will then be amplified by the JPA. Under the assumption that a thermal state is added after the JPA, this leads to higher calculated squeezing factors. In turn this means, that at the working point of 5.51 GHz, the JPA already adds more noise photons to the input signal, which can be attributed to the higher sensitivity of the resonant frequency of the JPA to an externally applied flux and, thus, to flux noise. This is also observed for the extracted thermal photons  $n_{th}$  depicted in Fig. 5.7 (b) and Fig. 5.8 (b) for the two working points. At the same signal gains, more thermal photons are added to the squeezed state at the working point of 5.51 GHz.

### Contributions of a sideband

At later stages of our experiment, we discovered that during mixing of the RF-signal with the local oscillator to the intermediate frequency  $f_{IF}$  of 11.5 MHz, a red sideband with frequency  $f_{sb} = f_0 - 2f_{IF}$  is also down-converted to the intermediate frequency. This means that for a working point at 5.51 GHz and intermediate frequency of 11.5 MHz, also a signal contribution from 5.487 GHz is present after mixing<sup>1</sup>. At this red sideband the

<sup>1</sup>In our experiments, we choose the local oscillator frequency to be below the working point frequency  $f_0$ . So the red sideband is always located at  $f_0 - 2f_{IF}$ , where  $f_{IF}$  is the intermediate frequency.

non-degenerate signal gain of the JPA is small but nevertheless finite. Due to the small detuning of  $f_{\text{sb}}$  from the working point frequency  $f_0$ , both sidebands are amplified equally in the amplification chains and finally mixed to the same intermediate frequency by a mixer (see Fig. 5.6). Since we use a single ended, harmonic double-balanced mixer, it is not possible to filter the red sideband contribution from the signal at the desired frequency digitally.

Therefore, we developed a basic model including the red sideband contribution in order to estimate the effect of the sideband on the squeezing level. Both bands are superposed with the beam splitter model. The reconstructed variance of the squeezed quadrature  $(\Delta q_{\text{sq}})^2$  is determined by a contribution from a squeezed vacuum and from a vacuum or a thermal state from the red sideband

$$(\Delta q_{\text{sq}})^2 = \eta \left( \frac{1}{4} G_{\text{d}}^{\text{min}}(A_{\text{pump}}) \right) + (1 - \eta) \left( \frac{1}{4} + \frac{1}{2} \tilde{n}_{\text{th}} G_{\text{p}}(A_{\text{pump}}) \right), \quad (5.3)$$

where  $A_{\text{pump}}$  is the pump amplitude,  $\eta = 0.5$  is the contribution of each sideband and  $G_{\text{p}}(A_{\text{pump}})$  is the measured non-degenerate signal power gain depending on the pump amplitude and  $\tilde{n}_{\text{th}}$  a constant, so that  $\tilde{n}_{\text{th}} G_{\text{p}}(A_{\text{pump}})$  gives the thermal photons for the respective signal gain. The first term represents the variance of the squeezed quadrature of the band we want to measure and the second term the variance of a thermal state in the red sideband. Both bands are treated equally by the amplification paths, so the weight of both is  $1/2$ , hence  $\eta = 0.5$ .

$G_{\text{d}}^{\text{min}}$  is the minimal signal gain of the JPA in the degenerate operation mode (see Eq. (2.103)) and depends, after the substitution  $\delta \rightarrow (A_{\text{pump}} - \Delta A)\epsilon_{\text{a}}$ , on  $A_{\text{pump}}$

$$G_{\text{d}}^{\text{min}}(A_{\text{pump}}) = \left( \frac{2(A_{\text{pump}} - \Delta A)\epsilon_{\text{a}}\omega_0 - \frac{\kappa_1 - \kappa_2}{2}}{2(A_{\text{pump}} - \Delta A)\epsilon_{\text{a}}\omega_0 + \frac{\kappa_1 + \kappa_2}{2}} \right)^2, \quad (5.4)$$

where  $\epsilon_{\text{a}}$  is a conversion factor from a pump amplitude to a frequency modulation  $\delta$ ,  $\omega_0$  is the resonant frequency of the JPA,  $\kappa_1, \kappa_2$  are the coupling rates and  $\Delta A$  an offset of the pump amplitude, describing the onset of the frequency modulation  $\delta$ . The offset is explained by the fact that in experiments we only control the pump amplitude  $A_{\text{pump}}$  at the microwave source, but a resonant frequency modulation  $\delta$  is induced by the magnetic field threading the dc-SQUID loop generated by the pump line. We use a linear approach to describe the dependence  $\delta(A_{\text{pump}})$ , however higher order terms might also play a role, which can lead to an offset  $\Delta A$  in the linear approach. Second, vacuum or weak thermal fluctuations induce flux fluctuations in the dc-SQUID loop. In order to amplify or squeeze a signal with a JPA, the pump amplitude at the JPA and the thereby induced flux need to be larger than these fluctuations. Thus, a certain threshold  $\Delta A$  of the pump amplitude at the microwave source needs to be exceeded.

By fitting our data for the two working points at 5.594 GHz and 5.51 GHz with Eq. (5.3), we obtain Fig. 5.7 and Fig. 5.8, respectively. The fitting results are summarized in Tab. 5.1.

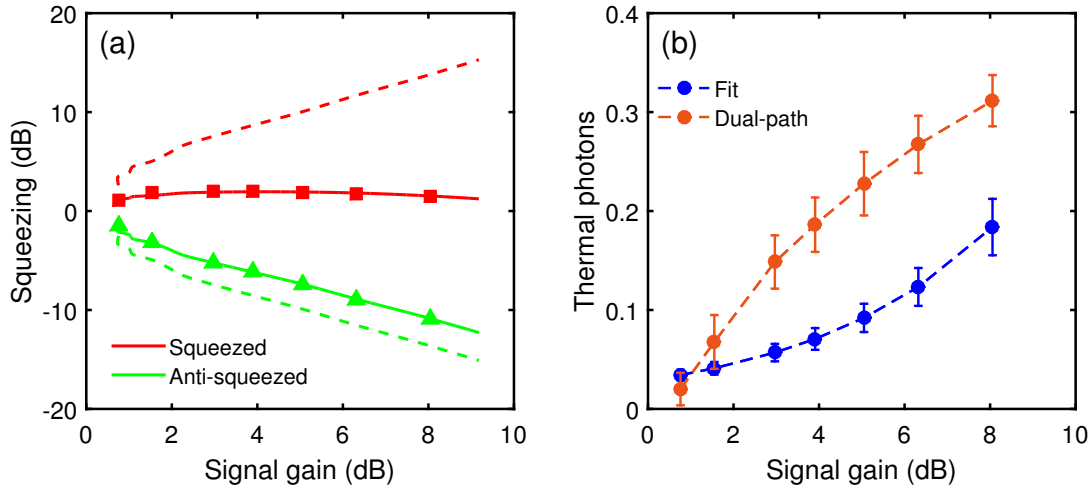


**Figure 5.7:** (a) Squeezing of the squeezed quadrature (red) and anti-squeezed quadrature (green) as a function of the signal gain at 5.594 GHz. Squares and triangles represent the experimental data. The solid lines are a fit to the data after Eq. (5.3). The dashed lines are the theoretical squeezing without any noise contributions,  $\eta = 1$ , for the extracted fitting parameters. (b) Number of thermal photons obtained from fitting (blue) and dual-path reconstruction with thermal squeezed vacuum states (orange) as a function of the signal gain. Lines are guides for the eyes. If no error bars are shown, the error is smaller than the marker size.

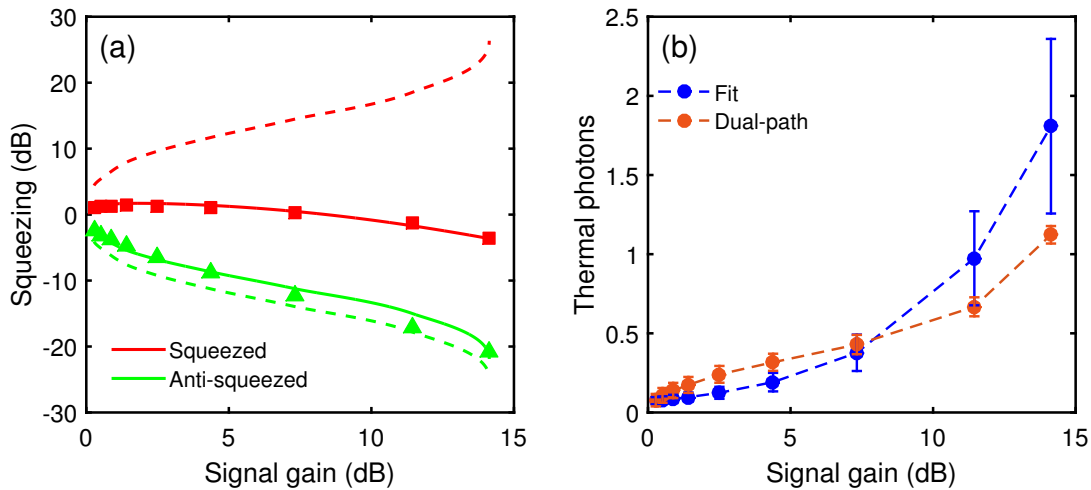


**Figure 5.8:** (a) Squeezing of the squeezed quadrature (red) and anti-squeezed quadrature (green) as a function of the signal gain at 5.51 GHz. Squares and triangles represent the experimental data. The solid lines are a fit to the data after Eq. (5.3). The dashed lines are the theoretical squeezing without any noise contributions,  $\eta = 1$ , for the extracted fitting parameters. (b) Number of thermal photons obtained from fitting (blue) and dual-path reconstruction with thermal squeezed vacuum states (orange) as a function of the signal gain. Lines are guides for the eyes. If no error bars are shown, the error is smaller than the marker size.

Working point	$\tilde{n}_{\text{th}}$	$\epsilon_a$ (kV <sup>-1</sup> )	$\Delta A$ (V)
5.594 GHz	$0.029 \pm 0.005$	$0.220 \pm 0.008$	$0.104 \pm 0.075$
5.51 GHz	$0.070 \pm 0.021$	$0.559 \pm 0.047$	$0.318 \pm 0.110$

**Table 5.1:** Fitting results of the squeezing level with red sideband contribution for the two working points. Uncertainties are from 95% confidence bounds of fitting.

We note, that the fit is performed simultaneously for the squeezed and the anti-squeezed quadratures<sup>2</sup>.

At 5.594 GHz, the fit follows both the squeezed as well as the anti-squeezed quadrature very well (see Fig. 5.7 (a)). The effect of thermal photons in the red sideband on the variance of the anti-squeezed quadrature is, in the limit of large anti-squeezing and small number of thermal photons, a reduction by 3 dB as compared to the theory curve neglecting the red sideband. For larger contributions of thermal photons the difference between the curves is smaller than 3 dB. Therefore, the general trend of the anti-squeezed quadrature should be similar with and without a red sideband, which is confirmed by our measurements (see green triangles and dashed green line in Fig. 5.7 (a)). The total reconstructed squeezing of the squeezed quadrature, on the other hand, depends strongly on the red sideband contribution. Even with infinite squeezing at the JPA and a vacuum state added through the red sideband, one can achieve a maximum squeezing of 3 dB in the combined signal. If more than half a thermal photon is added through the red sideband, no squeezing below the vacuum can be measured any more. Therefore, a red sideband contribution will drastically reduce the reconstructed squeezing level of the hybrid ring input signal.

In Fig. 5.7 (b), the obtained number of thermal photons  $\tilde{n}_{\text{th}}G_p(A_{\text{pump}})$  (blue circles) from fitting Eq. (5.3) are shown for the respective signal gains. Additionally, the number of thermal photons (orange circles) from the dual-path reconstruction under the assumption of thermal squeezed vacuum states, as discussed previously, are shown for comparison. The extracted numbers of thermal photons from both approaches deviate from one another, but show an increase for increasing signal gain.

For 5.51 GHz, the squeezed quadrature is fitted reasonably well but the anti-squeezed quadrature slightly deviates from the fit (see Fig. 5.8 (a)). We note, that the signal gain range for both plots is different. The conversion factor  $\epsilon_a$  from pump amplitude to frequency modulation  $\delta$  for this frequency is bigger than for the working point at 5.594 GHz. This is expected, since the slope of the resonant frequency as a function of the external flux is smaller at 5.594 GHz. This translated to a smaller frequency modulation  $\delta$  for the same pump amplitudes. Again, the number of thermal photons from fitting as well as the dual-path reconstruction are depicted in Fig. 5.8 (b). Similarly to the other

<sup>2</sup>The total variance of the anti-squeezed quadrature  $(\Delta q_{\text{anti-sq}})^2$  is given by Eq. (5.3) where  $G_d^{\text{min}}$  is replaced by the maximal signal gain of the JPA  $G_d^{\text{max}}$  (see Eq. (2.104)).

working point, they deviate from one another, but at the same signal gains show a similar behavior.

At the respective signal gains with the highest measured squeezing levels, we obtain 7.55 dB and 7.95 dB of squeezing for the working points at 5.594 GHz and 5.51 GHz, respectively, if the red sideband contribution is neglected. These values give an absolute upper bound to the possible squeezing level at the respective signal gains, since they do not include noise contributions from the detection setup or connection losses at the JPA sample.

### 5.3 Displacement of quantum states

In the following, we are interested in the displacement of quantum states, particularly in displaced vacuum states and displaced squeezed states. To this end a vacuum state is incident to the JPA input and a coherent signal to the coupled port of the directional coupler with high transmissivity is applied. An incoming signal to the directional coupler is then displaced by a certain amount of photons. If no pump tone is applied to the JPA, a vacuum state is incident to the directional coupler, which will be displaced and, thus, results in a coherent state at the input to the hybrid ring. When a pump tone is applied to the JPA, one obtains a displaced squeezed state at the input to the hybrid ring. The cryogenic and the room temperature setup schemes are shown in Fig. 3.2 and Fig. 3.6, respectively, where JPA Q200new is used for the measurements.

We now turn the pump to the JPA on and also apply a displacement signal to the coupled port of the directional coupler. By accounting for losses of the microwave input line, the displacement power at the directional coupler input is estimated to  $-126$  dBm. By changing the phase  $\theta$  of the displacement signal, one can adjust the angle of displacement as seen in Fig. 5.9. The working point is at 5.51 GHz and the phase stabilization protocol with 100 measurements per displacement angle is applied, where the squeezing angle as well as the displacement angle are stabilized. In Fig. 5.9 (a), an overlay of the reconstructed Wigner functions for displacement angles of  $\theta = 0^\circ, 45^\circ, 90^\circ$  and  $135^\circ$  and a squeezing angle of  $\gamma = 45^\circ$  is shown. The corresponding  $1/e$  contours of the Wigner functions and vacuum states with the respective displacement angles are depicted in Fig. 5.9 (b). We observe, that the target values of squeezing and displacement angles coincide very well with the mean values obtained from averaging 100 measurements. However, the standard deviation for both angles is of the order of degrees (see Fig. 5.9 (c,d)) and, thus, similar to the squeezed vacuum states (compare to Fig. 5.1). The standard deviation of the anti-squeezed quadrature angle is larger than the one of the displacement angle, because we displace the state by approximately 45 photons and therefore obtain a rather strong coherent signal. The phase of such a strong coherent signal can be measured more precisely than the phase of the anti-squeezed quadrature. In theory, one expects a constant squeezing level for different displacement angles. In contrast, we observe a non-constant dependence of the

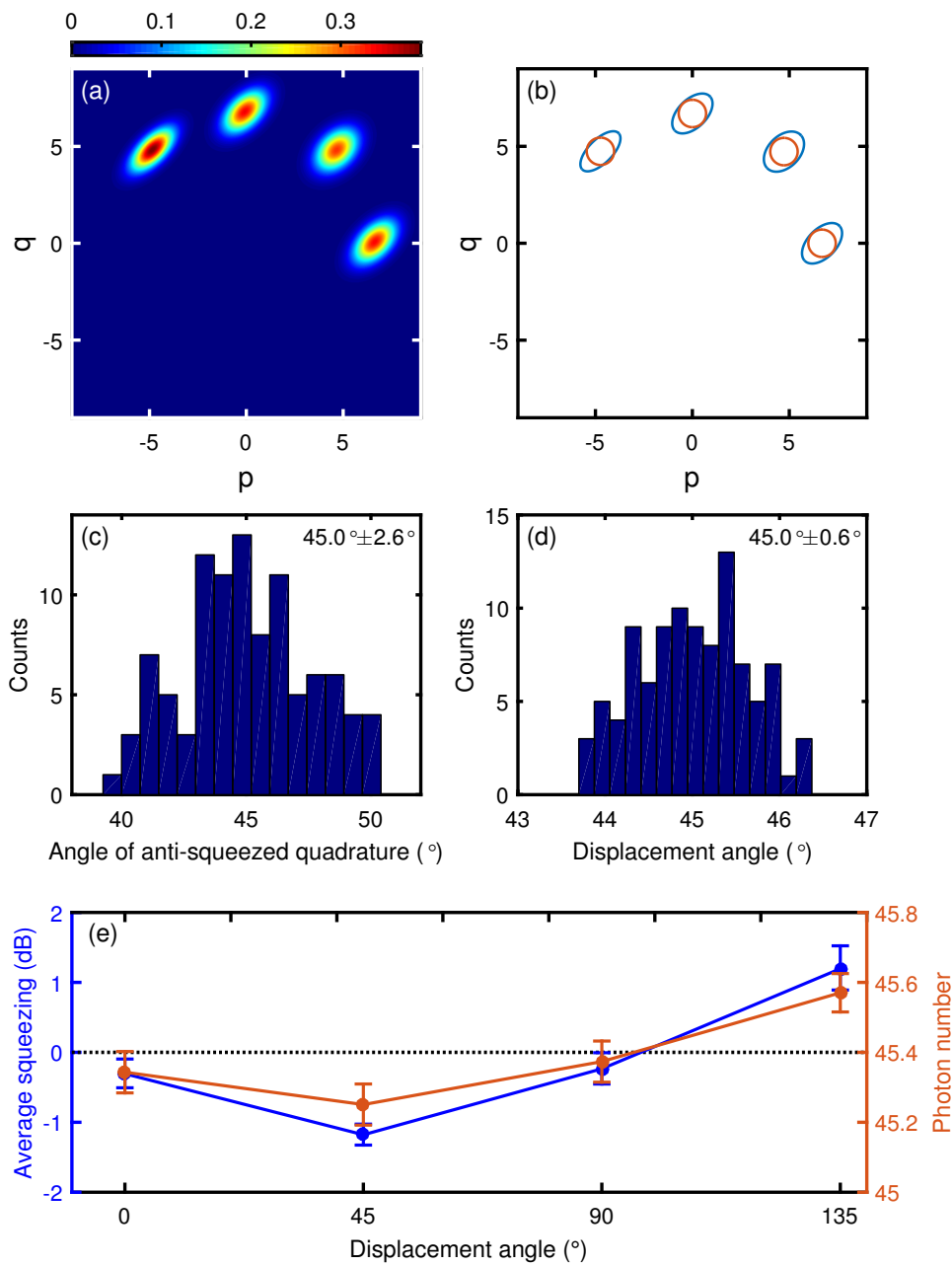


**Figure 5.9:** (a) Wigner functions for four different displacement angles of  $\theta = 0^\circ, 45^\circ, 90^\circ, 135^\circ$  with anti-squeezed angle  $\gamma = 45^\circ$ . The individual Wigner functions are overlaid to produce the figure. The estimated displacement power at the directional coupler input is  $-126$  dBm. (b)  $1/e$  contours for the respective displacement angles of the vacuum state (orange) and the squeezed displaced state (blue). Histograms of (c) the angle of anti-squeezed quadrature and (d) displacement angle for a target displacement angle  $\theta = 45^\circ$ . (e) Average squeezing (blue) and photon number (orange) as a function of the displacement angle  $\theta$  for a working point at  $5.51$  GHz. The negative squeezing level, meaning squeezing above vacuum, for some displacement angles is caused by phase fluctuations or a misestimation of the PNCF factors as described in Fig. 5.10 for simulated phase fluctuations. For each displacement angle, 100 measurements with the phase stabilization protocol are performed, where each measurement is averaged over  $5.6 \times 10^8$  raw data samples. The lines are guides for the eyes. The error bars are of statistical nature. The JPA is stabilized to  $40$  mK.

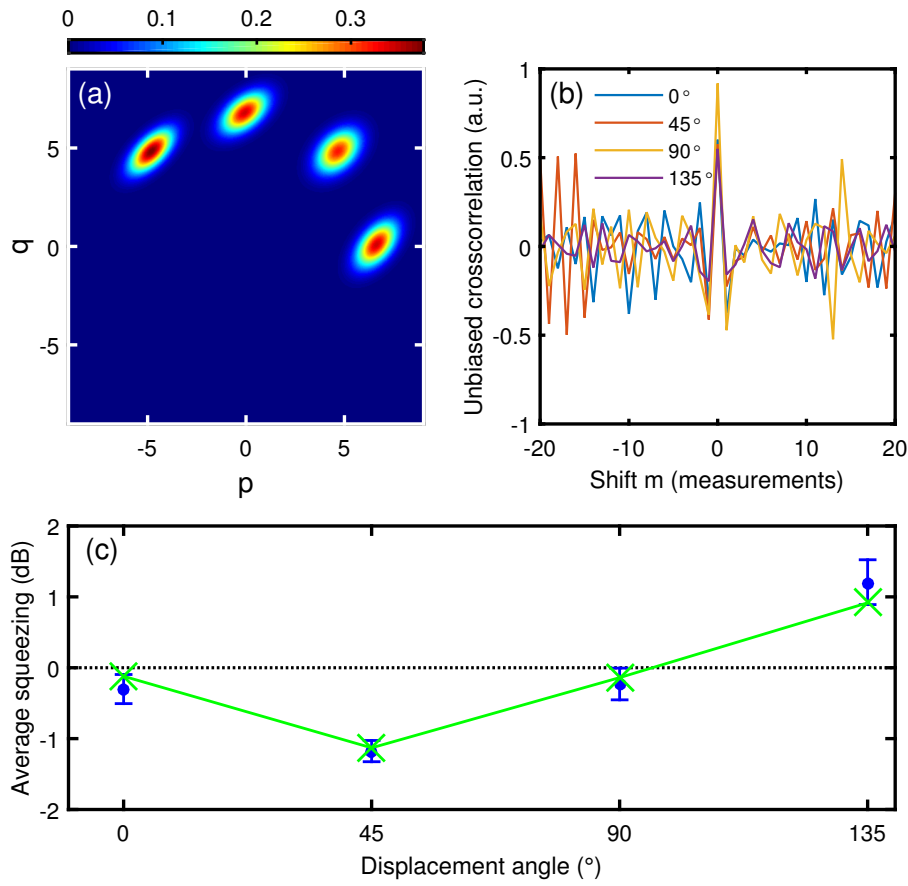


**Figure 5.10:** (a) Wigner functions of simulated signals for displaced squeezed vacuum states with  $r = 0.48$ ,  $\gamma = 45^\circ$ ,  $n_{\text{th}} = 0.21$  photons and displacement of 44.8 photons at displacement angles of  $\theta = 0^\circ, 45^\circ, 90^\circ$  and  $135^\circ$ . Both angles fluctuate with a standard deviation of  $3.0^\circ$  in the simulation. The individual Wigner functions are overlaid to produce the figure. (b) Unbiased cross-correlation between  $\theta$  and  $\gamma$  for different lags of the 100 measurements. (c) Average squeezing from experiments for a working point at 5.51 GHz (blue) and simulated squeezing (green) versus displacement angle  $\theta$ . The line is a guide for the eyes. The error bars are of statistical nature. The JPA is stabilized to 40 mK.

squeezing level on the displacement angle  $\theta$ . The cumulants are not vanishing for these measurements, indicating that the states are non-Gaussian. If the difference between the angle of the anti-squeezed quadrature  $\gamma$  and the displacement angle  $\theta$  is  $0^\circ$ , we observe the lowest squeezing levels. If the difference is  $90^\circ$ , the highest squeezing levels are observed (see Fig. 5.9 (e)). In between, the squeezing level has intermediate values. The photon number also follows this trend.

In order to describe the behavior of the squeezing level for different displacement angles, one can simulate a signal with phase fluctuations of the displacement angle as well as the squeezing angle with a standard deviation of  $3.0^\circ$  (for details see Sec. 5.4.2). Wigner functions as shown in Fig. 5.10 (a) can be reconstructed from the simulated signals. The reconstructed Wigner functions are calculated for displaced squeezed vacuum

states with  $r = 0.48$ ,  $\gamma = 45^\circ$ ,  $n_{\text{th}} = 0.21$  photons and a displacement of 44.8 photons at displacement angles of  $\theta = 0^\circ, 45^\circ, 90^\circ$  and  $135^\circ$ . For each  $\theta$ , 10000 averages are performed. The measured squeezing level and the Wigner functions are reproduced quite well by the simulation (see Fig. 5.10 (a,c)). We note, that the values for  $r$  and the number of thermal photons  $n_{\text{th}}$  are not unique, similar Wigner functions and squeezing levels can be simulated with different values.

In Fig. 5.10 (b), the unbiased cross-correlation  $\langle \theta_i \cdot \gamma_j \rangle$  between  $\theta$  and  $\gamma$  of the four measured displacement angles is shown. The cross-correlation is calculated in a way so that  $i - j = m$  is fulfilled and, thus,  $m$  defines a shift between  $\theta_i$  and  $\gamma_j$  of the 100 individual measurements from the phase stabilization protocol. For  $m = 0$ , meaning that the 100 individual measurements of  $\theta$  and  $\gamma$  are not shifted with respect to each other, the cross-correlation shows a distinct peak for all four displacement angles. If one calculates the cross-correlation between shifted  $\theta$  and  $\gamma$ , lower values are obtained. This indicates, that the phase fluctuations are correlated. Reasons for such correlated phase fluctuations could be trigger issues with the Acqiris card or an unstable phase of the local oscillator signal.

## 5.4 Squeezing versus displacement

### 5.4.1 Experimental results

After investigating squeezed states for different displacement angles  $\theta$ , we are now interested in displacing squeezed states by a different amount of photons. Similar to the previous section, we turn on the pump tone to the JPA, but now the power of the coherent signal incident to the coupled port of the directional coupler is changed. The working point is at 5.537 GHz. The setup is as in Fig. 3.6 but no JS3 amplifiers and IQ-mixers (Marki, IQ4509LXP) instead of single ended mixers are used. The phase stabilization protocol with 35 measurements per displacement power is applied, where the squeezing angle as well as the displacement angle are stabilized. We also displace vacuum states<sup>3</sup>, where the JPA pump is off, with 10 measurements each. Each measurement is averaged over  $5.6 \times 10^8$  raw data samples.

First, one can look at the number of photons by which an incident state to the directional coupler is displaced when the displacement power at the microwave source is changed. For that, we take the reconstructed first moments  $\langle \hat{a} \rangle = \alpha$ , which are equal to the complex amplitude  $\alpha$ . Then,  $|\alpha|^2$  gives the number of photons by which the incident state is displaced. Fig. 5.11 shows the resulting displacement photons as a function of the displacement power at the microwave source. As expected, a linear fit describes the

---

<sup>3</sup>A displaced vacuum state is nothing else than a coherent state, since a coherent state is produced by displacing the vacuum. However, we use the notation displaced vacuum to emphasize that we use the directional coupler as displacer.

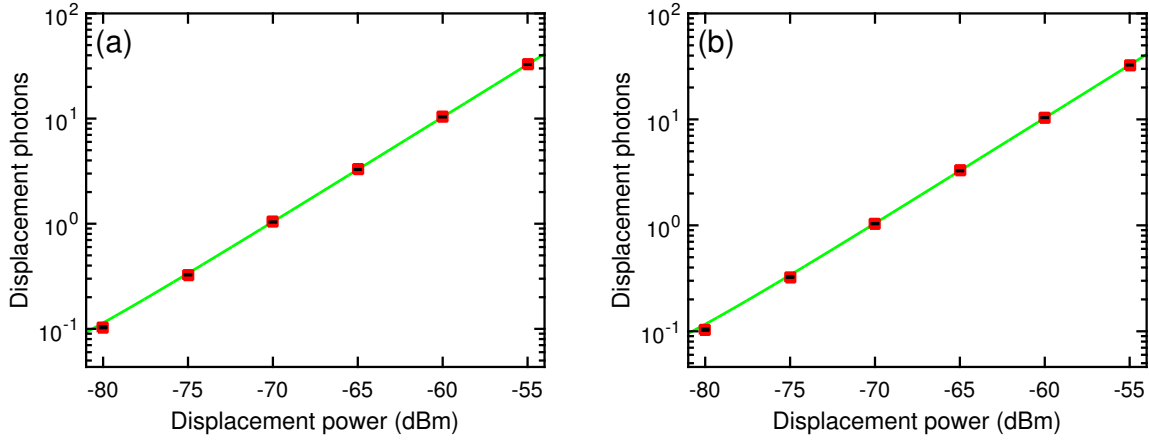


**Figure 5.11:** Number of photons by which (a) a squeezed state or (b) a vacuum state is displaced in phase space as a function of the displacement power at the microwave source. Red squares are data points and green lines are linear fits to the data. For displaced squeezed states 35 and for displaced vacuum states 10 phase stabilization steps are performed, where each measurement is averaged over  $5.6 \times 10^8$  raw data samples. The error bars (black) are of statistical nature. The JPA is stabilized at 40 mK.

data very well for both displaced squeezed (Fig. 5.11 (a)) and displaced vacuum states (Fig. 5.11 (b)). Such fits can be used as a calibration for further experiments where the directional coupler is used for linear transformations in e.g. quantum information protocols.

The reconstructed Wigner functions of the same datasets are depicted in Fig. 5.12 (a,b). The squeezing angle is  $\gamma = 45^\circ$  and the displacement angle is  $\theta = 135^\circ$ . For increasing displacement, the Wigner functions deform and get more smeared out in the direction perpendicular to the displacement direction. We emphasize, that this happens for displaced squeezed states as well as displaced vacuum states. Furthermore, we observed that the deformation is always perpendicular to the displacement direction. Additionally, the cumulants are small or vanish for all displacement powers, except for the highest one with 32.6 photons of displacement. Here a slight increase of the cumulants is observed. We refer the reader to the next section for a more detailed analysis of these issues.

In Fig. 5.12 (c,b) the extracted squeezing levels of displaced squeezed states and displaced vacuum states averaged over the phase stabilization steps are shown, respectively. As expected, the squeezing level of the displaced squeezed state is nearly constant as a function of the displacement up to 32.6 photons. The squeezing levels of the displaced vacuum states show a slight decrease with increasing displacement, which is attributed to the mentioned shape change of the Wigner function. As predicted in theory [29], our results show that a directional coupler with high transmissivity can be used to implement a displacement operation for classical and non-classical input states in the microwave regime.

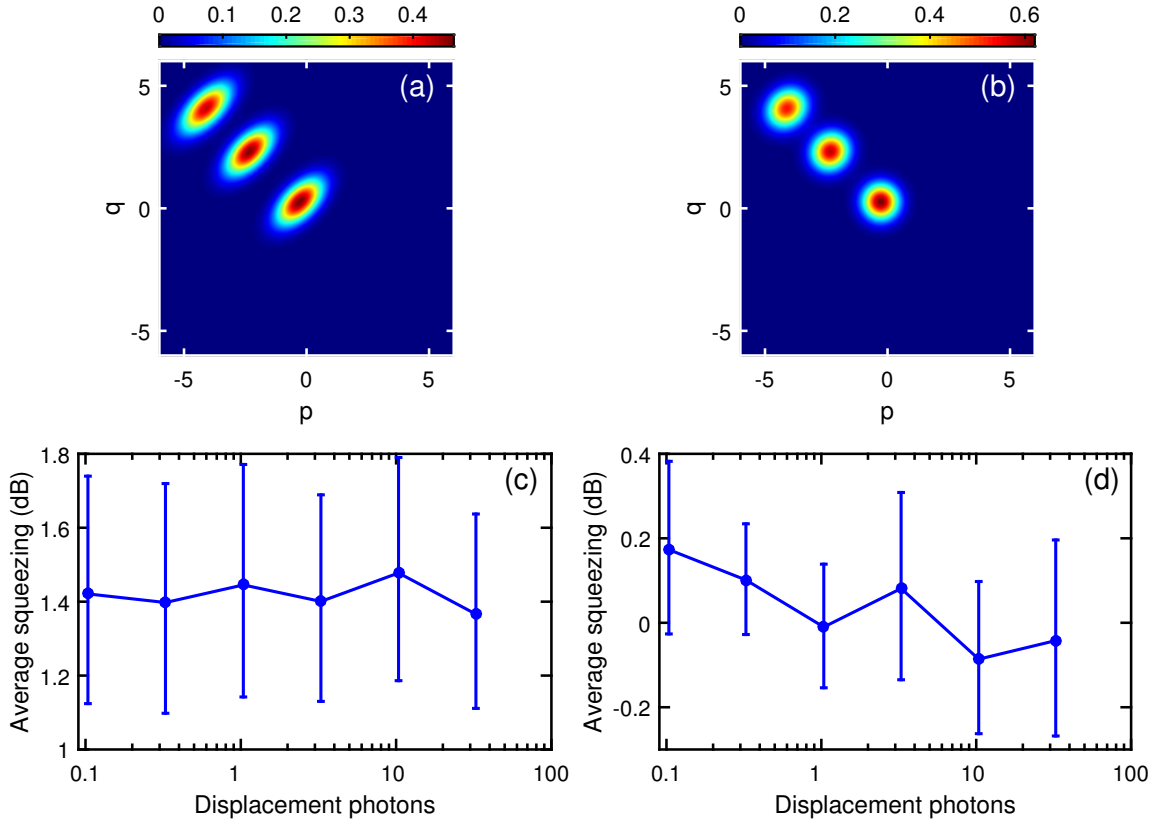


**Figure 5.12:** (a) Displaced squeezed states for different displacements with  $\gamma = 45^\circ$  and  $\theta = 135^\circ$ . (b) Displaced vacuum states or coherent states with different displacements with  $\theta = 135^\circ$ . For (a,b) the number of displacement photons is 0.1, 10.4 and 32.6. For displaced squeezed states 35 and for displaced vacuum states 10 phase stabilization steps are performed, where each measurement is averaged over  $5.6 \times 10^8$  raw data samples. The working point is at 5.537 GHz. (c,d) Squeezing level of displaced squeezed state and displaced vacuum as a function of displacement, respectively. The lines are guides for the eyes. The error bars are of statistical nature. The JPA is stabilized at 40 mK.

Furthermore, one can investigate quantum entanglement between the output states of the hybrid ring. It was shown previously, that by sending a squeezed state into a beam splitter, the output states of the beam splitter exhibit path entanglement [19, 49]. By using the beam splitter relations, one can calculate the output states  $\hat{c}_{1,2}$  of the beam splitter from the reconstructed signal moments

$$\hat{c}_1 = \frac{1}{\sqrt{2}}(\hat{a} + \hat{v}), \quad \hat{c}_2 = \frac{1}{\sqrt{2}}(-\hat{a} + \hat{v}), \quad (5.5)$$

where  $\hat{a}$  is the bosonic annihilation operator of the signal and  $\hat{v}$  bosonic annihilation operator of a reference mode, which is a weak thermal state with a temperature of approximately 30 mK. From the output states, the negativity kernel  $\mathcal{N}$  can be calculated. As described in Appendix C, the negativity kernel  $\mathcal{N}$  is an entanglement witness for an

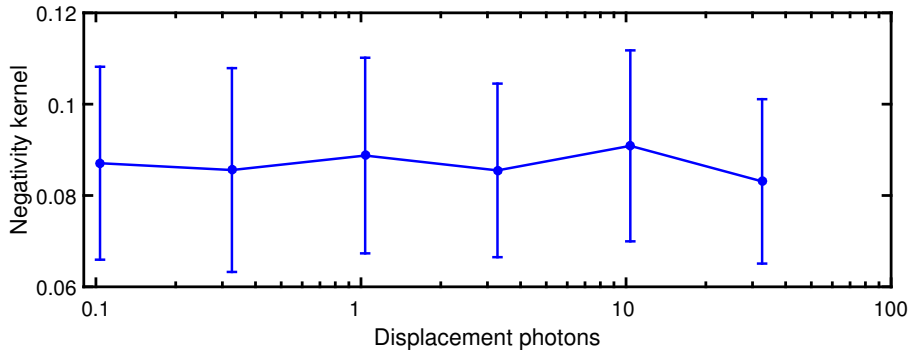


**Figure 5.13:** Negativity kernel of the evaluated outputs of the hybrid ring as a function of displacement. The negativity kernel is calculated with the hybrid ring input-output relations for an incident displaced squeezed state. The reconstructed moments used for calculation are the same as for Fig. 5.12. The lines are guides for the eyes. The error bars are of a statistical nature.

arbitrary bi-partite system. Fig. 5.13 shows the calculated negativity kernel for the data shown in Fig. 5.12 (a). The kernel is positive and, thus, indicates the path entanglement between the output paths of the hybrid ring. Furthermore, it is nearly constant up to a displacement of 33 photons of the displaced squeezed state, which is the input state to the hybrid ring. This means, the quantum mechanical correlations between the output states of a beam splitter are not destroyed when a classical coherent signal, that is the displacement signal, is added to a quantum state, that is the squeezed state, before sending it to a beam splitter. However, in comparison with results by Menzel *et al.* [19] the obtained values of the negativity kernel are smaller. This is explained by a substantially lower squeezing level of the states in the presented experiments resulting in smaller values of the negativity kernel.

### 5.4.2 Effect of phase fluctuations and the PNCF

As discussed in the previous sections, the observed Wigner functions reconstructed from the experimental data differ from the theoretical expectations, especially if the states are displaced by a large amount of photons. In detail, we observe a change in the squeezing level for different displacement angles  $\theta$ , as well as broadening of the reconstructed Wigner functions perpendicular to the displacement direction. The latter was observed for displaced squeezed and displaced vacuum states. We attribute the observed behavior to the presence of phase fluctuations of the displacement angle  $\theta$  and the squeezing angle  $\gamma$  as well as to misestimations in the photon number conversion factors (PNCFs).

The phase fluctuations most probably arise from trigger issues of the Acqiris card or phase instabilities of the local oscillator signal at the mixers. A modified version of the measurement program showed standard deviations of the phase, at which the Acqiris card triggers, of up to  $3.6^\circ$ . Trigger issues would also explain the correlation between  $\theta$  and  $\gamma$  (see Fig. 5.10 (b)). The misestimation in the PNCF is caused by an imperfect

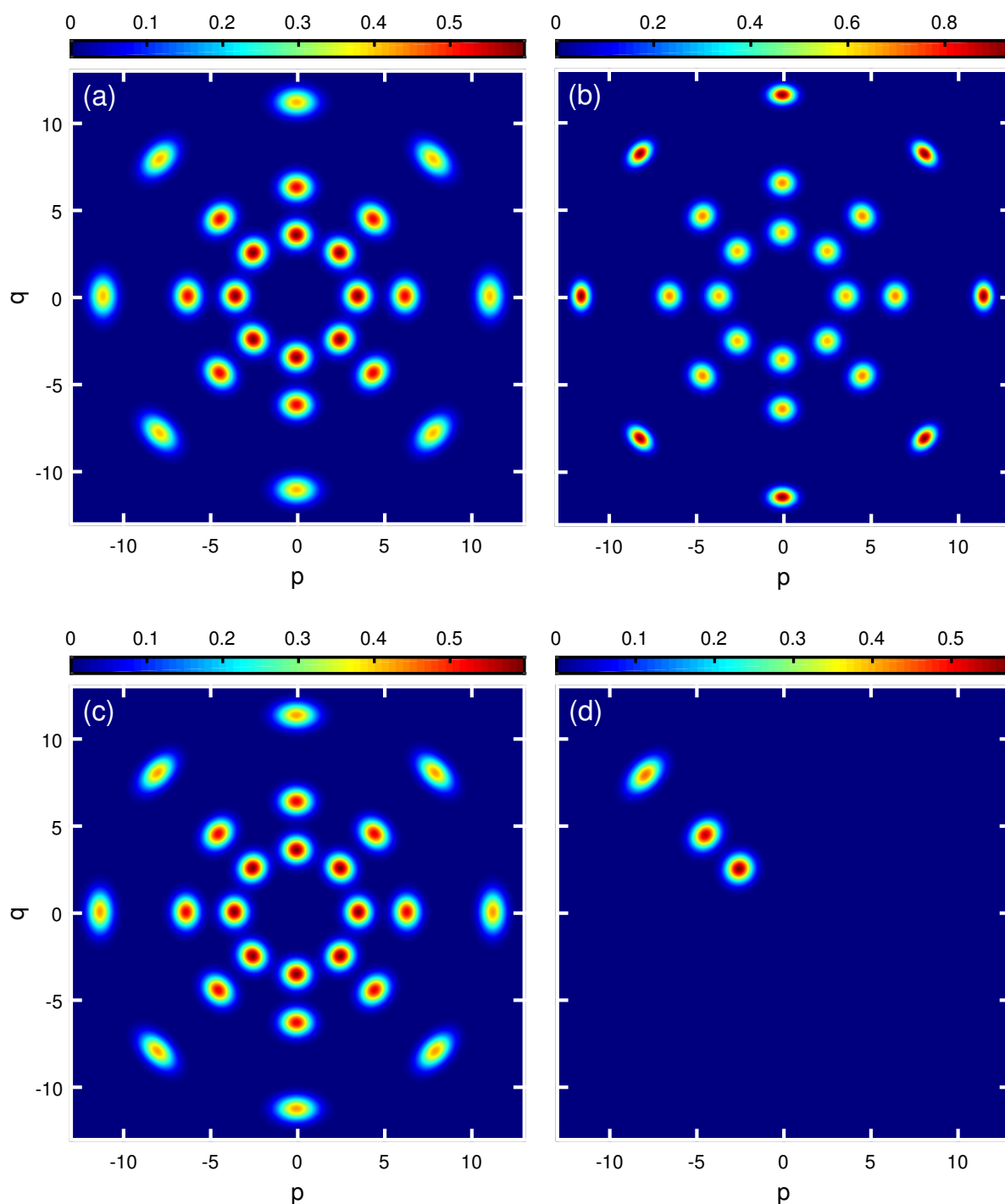


**Figure 5.14:** Wigner functions of simulated signals for displaced vacuum states with (a) only phase fluctuations, (b) only a misestimation of the PNCFs in one chain by a factor of 0.88, (c) both phase fluctuations and a misestimation of the PNCFs in one chain by a factor of 0.94 as well as (d) experimentally obtained Wigner functions for a displacement of 12, 39 and 124 photons. The displacement signal is at 5.932 GHz. 100 phase stabilization steps are performed, where each measurement is averaged over  $8.0 \times 10^7$  raw data samples. The JPA temperature is stabilized at 50.5 mK.

Planck spectroscopy we perform to calibrate the detection paths, due to limited detection efficiency of the Acqiris card and small instabilities in the amplification chains. The extracted PNCFs from fitting have 95% confidence bounds with a deviation of 2 – 3% of the PNCF value. As discussed in the following, a misestimation on this order causes deformations of the Wigner function for large displacements with large photon numbers.

In Fig. 5.14 (a-c) we show Wigner functions of simulated signals for displaced vacuum states with various displacement angles  $\theta$  and displacement amplitude of 12, 39 and 124 photons. The individual Wigner functions are overlaid to produce the figure. In Fig. 5.14 (a), only phase fluctuations with a standard deviation of  $3.0^\circ$  of the displacement angle  $\theta$  are considered in the simulation. For the simulation, the in-phase and out-of-phase quadratures for both amplification chains are simulated and reconstructed with the dual-path method in the same way as for a real measurement. Without phase fluctuations of the displacement angle, the simulations yield displaced vacuum states, as expected from theory. If one includes phase fluctuations in the displacement angle, the simulation reproduces the broadening perpendicular to the displacement direction. With increasing displacement, the maxima of the Wigner functions becomes shallower. Furthermore, with increasing displacement, both quadrature variances increase above the vacuum level. However, the quadrature variance perpendicular to the displacement direction is increased by a much larger amount than the parallel one (see Tab. 5.2).

In Fig. 5.14 (b), only a misestimation of the PNCF of one chain by a factor of 0.88 is simulated. For that the amplitude of the simulated displaced vacuum state of one chain is multiplied by a factor of 0.88. The smearing is similar as for (a), but now the maxima of the Wigner functions increase with increasing displacement. Also the squeezing level of the displaced vacuum state depends strongly on the displacement. For large displacements the states show higher levels of squeezing.

If both, phase fluctuations with a standard deviation of  $3.0^\circ$  and a PNCF misestimation of one chain by 0.94, are taken into account simultaneously, one obtains the Wigner functions shown in Fig. 5.14 (c). Now the maxima of the Wigner functions decrease with increasing displacement, but the squeezing level increases with increasing displacement. The simulation in Fig. 5.14 (c) describes the measured displaced vacuum states shown in Fig. 5.14 (d) with respect to the maxima of the Wigner functions as well as the dependence of the squeezing on the displacement. For the measurement data, the displacement signal is at 5.932 GHz. 100 phase stabilization steps are performed, where each measurement is averaged over  $8.0 \times 10^7$  raw data samples.

In Fig. 5.15 (a) and (b), we show simulations of displaced squeezed states for  $\gamma = 45^\circ$  and  $\gamma = 135^\circ$ , respectively, for various displacement angles  $\theta$  and displacements of 39 and 124 photons. Only fluctuations of the displacement angle  $\theta$  and the angle of the anti-squeezed quadrature  $\gamma$  with a standard deviation of  $3.0^\circ$  for both angles are taken into account. We observe, that the Wigner functions change their shape for different displacement angles. Simulated squeezing levels are depicted in Fig. 5.15 (c) and (d) for

	Photons $n$			Fig 5.14
	$n = 12$	$n = 39$	$n = 124$	
Phase	-0.002	-0.004	-0.009	(a)
PNCF	0.238	0.807	3.353	(b)
PNCF+Phase	0.051	0.166	0.551	(c)
Experiment	$-0.02^{+0.36}_{-0.33}$	$0.13^{+0.50}_{-0.45}$	$0.60^{+0.48}_{-0.43}$	(d)

**Table 5.2:** Squeezing levels in dB for simulations shown in Fig 5.14 (a-c) and measured displaced vacuum states in Fig 5.14 (d).  $n$  denotes the amount of photons by which the vacuum is displaced.

$\gamma = 45^\circ$  and  $\gamma = 135^\circ$ , respectively. If  $\theta - \gamma$  is an uneven multiple of  $\pi/2$  the state best resembles the undisplaced squeezed state and also exhibits a nearly unchanged squeezing level for both values of  $\gamma$ . If the difference  $\theta - \gamma$  is an even multiple of  $\pi/2$ , then the effect of the phase fluctuations is the largest. The Wigner function is strongly deformed and the squeezing level changes drastically. In general, the cumulants are not vanishing for such kind of reconstructed states.

From these results, we conclude that a very precise phase control of the used microwave sources and a reliable PNCF calibration are crucial for large displacements. Both displaced vacuum states and displaced squeezed states are affected by phase fluctuations and incorrect PNCFs.

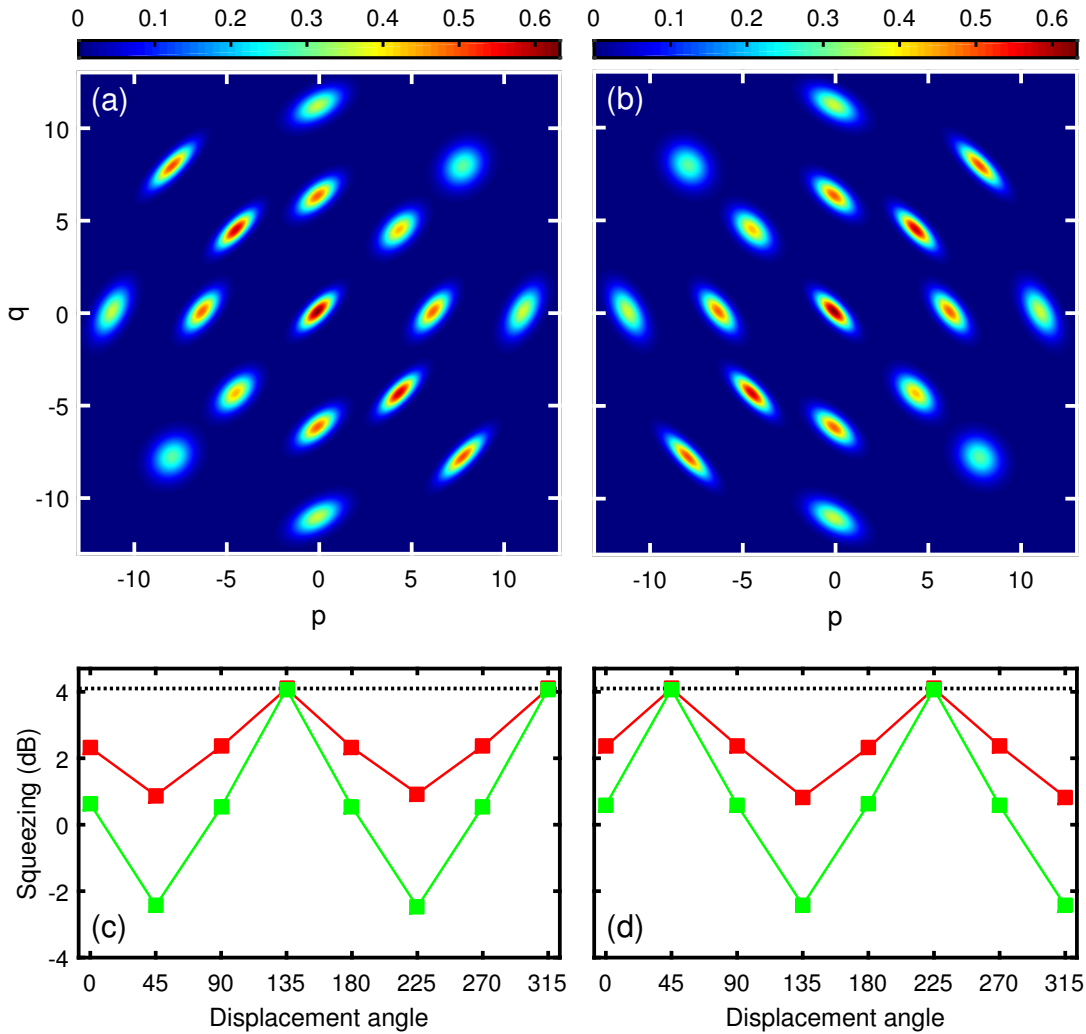


**Figure 5.15:** Wigner functions of simulated signals for displaced squeezed states with (a)  $\gamma = 45^\circ$  and (b)  $\gamma = 135^\circ$  for various displacement angles  $\theta$ . Only fluctuations of the displacement angle  $\theta$  and the angle of the anti-squeezed quadrature  $\gamma$  with a standard deviation of  $3.0^\circ$  for both angles are taken into account. The states are displaced by either 39 (red) or 124 (green) photons. (c) and (d) show the squeezing as a function of the displacement angle for  $\gamma = 45^\circ$  and  $\gamma = 135^\circ$ , respectively. The black dashed line indicates the squeezing level of the undisplaced squeezed state. The lines are guides for the eyes.

# Chapter 6

## Conclusions and outlook

In this work, flux-driven Josephson Parametric Amplifiers (JPAs) are used for the generation of squeezed light in the microwave regime. A JPA consists of a coplanar waveguide microwave resonator where the inner conductor is grounded on one side by a dc-SQUID. The flux dependent non-linear inductance of the dc-SQUID is utilized to tune the resonant frequency of the resonator. Multiple JPAs are characterized with respect to the dependence of the resonant frequency on an externally applied flux through the dc-SQUID loop. One sample shows a strong hysteretic behavior for different sweep directions of the external flux. The state of a dc-SQUID can be described by a phase-particle moving inside the two-dimensional potential of the dc-SQUID. To describe the hysteretic behavior, we developed an approach to simulate the position of the phase-particle inside this potential for a varying external flux. The thereby obtained flux dependence of the resonant frequency for both hysteretic and non-hysteretic JPAs are in good agreement with the experimental results. Additionally, the internal and external quality factors of the samples are determined.

With JPA Q200new, squeezing measurements are performed, since this sample exhibits very high internal quality factors. For that, an Acqiris card based dual-path setup with a digital IQ-demodulation is used. We investigate two different working points at frequencies of 5.51 GHz and 5.594 GHz of the JPA. For the two working points, the maximal squeezing levels  $\mathcal{S} = 1.41_{-0.60}^{+0.76}$  dB and  $\mathcal{S} = 2.00_{-0.38}^{+0.42}$  dB of squeezed vacuum states are obtained for signal gains of 1.4 dB and 3.0 dB, respectively. For higher signal gains, the squeezing level diminishes. We attribute this decrease to a contribution of an unsqueezed red sideband. The signal band, which contains the squeezed signal, is thereby diluted by a weak thermal state and the overall squeezing level evaluated by the dual-path reconstruction diminishes drastically. We developed a simple model to account for the unsqueezed red sideband contribution to the squeezing level and find good agreement with the measured data. After correction of the red sideband, we obtain calculated upper bounds for the squeezing levels at the two different working points of the JPA of 7.95 dB and 7.55 dB. This unwanted red sideband is a natural limitation of a 2-channel setup. However, in the future, it should be possible to filter out this sideband by using specific image reject mixers instead of usual harmonic double-balanced mixers.

Furthermore, a highly asymmetric directional coupler is used to displace squeezed vacuum states by biasing the coupled port with a strong coherent signal. We are able to control the angle and amount of displacement by changing the phase and power of the displacement signal, respectively. Thus, we are able to confirm that the directional coupler applies a displacement operation to an incident quantum state. Up to 33 photons of displacement, the squeezing level is nearly constant, showing that mixing the squeezed state with a classical coherent state, does not destroy the quantum correlations in the signal. However, for large displacements, the reconstructed Wigner functions and squeezing levels of squeezed as well as coherent states deviate from the expected behavior. The source of these effects, are misestimations of the photon number conversion factors (PNCFs) of the order of several percent and phase fluctuations, most probably caused by trigger issues of the Acqiris card or phase instabilities of the local oscillator signal.

Currently, the focus lies on eliminating the contribution of the red sideband, since the latter is the limiting factor in current measurements, regarding the squeezing level. On the one hand, a sharp analog filter at RF-frequencies could filter the red sideband, but would also limit the dual-path receiver to one frequency. A FPGA-card based setup, where analog IQ-mixers are used to extract the quadratures of the microwave signal, is a more robust alternative. Here, one can filter the red sideband during digital down-conversion of the IF-frequency. Furthermore, the FPGA allows for real-time data processing, increasing the detection efficiency drastically and decreasing the measurement time. This also contributes to a more precise determination of the PNCF factors, making higher displacements of squeezed states feasible. Next, phase instabilities need to be addressed, since for high squeezing levels, very high phase control of the squeezing angle is required. Also, connection and cable losses between the JPA and the input to the hybrid ring are not compensated by the dual-path state reconstruction, so keeping these losses at a minimum is of crucial importance. Furthermore, before the HEMT amplifiers, one can use JPAs as low-noise pre-amplifiers to significantly enhance the detection efficiency.

With the current setup, the commutation relation between the squeezing operator  $\hat{S}(\xi)$  and the displacement operator  $\hat{D}(\alpha)$  can be experimentally investigated. By either applying a coherent signal to the JPA and no displacement signal at the directional coupler or first squeezing the vacuum with the JPA and subsequent displacement by the directional coupler, one obtains final states of the form  $\hat{S}(\xi)\hat{D}(\alpha)|0\rangle$  or  $\hat{D}(\alpha)\hat{S}(\xi)|0\rangle$ , respectively. By comparing the resulting states it is possible to experimentally verify the commutation relations between the operators.

With the displacement operation and the entanglement between the output chains, two main building blocks for quantum teleportation with continuous variables in the microwave regime are available.

# Appendix A

## Simulation of dc-SQUID potential

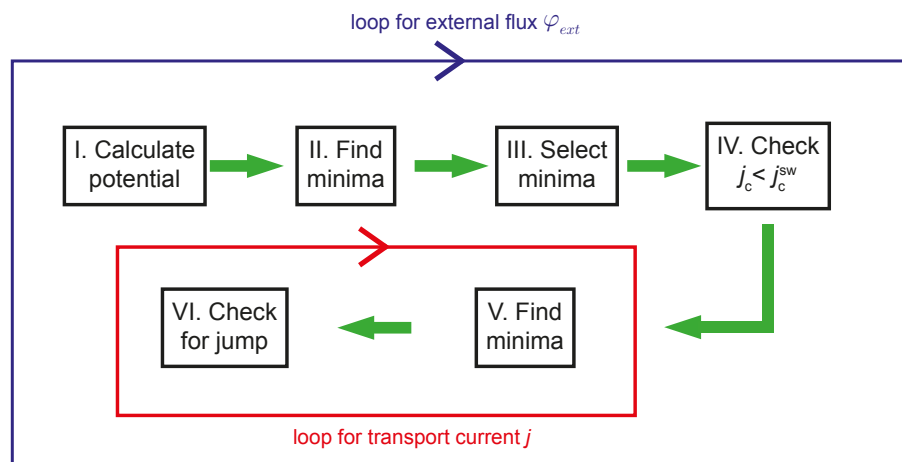


**Figure A.1:** Sketch for simulation of dc-SQUID potential and determination of normalized critical current  $j_c(\varphi_{ext})$ .

Fig. A.1 depicts a sketch describing the simulation of dc-SQUID potential and determination of normalized critical current  $j_c(\varphi_{ext})$ . The numerical simulations are implemented in MATLAB. An outer loop sweeps the external flux  $\varphi_{ext}$  for increasing and decreasing sweep directions.

(I.): For every loop iteration, the dc-SQUID potential for the present external flux is calculated after Eq. (4.2).

(II.): All potential minima around a certain start point are found with *fmincon* in combination with the *MultiStart* class. In order to find the correct local minima, the function is supplied with the gradient and the hessian of the potential, which also decreases the calculation time. In the first iteration, the start point is manually chosen, whereas for the following iterations, the starting point is determined by the position of the phase particle in the last iteration.

(III.): From the obtained local minima, the closest one to the starting point and thereby to the position of the phase particle in the previous iteration, is chosen as new position of the phase particle. Here, a new or the old minimum can be chosen.

(IV.): If the normalized critical current  $j_c$  for the last iteration is smaller than the specified switching current  $j_c^{\text{sw}}$ , then the previously selected minimum is discarded and the next closest one is selected. This procedure induces the preliminary switching of local minima even though the present minimum of the phase particle did not vanish.

(V.): Now a sub-loop is started in which the normalized critical current  $j_c$  is determined. For that one sweeps the transport current through the dc-SQUID and again finds the local minima around the selected minimum, acting as start point for the algorithm.

(VI.): For every transport current, one checks how far the closest found local minimum deviates from the start point. If the distance is larger than a given threshold, one interprets this as jump, the sweep is stopped and the latest transport current is saved as  $j_c$  for this particular external flux  $\varphi_{\text{ext}}$ . One can easily verify, that for every  $\beta_L$  the jump is above a certain threshold value. However, in numerical simulations too low thresholds produce false-positive jumps due to the finite transport current sweep step, since different transport currents move the local minima of the potential slightly.

Then the next loop iteration of the outer loop is started, beginning at (I.) again. With that procedure one finds the normalized critical current  $j_c(\varphi_{\text{ext}})$  depending on the external flux  $\varphi_{\text{ext}}$ . The obtained dependencies are different depending on whether  $\varphi_{\text{ext}}$  is increased or decreased in the outer loop.

# Appendix B

## Cumulants and Gaussianity

The reconstruction of the Wigner function after Eq. (2.13) assumes Gaussian states. We use cumulants  $\langle\langle(\hat{a}^\dagger)^m \hat{a}^n\rangle\rangle$  as a measure for the Gaussianity of the reconstructed states. The signal moments  $\langle(\hat{a}^\dagger)^m \hat{a}^n\rangle$  and the cumulants can be used equivalently to describe a probability distribution. The cumulants can be calculated from the density matrix  $\rho$  of a quantum state [73]

$$\langle\langle(\hat{a}^\dagger)^m \hat{a}^n\rangle\rangle \equiv \frac{\partial^m}{\partial(ix)^m} \frac{\partial^n}{\partial(iy)^n} \left[ \frac{xy}{2} + \ln \text{Tr} \left( e^{(ix\hat{a}^\dagger + iy\hat{a})} \rho \right) \right] \Big|_{x,y=0}, \quad (\text{B.1})$$

where  $\hat{a}^\dagger$  and  $\hat{a}$  are the creation and annihilation operators, respectively. However, an expression of the cumulants in terms of the signal moments is more convenient [48, 74]

$$\langle\langle(\hat{a}^\dagger)^m \hat{a}^n\rangle\rangle \equiv \frac{\partial^m}{\partial x^m} \frac{\partial^n}{\partial y^n} \sum_{k,l} \frac{\langle(\hat{a}^\dagger)^k \hat{a}^l\rangle x^k y^l}{k!l!} \Big|_{x,y=0}. \quad (\text{B.2})$$

For Gaussian states only a finite number of cumulants are non-zero. In particular, only cumulants with order  $m + n \leq 2$  are non-zero and higher orders vanish. In our experiments we calculate the cumulants up to 4<sup>th</sup> order from the signal moments  $\langle(\hat{a}^\dagger)^m \hat{a}^n\rangle$  with  $m + n \leq 4$  in order to check the consistency with Gaussian states.

For completeness, we spell out the cumulants in terms of the signal moments up to 4<sup>th</sup> order from Eq. (B.2) [74]

$$\langle\langle\hat{a}\rangle\rangle = \langle\hat{a}\rangle \quad (\text{B.3})$$

$$\langle\langle\hat{a}^2\rangle\rangle = \langle\hat{a}^2\rangle - \langle\hat{a}\rangle^2 \quad (\text{B.4})$$

$$\langle\langle\hat{a}^\dagger \hat{a}\rangle\rangle = \langle\hat{a}^\dagger \hat{a}\rangle - \langle\hat{a}^\dagger\rangle \langle\hat{a}\rangle \quad (\text{B.5})$$

$$\langle\langle\hat{a}^3\rangle\rangle = \langle\hat{a}^3\rangle - 3\langle\hat{a}^2\rangle \langle\hat{a}\rangle + 2\langle\hat{a}\rangle^3 \quad (\text{B.6})$$

$$\langle\langle\hat{a}^\dagger \hat{a}^2\rangle\rangle = \langle\hat{a}^\dagger \hat{a}^2\rangle - \langle\hat{a}^\dagger\rangle \langle\hat{a}^2\rangle - 2\langle\hat{a}^\dagger \hat{a}\rangle \langle\hat{a}\rangle + 2\langle\hat{a}^\dagger\rangle \langle\hat{a}\rangle^2 \quad (\text{B.7})$$

$$\langle\langle\hat{a}^4\rangle\rangle = \langle\hat{a}^4\rangle - 4\langle\hat{a}^3\rangle \langle\hat{a}\rangle - 3\langle\hat{a}^2\rangle^2 + 12\langle\hat{a}^2\rangle \langle\hat{a}\rangle^2 - 6\langle\hat{a}\rangle^4 \quad (\text{B.8})$$

$$\begin{aligned} \langle\langle \hat{a}^\dagger \hat{a}^3 \rangle\rangle &= \langle \hat{a}^\dagger \hat{a}^3 \rangle - \langle \hat{a}^\dagger \rangle \langle \hat{a}^3 \rangle - 3 \langle \hat{a}^\dagger \hat{a}^2 \rangle \langle \hat{a} \rangle - 3 \langle \hat{a}^\dagger \hat{a} \rangle \langle \hat{a}^2 \rangle + 6 \langle \hat{a}^\dagger \rangle \langle \hat{a}^2 \rangle \langle \hat{a} \rangle \\ &\quad + 6 \langle \hat{a}^\dagger \hat{a} \rangle \langle \hat{a} \rangle^2 - 6 \langle \hat{a}^\dagger \rangle \langle \hat{a} \rangle^3 \end{aligned} \quad (\text{B.9})$$

$$\begin{aligned} \langle\langle (\hat{a}^\dagger)^2 \hat{a}^2 \rangle\rangle &= \langle (\hat{a}^\dagger)^2 \hat{a}^2 \rangle - 2 \langle (\hat{a}^\dagger)^2 \hat{a} \rangle \langle \hat{a} \rangle - \langle (\hat{a}^\dagger)^2 \rangle \langle \hat{a}^2 \rangle + 2 \langle (\hat{a}^\dagger)^2 \rangle \langle \hat{a} \rangle^2 - 2 \langle \hat{a}^\dagger \hat{a}^2 \rangle \langle \hat{a}^\dagger \rangle \\ &\quad - 2 \langle \hat{a}^\dagger \hat{a} \rangle^2 + 8 \langle \hat{a}^\dagger \hat{a} \rangle \langle \hat{a}^\dagger \rangle \langle \hat{a} \rangle + 2 \langle \hat{a}^\dagger \rangle^2 \langle \hat{a}^2 \rangle - 6 \langle \hat{a}^\dagger \rangle^2 \langle \hat{a} \rangle^2 \end{aligned} \quad (\text{B.10})$$

Other cumulants of 4<sup>th</sup> order are calculated with  $\langle\langle (\hat{a}^\dagger)^m \hat{a}^n \rangle\rangle = \langle\langle (\hat{a}^\dagger)^n \hat{a}^m \rangle\rangle^*$ .

# Appendix C

## Negativity

The discussions in this section are based on the supplementary material from Ref. [19]. For a bipartite system, the amount of entanglement between the subsystems A and B can be quantified by means of the negativity

$$\mathcal{N}(\rho) \equiv \frac{\|\rho^{TB}\|_1 - 1}{2}, \quad (\text{C.1})$$

where  $\rho$  is the density matrix of the total system, and  $\|\rho^{TB}\|_1 = \text{Tr}|\rho^{TB}|$  is the trace norm of the partial transpose of  $\rho$  with respect to subsystem B,  $\rho^{TB}$ . If  $\mathcal{N}(\rho) > 0$ , the state is entangled. For a maximally entangled state,  $\mathcal{N}(\rho) \rightarrow \infty$ .

In the case of Gaussian states, all measures of entanglement are equivalent, and they are defined by the covariance matrix

$$\boldsymbol{\sigma} = \begin{pmatrix} \boldsymbol{\alpha} & \boldsymbol{\gamma} \\ \boldsymbol{\gamma}^T & \boldsymbol{\beta} \end{pmatrix}. \quad (\text{C.2})$$

Annihilation and creation operators,  $s_{1,2}$  and  $s_{1,2}^\dagger$ , are used to represent the two subsystems. We define the matrices

$$\boldsymbol{\alpha} \equiv \begin{pmatrix} \alpha_1 & \alpha_3 \\ \alpha_3 & \alpha_2 \end{pmatrix}, \boldsymbol{\beta} \equiv \begin{pmatrix} \beta_1 & \beta_3 \\ \beta_3 & \beta_2 \end{pmatrix}, \boldsymbol{\gamma} \equiv \begin{pmatrix} \gamma_{11} & \gamma_{12} \\ \gamma_{21} & \gamma_{22} \end{pmatrix} \quad (\text{C.3})$$

with

$$\alpha_1 = \langle \hat{s}_1^2 \rangle + \langle (\hat{s}_1^\dagger)^2 \rangle + 2\langle \hat{s}_1^\dagger \hat{s}_1 \rangle - \langle \hat{s}_1 + \hat{s}_1^\dagger \rangle^2 + 1 \quad (\text{C.4})$$

$$\alpha_2 = -\langle \hat{s}_1^2 \rangle - \langle (\hat{s}_1^\dagger)^2 \rangle + 2\langle \hat{s}_1^\dagger \hat{s}_1 \rangle + \langle \hat{s}_1 - \hat{s}_1^\dagger \rangle^2 + 1 \quad (\text{C.5})$$

$$\alpha_3 = i \left( -\langle \hat{s}_1^2 \rangle + \langle (\hat{s}_1^\dagger)^2 \rangle + \langle \hat{s}_1 \rangle^2 - \langle \hat{s}_1^\dagger \rangle^2 \right) \quad (\text{C.6})$$

$$\beta_1 = \langle \hat{s}_2^2 \rangle + \langle (\hat{s}_2^\dagger)^2 \rangle + 2\langle \hat{s}_2^\dagger \hat{s}_2 \rangle - \langle \hat{s}_2 + \hat{s}_2^\dagger \rangle^2 + 1 \quad (\text{C.7})$$

$$\beta_2 = -\langle \hat{s}_2^2 \rangle - \langle (\hat{s}_2^\dagger)^2 \rangle + 2\langle \hat{s}_2^\dagger \hat{s}_2 \rangle + \langle \hat{s}_2 - \hat{s}_2^\dagger \rangle^2 + 1 \quad (\text{C.8})$$

$$\beta_3 = i\left(-\langle \hat{s}_2^2 \rangle + \langle (\hat{s}_2^\dagger)^2 \rangle + \langle \hat{s}_2 \rangle^2 - \langle \hat{s}_2^\dagger \rangle^2\right) \quad (\text{C.9})$$

$$\begin{aligned} \gamma_{11} = & \langle \hat{s}_1 \hat{s}_2 + \hat{s}_1 \hat{s}_2^\dagger + \hat{s}_1^\dagger \hat{s}_2 + \hat{s}_1^\dagger \hat{s}_2^\dagger \rangle / 2 \\ & + \langle \hat{s}_2 \hat{s}_1 + \hat{s}_2 \hat{s}_1^\dagger + \hat{s}_2^\dagger \hat{s}_1 + \hat{s}_2^\dagger \hat{s}_1^\dagger \rangle / 2 \\ & - \langle \hat{s}_1 + \hat{s}_1^\dagger \rangle \langle \hat{s}_2 + \hat{s}_2^\dagger \rangle \end{aligned} \quad (\text{C.10})$$

$$\begin{aligned} \gamma_{12} = & \langle \hat{s}_1 \hat{s}_2 - \hat{s}_1 \hat{s}_2^\dagger + \hat{s}_1^\dagger \hat{s}_2 - \hat{s}_1^\dagger \hat{s}_2^\dagger \rangle / 2i \\ & + \langle \hat{s}_2 \hat{s}_1 + \hat{s}_2 \hat{s}_1^\dagger - \hat{s}_2^\dagger \hat{s}_1 - \hat{s}_2^\dagger \hat{s}_1^\dagger \rangle / 2i \\ & + i \langle \hat{s}_1 + \hat{s}_1^\dagger \rangle \langle \hat{s}_2 - \hat{s}_2^\dagger \rangle \end{aligned} \quad (\text{C.11})$$

$$\begin{aligned} \gamma_{21} = & \langle \hat{s}_1 \hat{s}_2 + \hat{s}_1 \hat{s}_2^\dagger - \hat{s}_1^\dagger \hat{s}_2 - \hat{s}_1^\dagger \hat{s}_2^\dagger \rangle / 2i \\ & + \langle \hat{s}_2 \hat{s}_1 - \hat{s}_2 \hat{s}_1^\dagger + \hat{s}_2^\dagger \hat{s}_1 - \hat{s}_2^\dagger \hat{s}_1^\dagger \rangle / 2i \\ & + i \langle \hat{s}_1 - \hat{s}_1^\dagger \rangle \langle \hat{s}_2 + \hat{s}_2^\dagger \rangle \end{aligned} \quad (\text{C.12})$$

$$\begin{aligned} \gamma_{22} = & \langle -\hat{s}_1 \hat{s}_2 + \hat{s}_1 \hat{s}_2^\dagger + \hat{s}_1^\dagger \hat{s}_2 - \hat{s}_1^\dagger \hat{s}_2^\dagger \rangle / 2 \\ & + \langle -\hat{s}_2 \hat{s}_1 + \hat{s}_2 \hat{s}_1^\dagger + \hat{s}_2^\dagger \hat{s}_1 - \hat{s}_2^\dagger \hat{s}_1^\dagger \rangle / 2 \\ & + \langle \hat{s}_1 - \hat{s}_1^\dagger \rangle \langle \hat{s}_2 - \hat{s}_2^\dagger \rangle \end{aligned} \quad (\text{C.13})$$

and  $\gamma^T$  being the transpose of  $\gamma$ . Finally, the negativity becomes [75]

$$\mathcal{N} = \max \left\{ 0, \frac{1 - \nu}{2\nu} \right\} \equiv \max \{ 0, \tilde{\mathcal{N}} \}, \quad (\text{C.14})$$

where  $\nu \equiv \sqrt{(\Delta(\boldsymbol{\sigma}) - \sqrt{\Delta^2(\boldsymbol{\sigma}) - 4 \det \boldsymbol{\sigma}}) / 2}$  and  $\Delta(\boldsymbol{\sigma}) \equiv \det \boldsymbol{\alpha} + \det \boldsymbol{\beta} - 2 \det \boldsymbol{\gamma}$ .

Note that, despite not being a measure, the negativity kernel  $\tilde{\mathcal{N}}$  is a witness for arbitrary bipartite entanglement. In fact, if a non-Gaussian state has the same first and second moments as an entangled Gaussian state, it is entangled [76]. Consequently,  $\tilde{\mathcal{N}} > 0$  implies entanglement for any bipartite state.

# Bibliography

- [1] D. Deutsch & R. Jozsa. Rapid solution of problems by quantum computation. *Proc. R. Soc. Lond. A* **439**, 553–558 (1992).
- [2] P. W. Shor. Algorithms for quantum computation: discrete logarithms and factoring. *Proc. 37th Ann. Symp. on the Foundations of Comp. Sci. (FOCS)* 124–134 (1994).
- [3] N. J. Cerf, M. Lévy & G. Van Assche. Quantum distribution of Gaussian keys using squeezed states. *Phys. Rev. A* **63**, 052311 (2001).
- [4] F. Grosshans, G. Van Assche, J. Wenger, R. Brouri, N. J. Cerf & P. Grangier. Quantum key distribution using gaussian-modulated coherent states. *Nature* **421**, 238–241 (2003).
- [5] A. Furusawa, J. L. Sørensen, S. L. Braunstein, C. A. Fuchs, H. J. Kimble & E. S. Polzik. Unconditional quantum teleportation. *Science* **282**, 706–709 (1998).
- [6] T. C. Zhang, K. W. Goh, C. W. Chou, P. Lodahl & H. J. Kimble. Quantum teleportation of light beams. *Phys. Rev. A* **67**, 033802 (2003).
- [7] W. P. Bowen, N. Treps, B. C. Buchler, R. Schnabel, T. C. Ralph, H.-A. Bachor, T. Symul & P. K. Lam. Experimental investigation of continuous-variable quantum teleportation. *Phys. Rev. A* **67**, 032302 (2003).
- [8] D. L. Moehring, P. Maunz, S. Olmschenk, K. C. Younge, D. N. Matsukevich, L.-M. Duan & C. Monroe. Entanglement of single-atom quantum bits at a distance. *Nature* **449**, 68–71 (2007).
- [9] H. Bernien, B. Hensen, W. Pfaff, G. Koolstra, M. S. Blok, L. Robledo, T. H. Taminiau, M. Markham, D. J. Twitchen, L. Childress & R. Hanson. Heralded entanglement between solid-state qubits separated by three metres. *Nature* **497**, 86–90 (2013).
- [10] H. J. Kimble. The quantum internet. *Nature* **453**, 1023–1030 (2008).
- [11] J. M. Raimond, M. Brune & S. Haroche. Manipulating quantum entanglement with atoms and photons in a cavity. *Rev. Mod. Phys.* **73**, 565–582 (2001).
- [12] H. Walther, B. T. H. Varcoe, B.-G. Englert & T. Becker. Cavity quantum electrodynamics. *Rep. Prog. Phys.* **69**, 1325–1381 (2006).

- 
- [13] A. Wallraff, D. I. Schuster, A. Blais, L. Frunzio, R.-S. Huang, J. Majer, S. Kumar, S. M. Girvin & R. J. Schoelkopf. Strong coupling of a single photon to a superconducting qubit using circuit quantum electrodynamics. *Nature* **431**, 162–167 (2004).
- [14] R. J. Schoelkopf & S. M. Girvin. Wiring up quantum systems. *Nature* **451**, 664–669 (2008).
- [15] T. Niemczyk, F. Deppe, H. Huebl, E. P. Menzel, F. Hocke, M. J. Schwarz, J. J. Garcia-Ripoll, D. Zueco, T. Hümmer, E. Solano, A. Marx & R. Gross. Circuit quantum electrodynamics in the ultrastrong-coupling regime. *Nature Phys.* **6**, 772–776 (2010).
- [16] C. M. Caves. Quantum limits on noise in linear amplifiers. *Phys. Rev. D* **26**, 1817–1839 (1982).
- [17] E. P. Menzel, F. Deppe, M. Mariani, M. Á. Araque Caballero, A. Baust, T. Niemczyk, E. Hoffmann, A. Marx, E. Solano & R. Gross. Dual-path state reconstruction scheme for propagating quantum microwaves and detector noise tomography. *Phys. Rev. Lett.* **105**, 100401 (2010).
- [18] R. Di Candia, E. P. Menzel, L. Zhong, F. Deppe, A. Marx, R. Gross & E. Solano. Dual-path methods for propagating quantum microwaves. *New J. Phys.* **16**, 015001 (2014).
- [19] E. P. Menzel, R. Di Candia, F. Deppe, P. Eder, L. Zhong, M. Ihmig, M. Haeberlein, A. Baust, E. Hoffmann, D. Ballester, K. Inomata, T. Yamamoto, Y. Nakamura, E. Solano, A. Marx & R. Gross. Path entanglement of continuous-variable quantum microwaves. *Phys. Rev. Lett.* **109**, 250502 (2012).
- [20] T. Yamamoto, K. Inomata, M. Watanabe, K. Matsuba, T. Miyazaki, W. D. Oliver, Y. Nakamura & J. S. Tsai. Flux-driven Josephson parametric amplifier. *Appl. Phys. Lett.* **93**, 042510 (2008).
- [21] I. Siddiqi, R. Vijay, F. Pierre, C. M. Wilson, M. Metcalfe, C. Rigetti, L. Frunzio & M. H. Devoret. RF-Driven Josephson bifurcation amplifier for quantum measurement. *Phys. Rev. Lett.* **93**, 207002 (2004).
- [22] M. A. Castellanos-Beltran, K. D. Irwin, G. C. Hilton, L. R. Vale & K. W. Lehnert. Amplification and squeezing of quantum noise with a tunable Josephson metamaterial. *Nature Phys.* **4**, 929–931 (2008).
- [23] B. Yurke, L. R. Corruccini, P. G. Kaminisky, L. W. Rupp, A. D. Smith, A. H. Silver, R. W. Simon & E. A. Whittaker. Observation of parametric amplification and deamplification in a Josephson parametric amplifier. *Phys. Rev. A* **39**, 2519–2533 (1989).

- [24] L. Zhong, E. P. Menzel, R. Di Candia, P. Eder, M. Ihmig, A. Baust, M. Haeberlein, E. Hoffmann, K. Inomata, T. Yamamoto, Y. Nakamura, E. Solano, F. Deppe, A. Marx & R. Gross. Squeezing with a flux-driven Josephson parametric amplifier. *New J. Phys.* **15**, 125013 (2013).
- [25] R. Movshovich, B. Yurke, P. G. Kaminsky, A. D. Smith, A. H. Silver, R. W. Simon & M. V. Schneider. Observation of zero-point noise squeezing via a Josephson-parametric amplifier. *Phys. Rev. Lett.* **65**, 1419–1422 (1990).
- [26] C. Eichler, D. Bozyigit, C. Lang, M. Baur, L. Steffen, J. M. Fink, S. Filipp & A. Wallraff. Observation of two-mode squeezing in the microwave frequency domain. *Phys. Rev. Lett.* **107**, 113601 (2011).
- [27] R. Di Candia, K. G. Fedorov, L. Zhong, S. Felicetti, E. P. Menzel, M. Sanz, F. Deppe, A. Marx, R. Gross & E. Solano. Quantum teleportation of propagating quantum microwaves. *arXiv preprint arXiv:1506.06701* (2015). URL <http://arxiv.org/abs/1506.06701>.
- [28] C. M. Wilson, G. Johansson, A. Pourkabirian, M. Simoen, J. R. Johansson, T. Duty, F. Nori & P. Delsing. Observation of the dynamical Casimir effect in a superconducting circuit. *Nature* **479**, 376–379 (2011).
- [29] M. G. A. Paris. Displacement operator by beam splitter. *Phys. Lett. A* **217**, 78–80 (1996).
- [30] D. F. Walls & G. J. Milburn. *Quantum Optics* (Springer, Berlin, 2008).
- [31] U. Leonhardt & H. Paul. Measuring the quantum state of light. *Prog. Quant. Electron.* **19**, 89–130 (1995).
- [32] E. Wigner. On the quantum correction for thermodynamic equilibrium. *Phys. Rev.* **40**, 749–759 (1932).
- [33] M. Hillery, R. F. O’Connell, M. O. Scully & E. P. Wigner. Distribution functions in physics: fundamentals. *Phys. Rep.* **106**, 121–167 (1984).
- [34] H. Weyl. *The theory of groups and quantum mechanics* (Courier Corporation, 1950).
- [35] S. N. Filippov & V. I. Man’ko. Evolution of microwave quantum states in terms of measurable ordered moments of creation and annihilation operators. *Opt. Spectrosc.* **112**, 365–372 (2012).
- [36] S. N. Filippov & V. I. Man’ko. Measuring microwave quantum states: Tomogram and moments. *Phys. Rev. A* **84**, 033827 (2011).

- [37] A. Wünsche. Reconstruction of operators from their normally ordered moments for a single boson mode. *Quantum Opt.* **2**, 453–466 (1990).
- [38] C. T. Lee. Moment problem for a density matrix and a biorthogonal set of operator bases. *Phys. Rev. A* **46**, 6097–6099 (1992).
- [39] U. Herzog. Generating-function approach to the moment problem for the density matrix of a single mode. *Phys. Rev. A* **53**, 2889–2892 (1996).
- [40] V. Bužek, G. Adam & G. Drobný. Quantum state reconstruction and detection of quantum coherences on different observation levels. *Phys. Rev. A* **54**, 804–820 (1996).
- [41] V. Dodonov, E. Kurmyshev & V. Man’ko. Generalized uncertainty relation and correlated coherent states. *Phys. Lett. A* **79**, 150–152 (1980).
- [42] E. T. Jaynes. Information Theory and Statistical Mechanics. *Phys. Rev.* **106**, 620–630 (1957).
- [43] V. Bužek, G. Adam & G. Drobný. Reconstruction of Wigner functions on different observation levels. *Ann. Phys.* **245**, 37–97 (1996).
- [44] M. O. Scully & M. S. Zubairy. *Quantum optics* (Cambridge University Press, Cambridge, 1997).
- [45] E. Schrödinger. Der stetige Übergang von der Mikro- zur Makromechanik. *Naturwissenschaften* **14**, 664–666 (1926).
- [46] F. Mallet, M. A. Castellanos-Beltran, H. S. Ku, S. Glancy, E. Knill, K. D. Irwin, G. C. Hilton, L. R. Vale & K. W. Lehnert. Quantum state tomography of an itinerant squeezed microwave field. *Phys. Rev. Lett.* **106**, 220502 (2011).
- [47] C. Eichler, D. Bozyigit, C. Lang, L. Steffen, J. Fink & A. Wallraff. Experimental State Tomography of Itinerant Single Microwave Photons. *Phys. Rev. Lett.* **106**, 220503 (2011).
- [48] C. Eichler, Y. Salathe, J. Mlynek, S. Schmidt & A. Wallraff. Quantum-Limited amplification and entanglement in coupled nonlinear resonators. *Phys. Rev. Lett.* **113**, 110502 (2014).
- [49] E. P. Menzel. *Propagating quantum microwaves: dual-path state reconstruction and path entanglement*. Phd thesis, Technische Universität München (2013). URL [http://www.wmi.badw.de/publications/theses/Menzel\\_Doktorarbeit\\_2013.pdf](http://www.wmi.badw.de/publications/theses/Menzel_Doktorarbeit_2013.pdf).
- [50] B. Josephson. Possible new effects in superconductive tunnelling. *Physics Letters* **1**, 251–253 (1962).

- [51] R. Gross & A. Marx. *Festkörperphysik* (Oldenbourg Verlag, München, 2012).
- [52] J. Clarke & A. I. Braginski. *The SQUID Handbook* (Wiley-VCH Verlag, Weinheim, 2004).
- [53] G. Wendin & V. Shumeiko. Superconducting Quantum Circuits, Qubits and Computing. *arXiv preprint arXiv:cond-mat/0508729* (2005). URL <http://arxiv.org/abs/cond-mat/0508729>.
- [54] M. Sandberg, C. M. Wilson, F. Persson, T. Bauch, G. Johansson, V. Shumeiko, T. Duty & P. Delsing. Tuning the field in a microwave resonator faster than the photon lifetime. *Appl. Phys. Lett.* **92**, 203501 (2008).
- [55] D. M. Pozar. *Microwave Engineering* (John Wiley & Sons, Inc., New York, 2005).
- [56] T. Yamamoto, Y. Nakamura & K. Koshino. Quantum analysis on flux-driven parametric amplifier (2009), personal communication .
- [57] J. M. Sage, V. Bolkhovskiy, W. D. Oliver, B. Turek & P. B. Welander. Study of loss in superconducting coplanar waveguide resonators. *J. Appl. Phys.* **109**, 063915 (2011).
- [58] W. Buckel & R. Kleiner. *Superconductivity: Fundamentals and Applications* (Wiley-VCH Verlag, Weinheim, 2004).
- [59] P. Kittara, G. Yassin & S. Withington. Analysis of superconducting coplanar waveguides for SIS mixer circuits (2002).
- [60] M. Wallquist, V. S. Shumeiko & G. Wendin. Selective coupling of superconducting charge qubits mediated by a tunable stripline cavity. *Phys. Rev. B* **74**, 224506 (2006).
- [61] A. Baust. *Characterization of flux-driven Josephson parametric amplifiers*. Diploma thesis, Technische Universität München (2010). URL [http://www.wmi.badw-muenchen.de/publications/theses/Baust,Alexander\\_Diplomarbeit\\_2012.pdf](http://www.wmi.badw-muenchen.de/publications/theses/Baust,Alexander_Diplomarbeit_2012.pdf).
- [62] A. Marx, J. Hoess & K. Uhlig. Dry dilution refrigerator for experiments on quantum effects in the microwave regime. *arXiv preprint arXiv:1412.3619* (2014). URL <http://arxiv.org/abs/1412.3619>.
- [63] K. Uhlig. Dry dilution refrigerator with He-4 precool loop. *arXiv preprint arXiv:1412.3665* (2014). URL <http://arxiv.org/abs/1412.3665>.
- [64] G. J. Dolan. Offset masks for lift-off photoprocessing. *Appl. Phys. Lett.* **31**, 337–339 (1977).

- [65] E. Hoffmann, F. Deppe, T. Niemczyk, T. Wirth, E. P. Menzel, G. Wild, H. Huebl, M. Mariantoni, T. Weißl, A. Lukashenko, A. P. Zhuravel, A. V. Ustinov, A. Marx & R. Gross. A superconducting  $180^\circ$  hybrid ring coupler for circuit quantum electrodynamics. *Appl. Phys. Lett.* **97**, 222508 (2010).
- [66] M. Mariantoni, E. P., F. Deppe, M. Á. Araque Caballero, A. Baust, T. Niemczyk, E. Hoffmann, E. Solano, A. Marx & R. Gross. Planck Spectroscopy and Quantum Noise of Microwave Beam Splitters. *Phys. Rev. Lett.* **105**, 133601 (2010).
- [67] A. Barone & G. Paternò. *Physics and Application of the Josephson Effect* (John Wiley & Sons, Inc., New York, 1982).
- [68] B. S. Landman. Calculation of threshold curves for Josephson quantum interference devices. *IEEE Trans. Magn.* **13**, 871–874 (1977).
- [69] W.-T. Tsang & T. V. Duzer. dc analysis of parallel arrays of two and three Josephson junctions. *J. Appl. Phys.* **46**, 4573–4580 (1975).
- [70] R. de Bruyn Ouboter & A. de Waele. *Superconducting Point Contacts Weakly Connecting Two Superconductors*, Vol. VI (Elsevier Science PuElsevier, Amsterdam, 1970).
- [71] V. Lefevre-Seguin, E. Turlot, C. Urbina, D. Esteve & M. H. Devoret. Thermal activation of a hysteretic dc superconducting quantum interference device from its different zero-voltage states. *Phys. Rev. B* **46**, 5507–5522 (1992).
- [72] L. Zhong. *Generation and Reconstruction of Propagating Quantum Microwaves*. Phd thesis, Technische Universität München (2015).
- [73] R. Schack & A. Schenzle. Moment hierarchies and cumulants in quantum optics. *Phys. Rev. A* **41**, 3847–3852 (1990).
- [74] L.-Z. Jiang. The cumulants of bosonic quantum states. *Proc. SPIE* **7846**, 784612 (2010).
- [75] G. Adesso & F. Illuminati. Gaussian measures of entanglement versus negativities: Ordering of two-mode Gaussian states. *Phys. Rev. A* **72**, 032334 (2005).
- [76] P. Hyllus & J. Eisert. Optimal entanglement witnesses for continuous-variable systems. *New J. Phys.* **8**, 51 (2006).

# Acknowledgments

This work would not have been possible without the help and knowledge of many people, who i would like to thank in the following:

Prof. Dr. Rudolf Gross for giving me the opportunity to join the qubit group at the Walther Meißner Institute as a master student and get to know this interesting field of research. His vast knowledge and dedication as scientist inspire me.

Dr. Kirill Fedorov as advisor during my work at WMI. It was a pleasure working with him. I enjoyed plenty discussions about interesting physics as well as other not physics related topics. He always was available for questions and problems and was happy to help. The valuable suggestions and solutions to technical as well as theoretical problems, contributed strongly to progress in the project. His enthusiasm in the work is admirable. This work would not have been possible without him and I thank him for the great time.

Dr. Ling Zhong also as advisor working on the same project as Ph.D. student. I congratulate her for her successful Ph.D. graduation. I thank her for introducing me to the lab-work, the measurement setup and also the physics related to the work. We had plenty fruitful discussions about the project and she always gave useful ideas on current problems. I also thank her for various measurement programs in Labview, analysis codes in Matlab and measurements. I admire her endurance during long, repetitive measurements and during working also late at night. I wish you all the best!

Dr. Frank Deppe and Dr. Achim Marx for leading the qubit group and valuable ideas and suggestions concerning the analysis of measurement data of the project. The kindness and friendliness made my stay at WMI enjoyable. The great lecture of Frank woke my interest in the qubit group and made it possible to do my master thesis at WMI in the first place. Despite his busy schedule, he was always happy to answer any kind of questions. I am also specifically grateful to Achim for proof reading my thesis and his suggestions and corrections. Additionally, he gave valuable suggestions and explanations concerning the measured data and was always available for questions, answering them with his kind and calm nature.

Prof. Dr. Enrique Solano and all his group for the collaboration with WMI and various visits during my stay. Especially Roberto Di Candia has to be thanked for theory support on fundamental questions regarding the dual-path reconstruction. The talks of Enrique were inspiring and his huge dedication towards physics is captivating.

To my office colleagues Franz Kramer, Ahmed Alshemi, Daniel Schwienbacher, Philip Schmidt, Prof. Dr. B.S. Chandrasekhar, Christian Schneider, Michael Fischer, Fabian Kössel and Michael Rehm. The atmosphere in the office was always very nice and we had plenty interesting discussions about various topics. Also Martin Betzenbichler for working at the same project. He was always happy to help and answer questions. I'm also grateful for the help when working on the cryostat.

Our Japanese collaborators, Tsuyoshi Yamamoto, Kunihiro Inomata and Prof. Yasunobu Nakamura for providing us with the JPA samples of the work. Also the theory concerning the flux-driven JPA was very valuable to understand and describe the measured data.

The workshop team for always being friendly and helpful. They constructed various important pieces for the work and I am thankful for their effort. Also Emel Dönertas and Ludwig Ossiander deserve a special thanks for the administrative work.

All members of WMI and especially the qubit group for the great working atmosphere. Everybody was happy to help and available for questions. Also special thanks to Peter Eder, he gave very valuable ideas in explaining the results.

My parents for their constant support throughout my studies. Without their support my studies and the master's thesis would not have been possible. I am grateful for their understanding and their encouragement. Their doors are always open for me and I can always rely on them if I need help. Also my good friends, which were always a pleasant distraction from work.

Finally, I thank my girlfriend Alexandra for being there for me for the last years and support my studies, even though I spent a lot of time at WMI and the university. I'm very grateful for her constant support and being there for me through hard times. She built me up when the measurements where not going as planned or I had other problems. I'm glad to have her in my life!